THE EFFECT OF HYDRATE FORMATION ON THE ELASTIC PROPERTIES OF UNCONSOLIDATED SEDIMENT

by

Marisa B. Rydzy

A thesis submitted to the Faculty and the Board of Trustees of the Colorado School of Mines in partial fulfillment of the requirements for the degree of Doctor of Philosophy (Geophysics)

Golden, Colorado

Date _____

Signed: _____

Marisa B. Rydzy

Signed: _____

Dr. Michael L. Batzle

Thesis Advisor

Golden, Colorado

Date _____

Signed: _____

Dr. Terence K. Young

Professor and Head

Department of Geophysics

ABSTRACT

Natural gas hydrates exist in unconsolidated marine or permafrost sediments and can adopt many morphologies. Hydrates can occur in shapes of nodules, veins, layers, or finely disseminated between sediment grains. In the latter configuration, hydrate may cement sediment grains, act as a load-bearing sediment component, or occur free-floating in the pore fluid. While the sediment lithology dictates whether hydrate is present in massive or disseminated form, the manner of hydrate formation determines whether the disseminated hydrate will act as a cementing or non-cementing element in the system. The physical properties imparted to the hydrate-bearing sediment by hydrate can vary dramatically depending on how the hydrate forms, and in nature, gas hydrates generally form from gas dissolved in water, but can also form from water in the presence of a free gas phase. In this study, the effect of hydrate formation on the wave velocities of unconsolidated sediment was investigated in a series of laboratory studies, with particular focus on the extent to which the initial water saturation controls the manner in which hydrate is distributed, and thus the extent to which hydrate formation increases the wave velocity in sands.

Ultrasonic p- and s-wave velocities (v_p, v_s) were measured in conjunction with magnetic resonance imaging (MRI) in hydrate-bearing Ottawa Sand F110 during hydrate formation and dissociation. v_p and v_s were determined as functions of gas hydrate saturation (S_h). Hydrates were formed out of solution using tetrahydrofuran (THF) and through CH_4 injection into partially water-saturated samples. For the latter,

samples with low and high **i**nitial water saturation (S_{wi}) were tested. The recorded velocities exhibited a noticeable dependence on S_{wi}. At low S_{wi} (~20%) the hydrate stiffened the sediment and increased the ultrasonic velocities dramatically. However, the rate at which the velocity increased during hydrate formation decreased with increasing S_{wi} and small changes in the initial water saturation resulted in significant changes in final velocities. At high S_{wi} (~80%), the velocity increased almost linearly with increasing hydrate content even at very low S_h. This behavior differed from that observed for hydrate formed out of solution. Ultrasonic velocities recorded in water-saturated, THF hydrate-bearing sand sediment did not change until a critical hydrate saturation of 35-50 percent was exceeded.

Comparing measured velocities to those calculated with existing rock physics models links the initial water saturation, which determines the gas-water distribution in the sediment and hence the location of initial hydrate formation, to the evolution of wave velocity during hydrate formation. We concluded that at low S_{wi}, the water is evenly distributed and located at the grain contacts. The resulting hydrate cements the grains, dramatically increasing the wave velocities even at low hydrate saturations. At high S_{wi}, gas occurs in stiff bubbles within the pore space. The resulting hydrate particles become load-bearing and keep the grains from slipping. At intermediate S_{wi}, gas and water appear to occur as patches, resulting in a mixture of load-bearing and cementing hydrate. The model comparison also reinforces our picture of hydrate-formation out of solution, where the pore-filling hydrate particles do not interact with the sediment until a critical value for S_h is exceeded and the hydrate becomes load-bearing.

To test the dependence of the initial water distribution on the initial water saturation, micro X-ray CT images were also acquired of partially saturated glass-bead packs without hydrate but with varying amounts of water. At low water saturations, water occurred as bridges between adjacent glass beads or was located at the glass-bead contacts. At high water saturations, water occurred as a continuous phase and gas was present in the form of bubbles or patches. At intermediate water saturations both types of water distributions, gas bubbles and water bridges, were observed within one sample. With decreasing S_{wi}, the closer the gas/water interface is located to the grain contact, the higher the degree of cementation will be when hydrate forms . Conversely, the higher the S_{wi}, the less cementation occurs and the less a given degree of hydrate formation will affect v_p and v_s in unconsolidated sediments.

To extend our observations to hydrate-bearing systems, the distribution of THF and cyclopentane (CP) hydrate packs of glass beads was observed with micro X-ray computed tomography (CT). While THF is completely miscible in water, CP and water coexist as two separate phases. After hydrate formation in the THF hydrate-bearing samples, unconverted water was identified at the grain contacts and was often observed as a thin layer between hydrate and the glass-beads, indicating that the hydrate formation from the dissolved phase had initiated away from the glass beads and the bead-to-bead contacts. In some areas, THF hydrates grew to become amorphous patches that surrounded grains, but in most cases the hydrate was restricted to individual pores and exhibited characteristically sharp edges. In the CP hydrate-bearing samples, the image contrast between water/ice and CP hydrate could not be resolved. However, it appeared as if CP hydrate had formed along the CP-water interface and

served as a diffusion barrier between the two phases. As hydrate in known to initially grow at the gas-water interface, the hydrate distribution was most likely affected by the distribution of water prior to hydrate formation.

Based on the experimental results and our comparison with rock-physics theory, a conceptual model of hydrate in sediment was developed. The distribution of hydrate can be shown to be primarily a function of the water distribution within the sample prior to hydrate formation. With increasing water content, the distribution of the liquid phase transitions from being located at the grain contacts, to forming patchy networks, and finally becoming the continuous phase. When gas occurs as the continuous phase, hydrate grows into the water phase and the resulting hydrate will cement sediment grains. If water is the continuous phase, hydrate will grow into the gas phase and the resulting hydrate will initially be pore filling, but will become patchy and load-bearing as the hydrate saturation grows beyond 35-50% of the pore space.

TABLE OF CONTENTS

LIST OF FIGURES

LIST OF TABLES

LIST OF SYMBOLS

Chapter 2

C_3H_8 propane

CH_4 methane

CO_2 carbon-dioxide

D sample diameter

DL change in length due to applied confining pressure

Dt deadtime (Dt_p, Dt_s) required for an acoustic signal to pass through the electronics and end caps in the absence of a specimen.

H_2O water

L sample length

Li (i=1,2,3…) length measured at different sample angles

m_s sand mass

m_w water mass

MXCT micro X-ray computed tomography

P_d effective pressure

S_{wi} Initial water saturation

t arrival time of ultrasonic pulse (t_p, t_s)

THF tetrahydrofuran (C_4H_8O)

v velocity of p- or s-wave (v_p, v_s)

V_s sand volume

V_w water volume

V_{tot} total sample volume

V_{pore} pore volume

ΔDL error of length change

ΔDt deadtime error (ΔDt_p, ΔDt_s)

ΔL overall error of sample length

ΔL* precision of length-measurement tool

ΔL’ standard deviation of L_i

Δt uncertainty of picked arrival time

Δv absolute error for velocity (Δv_p, Δv_s)

Δv/v relative error for velocity ($\Delta v_p/v_p$, $\Delta v_s/v_s$)

ρ_i density of ice

ρ_s density of sand grains

ρ_w density of water

ϕ Porosity

Chapter 3

3D three-dimensional

CH_4 methane

F1 CH_4 hydrate formation method 1 (pressurization before cooling)

F2 CH_4 hydrate formation method 2 (cooling before pressurization)

G Shear modulus [GPa]

H_2O water

K	bulk modulus [GPa]
L	sample length [m]
MRI	magnetic resonance imaging
P_c	confining pressure [psi (MPa)]
P_d	differential (a.k.a. effective) pressure [psi (MPa)]: $P_d=P_c-P_p$
Pp	pore pressure [psi (MPa)]
S_h	hydrate saturation
$S_{w,res}$	residual water fraction after hydrate formation
S_{wi}	Initial water saturation
T	temperature [°C]
t	traveltime of elastic wave through sample [s]
THF	tetrahydrofuran
v	velocity
v_p	P-wave velocity [m/s]
v_s	S-wave velocity [m/s]
ΔL	precision of length measurement [m]
Δt	precision of traveltime measurement [s] = waveform sampling rate
ΔV	uncertainty of velocity [m/s]
v	Poisson ratio
ρ	density [kg/m^3]

Chapter 4

B_h	Bulk modulus of CH_4 hydrate (= K_h)

B_m Bulk modulus of sediment matrix (= K_m)

B_w Bulk modulus of water (= K_w)

C Contact number

G Shear modulus

HM Hertz-Mindlin Model

K Bulk modulus

K_d Bulk modulus of sediment framework in TPBT (= K_{hm} or = K_{sm})

K_{hKT} Kuster-Toksöz bulk modulus for hydrate in TPBT

K_{hm} Bulk modulus of sediment framework in Three-Phase Biot Theory

K_{HS} Hashin-Shtrikman upper bound bulk modulus

K_{mKT} Kuster-Toksöz bulk moduli for sediment in TPBT

K_s Bulk modulus of sediment or hydrate grains in TPBT (Lee & Waite 2008)

K_{sm} Bulk modulus of sediment framework in Three-Phase Biot Theory

n Cementation exponent

P_e effective pressure

P_e* Empirical pressure parameter in TPBT

R_{ij} Stiffness matrix

S_h Gas (CH_4) hydrate saturation

S_{hc} Critical hydrate saturation

S_{wi} Initial water saturation

V_0 p- or s-wave velocity before hydrate formation

v_h P-wave velocity of gas hydrate

v_m P-wave velocity of sediment matrix

v_p p-wave (compressional) velocity

v_s s-wave (shear) velocity

v_{sk} Small-strain Poisson ratio for the sediment matrix

v_w P-wave velocity of water

V_{wood} P-wave velocity calculated using Wood's equation

V_{wyllie} P-wave velocity calculated using Wyllie's time average equation

W Weighting factor

α Shear velocity at 1 kPa effective pressure in cemented-soil model

α Consolidation factor in TPBT

β Empirical parameter capturing pressure sensitivity of v_s (Cemented Soil Model)

β Empirical parameter in TPBT

ε Empirical parameter capturing the hydrate habit in TPBT

θ Empirical parameter capturing hydrate habit

μ_d Shear modulus of sediment framework in TPBT (= μ_{hm} or = μ_{sm})

μ_{hKT} Kuster-Toksöz shear modulus for hydrate in TPBT

μ_{hm} Shear modulus of sediment framework in Three-Phase Biot Theory

μ_{HS} Hashin-Shtrikman upper bound shear modulus

M_{ij} Shear matrix

μ_s Bulk modulus of sediment or hydrate grains in TPBT (Lee & Waite 2008)

μ_{sm} Shear modulus of sediment framework in Three-Phase Biot Theory

$\mu_{sm,0}$ Shear modulus

ρ Bulk density (= ρ_{mix} = ρ_b)

ρ_b Bulk density

ρ_h CH_4 hydrate density

ρ_m Matrix density

ρ_{mix} Bulk density (= ρ = ρ_b)

ρ_w Water density

$\sigma_{\parallel}$ Horizontal effective stress

$\sigma_{\perp}$ Vertical effective stress

Φ Porosity

Φ_{as} Apparent porosity of sediment framework in TPBT

Φ_c Critical porosity

ϕ_h Hydrate fraction

ϕ_s Sediment fraction

ϕ_w Water fraction

ACKNOWLEDGEMENTS

The completion of this thesis would not have been possible without the help and support of my advisor, committee members, co-workers, friends, and family. I would like to specifically acknowledge and thank the following people.

First and foremost, to Mike Batzle, for giving me the opportunity and freedom to pursue a study in the field of squeezing gas hydrates. His guidance, reinforcement and patience (!) allowed me to grow as a researcher and as a person.

To Bill Waite, for the mentorship he provided, his diligence in reviewing my thesis, and the many, many discussions about the wondrous nature of THF hydrate. Bill also organized the Inter-Laboratory Comparison Project which inspired the repeatability study presented in this thesis.

Large part of the experimental work was performed at the ConocoPhillips Technology Center in Bartlesville, OK. I would like to thank James Howard, Keith Hester and Jim Steven for giving me the opportunity to work with them and learn from their experience. Our collaboration was not only a very enjoyable experience but made this thesis possible.

To Judith Schicks, who introduced me to the world of gas hydrates, has provided great scientific and moral support over the years, and who, in a fun, collaborative effort, helped to design the MXCT sample holder.

To the other committee members: Carolyn Koh, Diana Sava, Andre Revil, Terry Young, and Mark Miller for their constant support and encouragement.

To Hydrate Busters Zach Aman and Sergey Skiba, for sharing their knowledge about cyclopentane hydrates and for their assistance with the differential scanning calorimetry measurements.

To Mandy Schindler for spending countless days and nights in the laboratory watching over gas hydrate-bearing specimen. I am very grateful for her technical assistance with the experiments.

To Mathias Pohl, for being not only a reliable “lab minion”, but a good friend and road-trip buddy. I would like to thank all my friends who supported me during my studies not only in Golden, but also in Houston, Berlin, and Bartlesville. An special warm thanks goes to “my girls” Sophie Hancock, Hallgerd Erdal, and Julia Krmaer.

Thanks to the CSM Geophysics Department, past and present Rock Abusers, as well as Michelle Szobody and Dawn Umpleby, for creating a friendly work environment.

I would also like to acknowledge the financial support from the US Department of Energy, Award Number DE-FE 0009963. In addition, this study was funded by the DHI/Fluids Consortium and in part by BP.

And finally, thanks to my family for their unwavering love and support.

To my grandparents, Ruth and Erwin Hilgenfeld

CHAPTER 1

MOTIVATION & PROBLEM STATEMENT

Gas hydrates, a.k.a. clathrate hydrates, are naturally occurring ice-like crystalline solids, which form from water and gas molecules (e.g. methane, ethane, propane, carbon dioxide) under conditions of elevated pressure and low temperatures [Sloan and Koh, 2008]. They are composed of hydrogen-bonded water molecules, which enclose individual gas molecules (guests) in three-dimensional cage-like structures. Gas hydrate are also called clathrates (clatratus is Latin for cage). Natural gas hydrates occur worldwide in sediments, where thermobaric and geological conditions are appropriate for gas hydrate formation and stability. The existence of gas hydrates in nature was first proposed in the early 1970s [Stoll et al. 1971, Makogen et al. 1972, Bily and Dick 1974, Trofimuk et al. 1977] and confirmed almost ten years later in the early 1980s [reviewed by Kvenvolden and McMenamin, 1980 and Kvenvolden et al. 1993]. Figure 1.1 shows the worldwide distribution of all natural gas hydrate deposits that have been identified to date. As can be seen, gas hydrates are found in a variety of settings, such as oceanic sediments of outer continental slopes, and polar sediments on continents and continental shelves, as well as in deep water sediments of inland lakes and seas. Estimates of the amount of natural gas stored in the form of gas hydrates are highly speculative and vary widely over three orders of magnitude, from 10^{15} to 10^{18} m^3 (at standard temperature and pressure [Sloan and Koh, 2008; Boswell and Collett, 2011]). Nevertheless, even the most conservative estimates predict substantial gas volumes

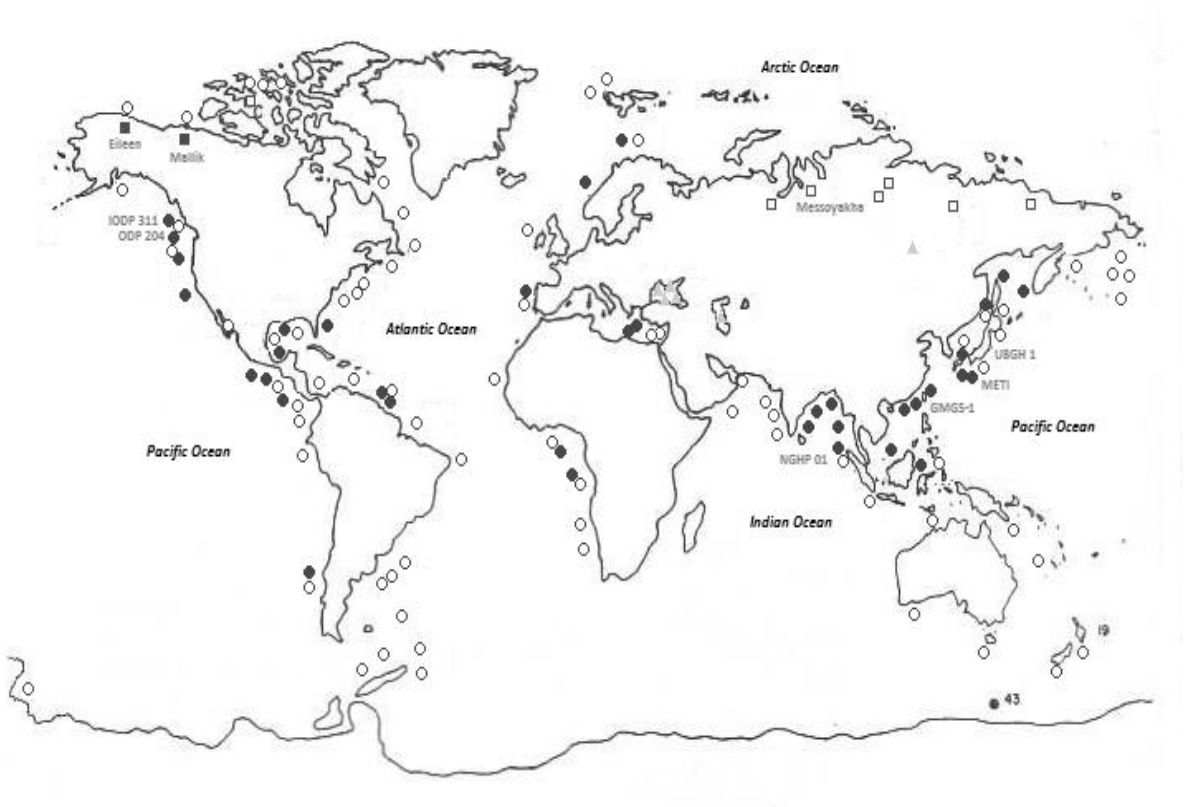

Figure 1.1: Worldwide distributions of gas hydrate deposits (after Collett et al. 2009) solid symbols mark locations where gas hydrate samples have been recovered, unfilled symbols represent inferred gas hydrate locations – circles, squares, and triangles represent occurrences in marine regions, permafrost areas, and inland lakes, respectively

within hydrate reservoirs that rival those present in conventional gas accumulations [Collett et al. 2009].

1.1 Relevance of Natural Gas Hydrates

Because of the enormous amount of naturally occurring gas hydrates, their wide geographical distribution, and high energy density, clathrate hydrates are considered as a potential alternative energy resource capable of contributing to satisfy the world's increasing demand of energy. In recent years, the realization that this unconventional resource could be developed with existing conventional oil and gas production technology sparked interest among major energy companies and turned gas hydrate development from a distant goal into a near-term possibility [Collett et al. 2009]. Currently, sand-dominated permafrost and marine deposits present the most promising targets for potential gas production and are closest to commercialization [Boswell et al., 2006; Collett et al, 2009]. Potential scenarios for gas production from a hydrate reservoir include depressurization, thermal stimulation, and inhibitor injection [Holder et al. 1984, Collett 2002, Satoh et al. 2005], as well as CO_2-CH_4-exchange [Graue et al., 2006; Stevens et al., 2008]. In addition to their role as a potential resource, natural gas hydrates pose a significant danger in conventional drilling and production operations [Ruppel et al., 2008]. Risks include uncontrolled gas release (gas kicks, blow outs), collapsed casings, gas leaks outside the borehole [Collett & Dallimore, 2002], as well as catastrophic well-site subsidence [e.g. Yakushev & Collett, 1992]. Drilling and the production of hot fluids through a hydrate-bearing interval introduce heat into the surrounding formation, which can cause gas hydrates present to decompose, release

gas, and possibly compromise the formation integrity. Naturally-destabilized gas hydrates may contribute to large-scale slope destabilization [e.g. Mosher 2009, Hornbach et al. 2007, Berndt et al. 2005, López et al. 2010] and build-up of atmospheric methane - a potent greenhouse gas [e.g. Dickens et al. 1995, Hesslebo et al., 2000, Pecher et al. 2005], though both of these hypotheses remain controversial [e.g. Bowen et al. 2006; Dickens, 2011; Ruppel, 2011].

1.2 Problem Statement

"The importance of gas hydrate either as an energy resource, as a driver for global climate change, or as a contributing factor in large submarine landslides, can only be fully assessed by accurately mapping the occurrence and concentration of hydrate within sediments" [Priest et al.,2009]. Where hydrate-bearing sediment cores are not available as direct evidence, the presence of gas hydrates can be detected indirectly by means of geophysical techniques such as reflection seismic surveys [e.g. Shelander et al, 2012] or sonic logging [e.g. Collett, 1998]. Seismic velocities of gas hydrates are higher compared to those of other pore fluids, and an increase in the overall velocity can generally be observed when hydrate is present in subsurface sediments [e.g. Yuan et al. 1996]. The relationship between seismic velocities and gas hydrate saturation (volumetric fraction of pore space occupied by gas hydrates), however, is not straightforward and strongly depends on the morphology of the gas hydrate occurrence [e.g. Sava and Hardage, 2006]. A handful of rock physics models have been developed that relate p- and s- velocities to the amount of gas hydrate present in the pore space [e.g. Lee et al., 1996; Ecker et al., 1998; Carcione and

Tinivella, 2000]. These models, however, strongly rely on empirical relationships that need to be calibrated [e.g. Lee at al., 1996] and/or require assumptions about the micro-structural arrangement of gas hydrate and sediment [e.g. Ecker et al. 1998]. Thus, there is a great need for extended laboratory studies of gas hydrate-bearing sediment to calibrate these rock physics models. As natural gas hydrate-cores are rare, costly, heterogeneous, and almost always show some degree of damage, sediments containing laboratory-formed gas hydrates must be used as an alternative. There are a number of different ways to form gas hydrate in sediment, and each laboratory generally has its preferred technique. Previous studies suggest the manner in which gas hydrate is formed impacts the hydrate habit and distribution [e.g. Priest et al., 2009; Lee et al., 2010]. To date, no comprehensive testing has been conducted within a single experimental apparatus that would allow a quantitative comparison between the different hydrate formation techniques, show the differences in the resulting hydrate distributions, as well as how those differences manifest themselves in the bulk elastic properties.

1.3 Thesis Scope

The objective of this PhD thesis was to investigate the effect hydrate formation techniques have on the pore-scale hydrate distribution and the subsequent effect on the elastic properties of unconsolidated sediment. The associated research involved a series of petrophysical tests on laboratory-formed hydrate-bearing sediments, including measurements of ultrasonic velocities. The hydrate formation methods in this study were: gaseous methane injection into partially water-saturated sand and the use of

liquid tetrahydrofuran as a hydrate former. These formation methods produce "cementing" and "non-cementing" hydrate, respectively. Imaging techniques such as magnetic resonance imaging and micro X-ray computed tomography were used to characterize the distribution of hydrate within the pore space and throughout the sample.

Previously, cementing and non-cementing hydrate were treated been treated as being completely distinct and unrelated with respect to their pore-scale distribution and elastic properties. The results of this thesis show that these two hydrate distributions represent end members of a continuous spectrum of hydrate morphologies that are linked by the initial water saturation present in the sediment prior to hydrate formation.

Our improved understanding of hydrate formation in unconsolidated sediment will provide guidance to those studying the physical properties of laboratory-formed gas hydrates, i.e. allow researchers to predict what hydrate distribution to expect as a function of initial water saturation and interpret their laboratory-derived data set and relate measured parameters. Hopefully, this knowledge can be extended to the formation of natural gas hydrate system and will help to better predict the elastic properties of gas hydrate-bearing sediments found in nature based on their formation history.

1.4 Thesis Organization

Chapter 2 addresses repeatability issues and uncertainties associated with laboratory synthesis of methane (CH_4) and tetrahydrofuran (THF) hydrates in sandpacks. It describes a series of ultrasonic velocity measurements performed under

varying differential pressure conditions on a standard set of sand samples, including dry, partially water-saturated, frozen, CH_4 and THF hydrate-bearing specimens.

Chapter 3 represents the first of four chapters concerned with the investigation of the effect of hydrate formation on the elastic properties of hydrate-bearing unconsolidated sediments. It reports the results of ultrasonic velocity measurements performed in conjunction with magnetic resonance imaging on hydrate-bearing sandpacks during hydrate formation and dissociation. The measurements focused on sediments containing gas hydrates formed either through CH_4 injection into partially water saturated sand with varying initial water saturations or by forming THF hydrate in initially fluid-saturated sediment.

Chapter 4 presents a comparison of the velocity data obtained from the experiments described in Chapter 3, and theoretical velocities calculated using state-of-the-art rock physics models. Some of the models were of an empirical nature, and their fitting parameters were varied to gain insight into the hydrate habit of the measured specimens. This allowed us to extend the models from predicting velocities of static three-phase systems to describing dynamic processes, i.e. hydrate formation or dissociation. Comparisons between measured and modeled velocity trends were used to relate experimental hydrate formation methods to the pore-scale hydrate distributions described by the models.

Chapter 5 details the results of micro X-ray computed tomography on THF and cyclopentane (CP) hydrate-bearing glass-bead specimens. It focuses on the investigation of the pore-scale hydrate distribution as a function of whether hydrate is formed out of solution (THF hydrate) or from separate gas and liquid phases (CP

hydrate). The resulting images helped to test conclusions drawn in Chapter 4, and to gain further insight into how the manner of hydrate formation affects the pore-scale hydrate distribution in unconsolidated sediment.

Chapter 6 brings together the key observations of each chapter and presents a conceptual model of hydrate formation in unconsolidated sediment. The model describes how the water saturation prior to hydrate formation determines the location of the hydrate in the pore space and consequently, the elastic properties of the hydrate-bearing sediment during and after hydrate formation.

Chapter 7 uses the key findings presented in Chapters 2-6 as a basis for recommending future work. The main focus of the proposed studies is to extend the current research to specimen and experimental conditions that are more representative of natural gas hydrate-bearing sediment systems.

CHAPTER 2

REPEATABILITY OF ULTRASONIC VELOCITY MEASUREMENTS OF DRY, PARTIALLY WATER-SATURATED, FROZEN, CH_4 HYDRATE, AND THF HYDRATE-BEARING OTTAWA SAND F110

Ultrasonic velocities were measured under varying effective pressure (3-15 MPa) in dry, partially water-saturated, frozen, THF- and CH_4-hydrate-bearing Ottawa Sand F110. The measurements were conducted on at least 3 specimens per sample type to assess the repeatability of velocity measurements in unconsolidated, non-cohesive sediments with multi-phase pore fillings. The best data agreement was found for dry, partially water-saturated, and THF hydrate-bearing sandpacks. P- and s-wave velocities for each data set were reproducible within ±200 m/s and ±150 m/s, respectively. Overall, our results were in good agreement with available literature values. The observed data scatter came from two error sources, namely specimen variability and measurement uncertainty. The specimen variability was attributed to variations in porosity and packing of the sandpacks. The specimen variability in sandpacks cemented by low concentrations of ice or gas hydrate was more pronounced, with the additional scatter in the data caused by variations in ice or hydrate content, inhomogeneous distribution of the solid phases, and differences in the amount of residual water. The main contributing factor to the measurement uncertainties for all specimens was associated with determining sample lengths. Large length uncertainties could be attributed to non-parallel transducer endplates and the low precision of length

measurements made using a ruler. Based on the measurement-related uncertainties, relative errors for the individual data points were determined through error propagation calculation. The resulting relative errors were 2-11%. In comparison, relative errors due to sample variability in dry partially water-saturated, frozen and THF hydrate-bearing samples were 11%, 15%, 13%, and 23% respectively. Relative errors based on sample variability for CH_4 hydrate-bearing samples exceeded 50%.

2.1 Introduction

Gases of low molecular weight (e.g. CH_4, C_3H_8, CO_2) and volatile liquids (e.g. THF, cyclopentane) form clathrate hydrates in the presence of water when subjected to sufficiently low temperatures and high pressures [Sloan and Koh, 2008]. Clathrate hydrates are crystalline inclusion compounds composed of “guest” molecules that are trapped in a rigid network of hydrogen-bonded water molecules. It was estimated that up to 10^{18} m^3 (STP) of natural gas could potentially be stored in form of gas hydrates worldwide in shallow permafrost and marine continental-slope sediments [Collett et al., 2009]. Mapping and quantifying the extent of natural gas hydrate deposits is vital for the assessment of natural gas hydrates not only in their role as an unconventional energy resource [Holder et al., 1984; Walsh et al., 2009], but as a potential hazard to conventional oil and gas production [Yakushev and Collett, 1992; Collett and Dallimore, 2002; Hadley et al., 2008; Ruppel et al., 2008] and submarine instabilities [Berndt et al. 2005; Mosher 2009].

Quantification of gas- or hydrate saturations based on seismic velocities poses a challenge as the relationship between velocities and the concentration of each phase is

not straightforward. For example, even small amounts of free gas reduce the compressional bulk modulus of sediment dramatically [Domenico, 1977]. In addition, the velocity in gas-bearing sediment is influenced by whether gas occurs in patches or as bubbles [Dvorkin and Nur, 1998]. Similarly, the velocity in gas hydrate-bearing sediments depends on the hydrate distribution [Helgerud et al. 1999; Sava and Hardage, 2006; Dai et al., 2012]. In fine-grained sediments, natural gas hydrates often displace grains and take on the shapes of nodules, veins or layers [Paull et al., 1996; Tréhu et al., 2006]. Gas hydrates that are most valuable for potential gas production and closest to commercialization commonly occur in sand-dominated reservoirs [Collett et al., 2009], however. Consequently, current energy-based research focuses on gas hydrates in coarse-grained sediments, where gas hydrates have been observed evenly disseminated between grains [Uchida et al., 2000] or as patchy occurrences [Tréhu et al. 2004]. At the pore-scale, the distribution of gas hydrates can be further classified as cementing, frame-supporting or free-floating in the pore center [Ecker et al., 1998; Helgerud et al., 1999].

Laboratory velocity measurements are important for quantifying the effect of gas hydrate and free gas on the elastic properties of sediment. However, obtaining accurate and repeatable measurements in multiphase unconsolidated sediment presents a challenge in itself [Waite et al., 2011]. In 2011, an inter-laboratory comparison project (ILCP) was conducted to gather and analyze results for a standard set of wave velocity tests [Waite et al., 2011; 2012]. Within the capabilities of each participating laboratory, p- and s-wave velocities (v_p and v_s) were measured in dry, partially and fully water-saturated, frozen and CH_4 hydrate-bearing Ottawa Sand F110. The velocity data

exhibited a significant spread, which was mainly attributed to differences in sample porosity, compaction, and the heterogeneous distribution of pore fluids, ice, and hydrate. The observed variability increased significantly for the frozen and hydrate-bearing specimens. This was attributed in part to inter-specimen variability, but differences in sample preparation and measurement techniques between the different laboratories added to the data variability.

In this study, we measured ultrasonic velocities of dry, partially water-saturated, frozen, CH_4 and tetrahydrofuran (THF) hydrate-bearing unconsolidated sandpacks under varying effective pressure (3-15 MPa). The measurements were performed in accordance with the guidelines dictated by the ILCP. Participants of the ILCP generally submitted data only for one sample per test. At least three specimens were tested in this study for each type of sample to assess the reproducibility of velocity measurements within one laboratory and eliminate measurement-based variability. No uncertainties were reported for individual ILCP data points as it was assumed that these uncertainties were small compared to the spread in data. We performed thorough error analysis to determine the uncertainty associated with each data point. The resulting data sets will be compared with results of the ILCP as well as with literature values published for dry, partially water-saturated, frozen, and hydrate-bearing unconsolidated sediments [e.g. Domenico, 1977; Elliot and Wiley, 1975; Nakano and Arnold, 1973; Yun et al., 2005]. Previously published results on dry, water-saturated, frozen, and hydrate-bearing sand are summarized in the following section.

2.2 Previous Studies

P- and s-wave velocities (v_p, v_s) in dry, unconsolidated, non-cohesive sediments have been reported by a number of authors, including Domenico [1977], Yin [1992], Robertson et al. [1995], Aracne-Ruddle et al. [1999]. Zimmer et al. [2007a] compiled the results of many of these studies and showed that the relationship between velocities and effective pressure (P_d = difference between confining and pore pressure) consistently follows a power law, i.e. v_p and v_s are proportional to between $P_d^{1/3}$ to $P_d^{1/6}$. Hysteresis was observed for velocities recorded during loading and unloading processes. Zimmer et al. [2007a] recommended focusing on velocities recorded during unloading as these velocities appear more reproducible. Variability in the data was attributed to differences in porosity and grain shape and sorting, which in turn affect, grain slip and rotation, the increase in number of grain contacts and packing during compaction [Zimmer et al., 2007a; 2007b].

Despite the importance of understanding the effect of pore fluid saturation on elastic velocities, only a few experimental studies have been dedicated to the investigation of partially water-saturated, unconsolidated sediments [Elliot and Wiley, 1975; Domenico, 1977]. In these studies, only small changes in v_p with increasing water saturation were observed until the water saturation reached about 80%. As the sediment approached full saturation, v_p abruptly increased to values higher than the v_p in water [Schön, 1998]. The iso-stress average of gas and water bulk moduli is much smaller than the bulk modulus of water alone [Lee, 2004]. Consequently, v_p becomes very sensitive to small amounts of gas. The shear wave velocity in unconsolidated sand is not affected by the presence of water, though a small decrease in velocity can

generally be observed due to increase in bulk density with increasing water saturation [Schön, 1998].

Both, v_p and v_s increase drastically when water-saturated sediment is subjected to sub-zero temperatures. Frozen, unconsolidated sediments behave similarly to consolidated sediments because ice acts as cement between grains. Several authors reported v_p and v_s velocities for a variety of frozen sediments as functions of ice saturation and/or temperature [Timur, 1968; Nakano et al., 1972; Nakano and Arnold 1973; Kurfürst, 1976; Zimmermann and King, 1986; Jacoby et al., 1996; Wang et al., 2006; Christ and Park, 2009]. Even small ice saturations were sufficient to increase v_p and v_s dramatically. Both velocities increased further with increasing ice content. Depending on the temperature, a certain amount of unfrozen water remains between ice and sediment grains. As temperature decreases, more of the residual water solidifies. Consequently, velocities in ice-bearing sediments tend to increase with decreasing temperatures.

A fairly large number of velocity measurements on gas hydrate-bearing sediments have been published. Table 2.1 presents a summary of all laboratory studies that have been performed on hydrate-bearing sediments to date. These studies cover a broad range of sample characteristics, such as sediment type, porosity, effective pressure, and saturation in addition to the hydrate formation method. The manner of hydrate formation in particular was shown to have a significant impact on the velocities of hydrate-bearing sediment. Dramatic increases in both v_p and v_s were observed when hydrate was synthesized from an excess gas phase in partially water-saturated sediment [Waite et al., 2004; Priest et al., 2009]. Similar to ice, velocities increased with

Table 2.1: Laboratory Studies on Ultrasonic Velocities in Hydrate-Bearing Sediment (*Low frequency measurements ** subsequent H_2O injection, ***use of surfactants)

Publication	Host	Formation	Porosity	S_{GH}	v_p [km/s]
Stoll et al, 1971	Ottawa Sand	CH_4 Injection	unknown	unknown	1.83-2.65
Stoll & Bryan, 1979	Ottawa Sand	C_3H_8-Hyd-Slurry	~0.40	unknown	1.80-2.26
Pearson et al., 1986	Berea Sandstone	THF Hydrate	~0.20	1	4.5
Berge et al., 1999	Unspecified Sand	R11 Hydrate	~0.40	0.00-1.00	1.40-3.81
Collett, 2000	Synthetic Rock	THF Hydrate	~0.26	0.60-1.00	3.26-3.69
Kunerth et al., 2001	Garnet Sand	THF Hydrate	unknown	1	3.6
Waite et al., 2004	Ottawa Sand	CH_4 injection	0.33-0.39	0.19-0.70	3.08-4.00
Spangenberg et al., 2005	Glass Beads	Dissolved CH_4	~0.38	0.00-0.95	2.10-3.75
Yun et al., 2005	Ottawa Sand	THF hydrate	~0.37	0.58-1.00	2.00-3.80
Tan et al., 2005	Quartz Sand	H_2O injection	0.46	0.07-0.34	1.72-2.02
Ebinuma et al., 2008	Natural Core	CH_4 injection**	0.43	0.15-0.75	3.50-3.22
Wang et al., 2008	Unspecified Sand	THF hydrate	unknown	1.00?	3.74
Wang et al., 2008	Unspecified Sand	GH-Sand-Mix	unknown	unknown	2.90
Priest et al., 2009*	Leighton Buzzard	H_2O injection	0.40-0.42	0.00-0.40	1.66-2.01
Kwon and Cho, 2009	Ottawa Sand	CO_2 (g) injection	0.40	0.25-0.49	1.66-2.73
Hu et al., 2010	Synthetic Rock	Dissolved CH_4***	~0.42	0.00-0.70	4.25-4.50
Saito et al., 2010	Toyura Sand	CH_4 injection	~0.41	0.04-0.86	1.86-2.91
Ren et al., 2010	Quartz Sand	CH_4 injection	unknown	0.00-0.67	1.75-3.66
Lee et al., 2010	Various	THF hydrate	various	0.0,0.5,1.0	1.48-4.20
Espinoza et al. 2011	Ottawa Sand	Ice seeding	0.42	0.05-0.37	Unknown
ILCP, 2011	Ottawa Sand	CH_4 injection	~0.4	0.2-0.4	1.40-3.20

increasing hydrate saturation. When hydrate was formed in the presence of an excess water phase, only a moderate increase in velocity was observed [Priest et al., 2009; Hu et al. 2010]. Hydrate formation out of solution - using either THF or dissolved CH_4 - did not impact v_p and v_s significantly until hydrate saturations exceeded 30-50% [Yun et al., 2005; Spangenberg et al., 2008]. Even then, both velocities only moderately increased with growing hydrate saturation. Very few studies focused in the effective-pressure dependence of v_p and v_s in ice- or hydrate-bearing sediments [Priest et al., 2009; Waite et al., 2011; Lee et al., 2010].

2.3 Methodology

In the following, the experimental setup used to measure the ultrasonic velocity of dry, partially water-saturated, frozen, CH_4 hydrate and THF hydrate-bearing sandpacks is described and the preparation of the different specimen is detailed.

2.3.1 Experimental Equipment

We designed and built an experimental setup that allows us to measure p- and s-wave velocities in sediments during gas hydrate formation and dissociation under in-situ conditions (Figures 2.1 and 2.2). The experimental setup consists of a temperature-controlled pressure vessel filled with hydraulic oil which confines an instrumented sample holder. The sample is jacketed with flexible Tygon tubing and sandwiched between a pair of 1-inch diameter PEEK end caps that contain 500 kHz piezoelectric p-wave crystals and ports to enable fluid circulation through the sample and pore-pressure control. Two k-type thermocouples are placed outside the sample holder to

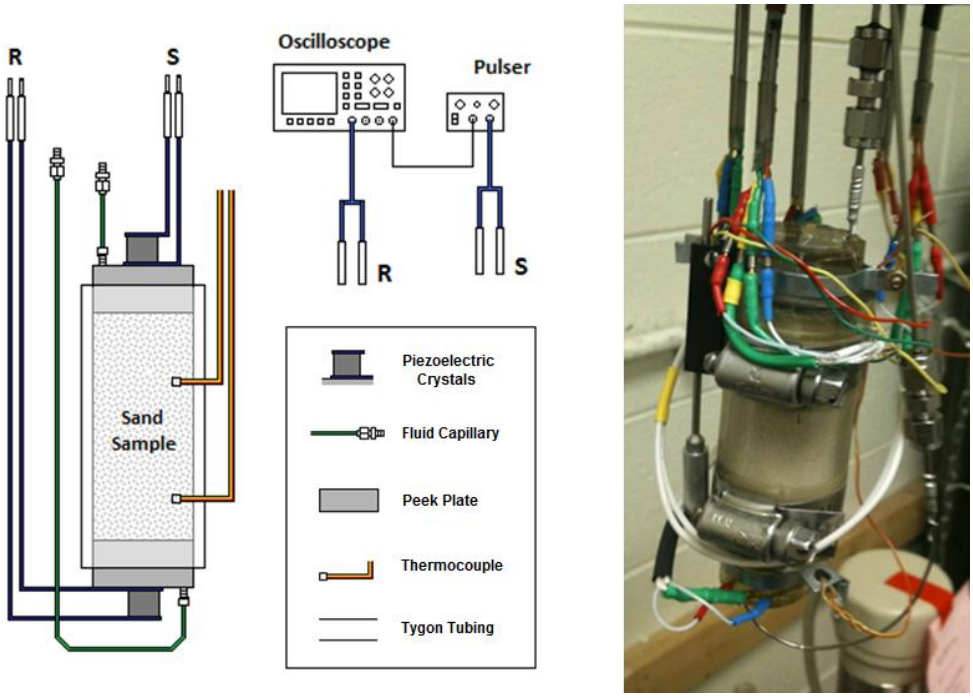

Figure 2.1: Instrumented sample holder for ultrasonic velocity measurements (sample diameter 1 inch)

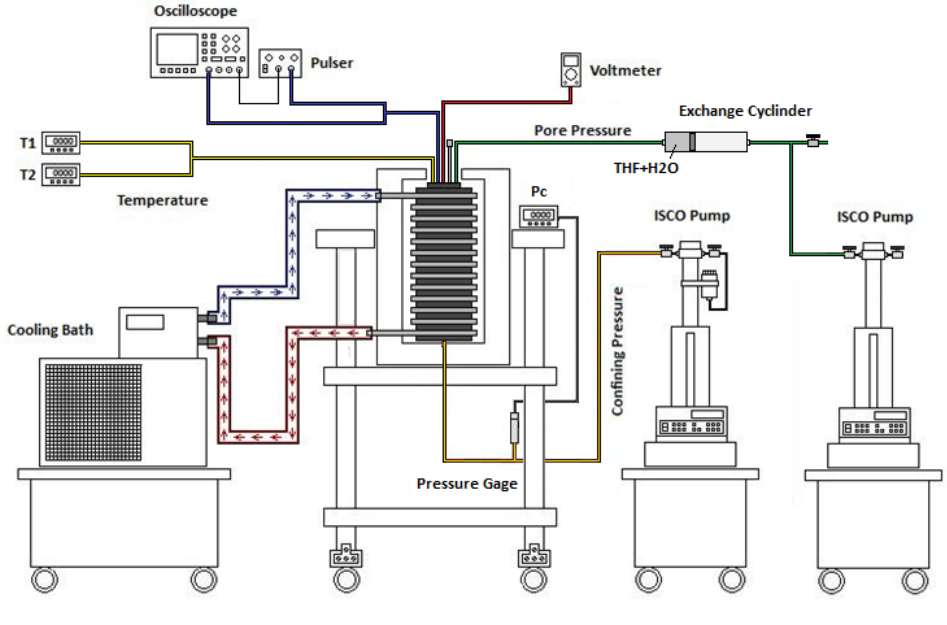

Figure 2.2: Peripheral experimental setup for ultrasonic velocity measurements in hydrate-bearing sediment under reservoir conditions. The voltmeter is used to measure the changes in resistance in the linear potentiometer, which is related to changes in sample length.

monitor the sample temperature with an accuracy of ±0.5ºC. Furthermore, linear potentiometers are attached to top and bottom end caps to measure the changes in length (±0.2 mm) when the sample is subjected to pore and confining pressure. A maximum confining pressure of 20 MPa can be applied to the sample at temperatures down to -10°C. The pressure vessel is cooled by circulating ethylene glycol (antifreeze) from a cooling bath through a copper coil that is wrapped around the insulated pressure vessel. Temperatures and the pressure inside the pressure vessel are logged continuously. Both pressures are controlled by external ISCO pumps with an accuracy of ±1.5 %.

2.3.2 Sample Preparation and Procedures

Ottawa sand F110 was used to prepare all the samples investigated. This type of Ottawa Sand is mainly composed of quartz (>99%) and has a density of 2650 kg/m^3 (Product Data Sheet). Figures 2.3 and 2.4 show micro X-ray CT images of dry and partially water saturated Ottawa sand F110, respectively. Due to capillary forces, the water in the partially saturated sample (Figure 2.4) prefers to sit in smaller pores and forms small clusters, but tends to be distributed throughout the sample fairly homogeneously. The grain size ranges from 50.2 to 355.7 microns. In total, 16 samples were tested; 3 of which were dry Ottawa sand, 5 partially water saturated, 3 frozen, as well as 3 CH_4 hydrate-bearing, and 7 THF hydrate-bearing. Porosity and initial water saturation for each specimen are displayed in Figure 2.5.

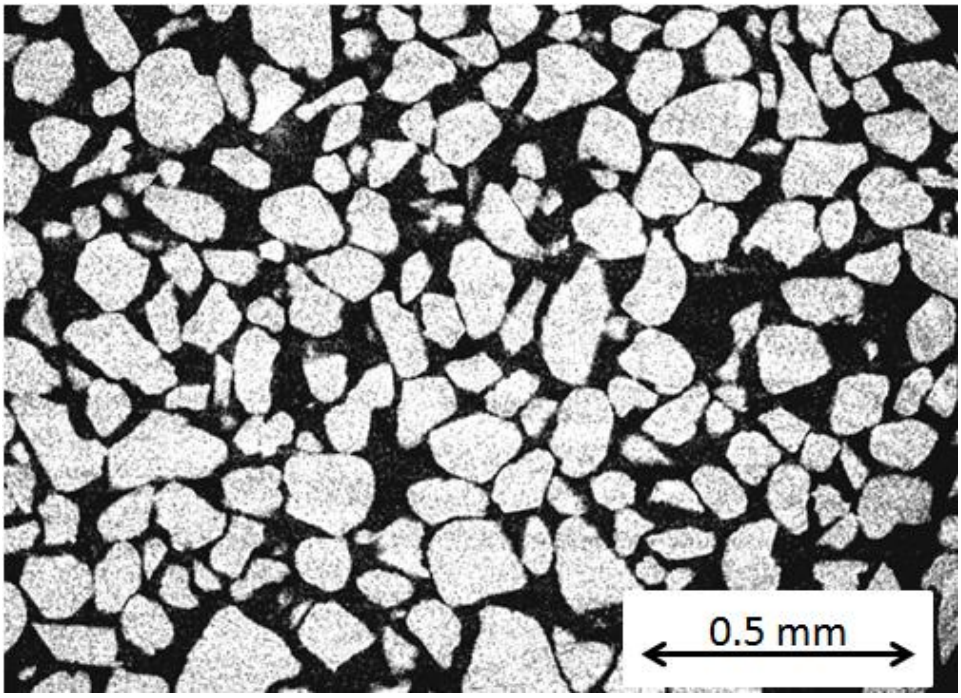

Figure 2.3: Micro X-Ray Computed Tomography images of dry Ottawa Sand F110 (light grey areas depict the sand grains and black background represents air)

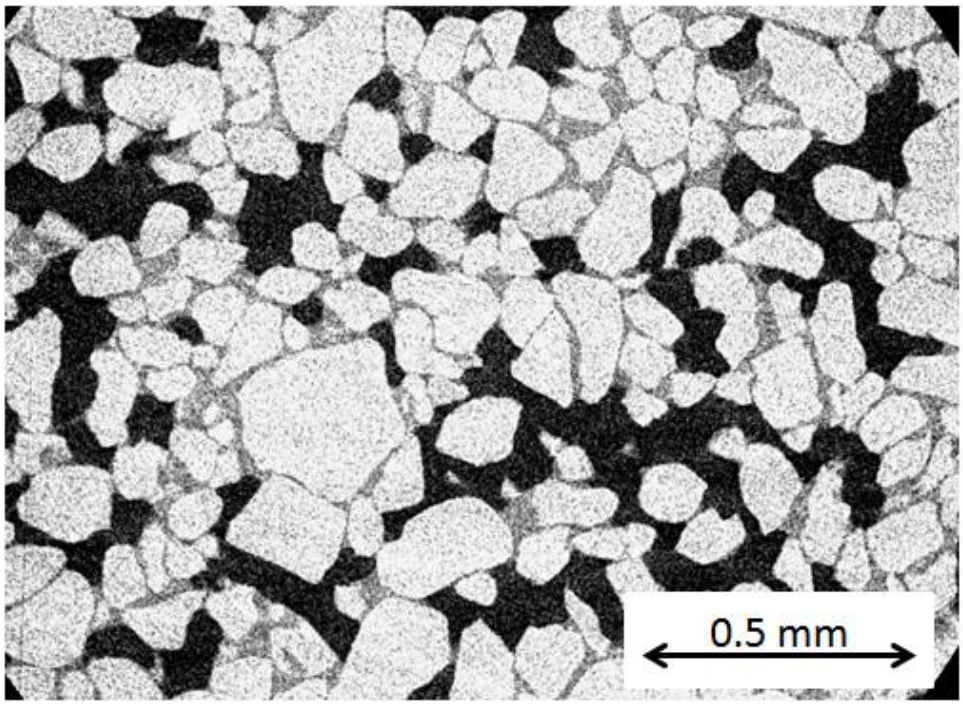

Figure 2.4: Micro X-Ray CT images of partially water-saturated Ottawa Sand F110 (light grey areas depict the sand grains, medium grey and black areas represents water and air, respectively). The water forms patches in areas with smaller pore sizes

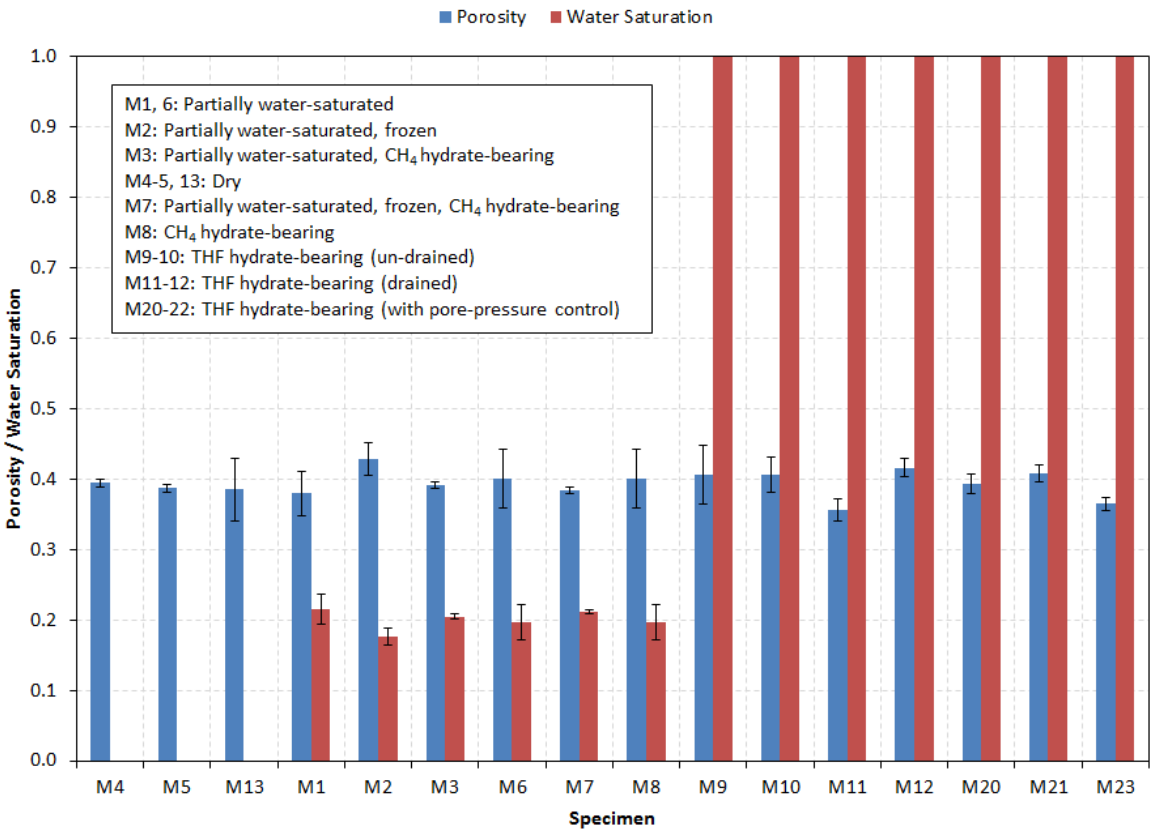

Figure 2.5: Porosity and water saturation calculated for the individual Ottawa sand specimen

2.3.2.1 Dry, Wet, and Frozen Sand Samples

To prepare a dry specimen, one transducer end piece was inserted into the Tygon tube and 16.1±0.05 g of dry Ottawa Sand was scooped into the opening. The sample holder was closed with the second end piece and the sandpack compacted to a designated length of about 2 cm, yielding a target porosity (ϕ) of about 40%. For the partially water-saturated samples, 16.1±0.05 g dry sand and 0.8 g de-ionized water were mixed thoroughly in a plastic bag. The wet sand was then filled into the sample holder and compacted in two layers with a tamping stick. Porosity and initial water saturation (S_{wi}) of the wet samples were targeted as 40% and 20%, respectively. The length of each sample was measured with either a ruler, caliper and/or based on micro X-ray CT (MXCT) scans (Figure 2.6). Knowing the sample diameter (D), sample length (L), as well as sand and water mass (m_s, m_w) and densities (ρ_s, ρ_w), S_{wi} and ϕ were calculated using the following equations:

$$\phi = \frac{V_{pore}}{V_{tot}} = 1 - \frac{V_s}{V_{tot}} = 1 - \frac{m_s/\rho_s}{(D/2)^2\pi L} \quad (2.1)$$

$$S_{wi} = \frac{V_w}{V_{pore}} = \frac{V_w}{\phi V_{tot}} = \frac{m_w/\rho_w}{\phi \cdot (D/2)^2\pi L} \quad (2.2)$$

In Equations 1 and 2, V_{tot}, V_{pore}, V_s, V_w denote the volumes of the total sample, pore space, sand, and water, respectively. Each prepared specimen was placed in the pressure vessel and subjected to an initial confining pressure of 435 psi (3 MPa). The pore pressure remained at atmospheric conditions while the confining pressure was raised to 2175 psi (15 MPa) and then lowered back to 435 psi (3 MPa) in increments of 1 MPa (145 psi). Three of the partially water-saturated samples were then cooled down

from room temperature to -5°C over the course of a few days. After 24 hrs at -5°C, the sample was subjected to another incremental confining-pressure cycle. We recorded p- and s-waveforms at every pressure step.

2.3.2.2 CH_4 Hydrate-Bearing Sand Samples

CH_4 hydrate-bearing samples were formed by injecting CH_4 into partially water-saturated sand packs. The wet sand packs were prepared as described above and installed inside the pressure vessel. A confining pressure of 1635 psi (11.27 MPa) was applied before CH_4 was injected. The pore pressure was raised to 1200 psi (8.27 MPa) yielding a effective pressure of 435 psi (3 MPa). Then the pressure vessel temperature was decreased into the CH_4 hydrate stability zone (Figure 2.7) with a cooling rate of approximately 0.05-0.10 °C/min. The equilibrium temperature of CH_4 hydrate at 8.27 MPa is 11.2°C (calculated with CSMGem; Sloan and Koh, 2008). A significant increase in ultrasonic velocities indicated the beginning of hydrate formation. When formed from a free CH_4 phase, a hydrate layer is formed at the CH_4-H_2O interface which provides a barrier between the remaining gas and H_2O. Consequently, after a fast initial hydrate growth period, the hydrate formation rate slows down significantly as the CH_4 has to diffuse through the initial hydrate layer [Waite et al. 2004; Howard et al. 2011]. Accordingly, the rate at which velocity increased slowed down as well. When the ultrasonic waveforms remained unchanged for more than 12 hours, the CH_4 hydrate-bearing sandpack was subjected to confining pressure testing.

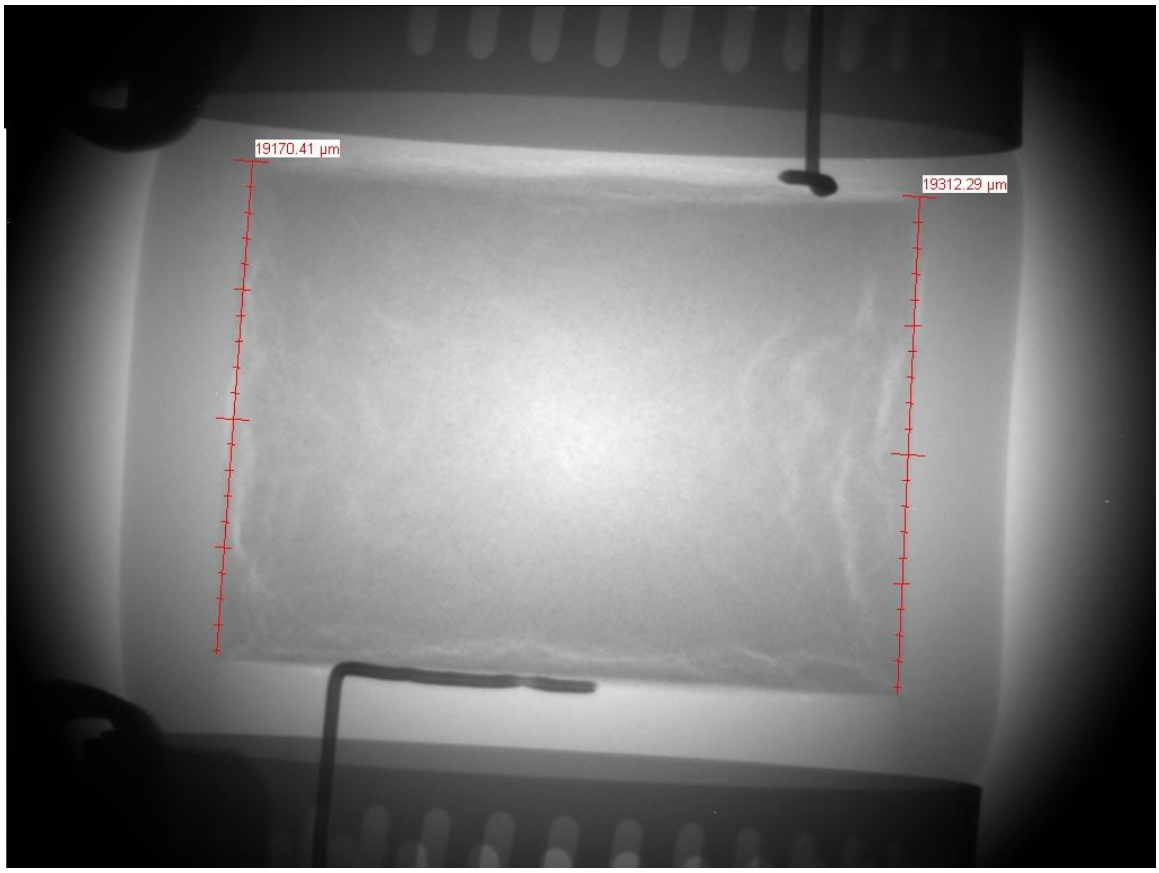

Figure 2.6: Example of 2-D micro X-ray CT image of sand specimen used for length measurements

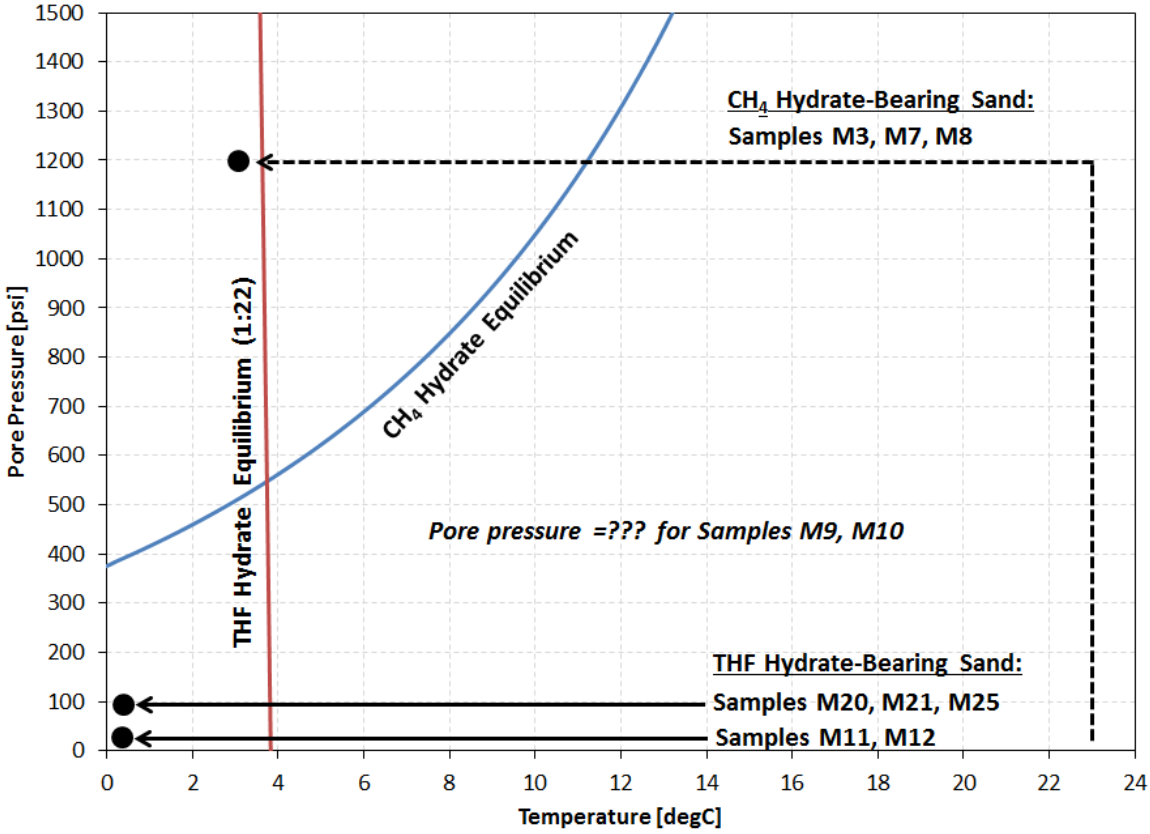

Figure 2.7: CH_4 and THF hydrate stability curves and temperature-pressure paths for the formation of the hydrate-bearing samples (CH_4 hydrate stability calculated using CSMGem (Sloan & Koh, 2008), THF phase equilibrium after Gough & Davidson [1971]). The THF-H_2O was mixed with a molar ratio of 1:22 which yielded a THF hydrate saturation of ~80%.

2.3.2.3 THF Hydrate-Bearing Sand Samples

To form the THF hydrate-bearing samples, we prepared dry sandpacks as described above. The dry samples were placed inside the pressure vessel and a vacuum was applied to each specimen for at least 2 hours. THF hydrates were formed from a solution composed of 15 wt% THF and 85 wt% de-ionized H_2O which yielded a THF hydrate saturation of about 80% with the rest of the pore space filled with water [Yun et al. 2005]. The THF-H_2O mixture was injected from the transfer vessel into the sandpacks. Pore and confining pressure were raised to 0.69 MPa (100 psi) and 3.69 MPa (535 psi) to produce an effective pressure of 3 MPa (435 psi) before the pressure vessel was cooled down to about 0.8±0.2°C. The equilibrium temperature for THF hydrate formed from this mixture is 3.9°C at atmospheric pressure (Figure 2.7). Increasing velocities indicated that THF hydrate had formed. As opposed to CH_4 hydrate, there is no diffusive barrier in THF hydrate formation, which is generally complete within a few hours. 24 hrs after initial hydrate formation was observed, the confining pressure cycle was applied to the sample.

2.4 Results and Discussion

Figure 2.8 shows examples of typical p- and s-waveforms recorded for dry, partially water-saturated (at both room temperature and -5°C) and fully THF-H_2O-saturated, as well as CH_4 and THF hydrate-bearing Ottawa Sand F110. The effective pressure for all waveforms shown was 3 MPa (425 psi). Arrows in Figure 2.8 indicate where arrival times for p- and s-waves were picked in these waveforms.

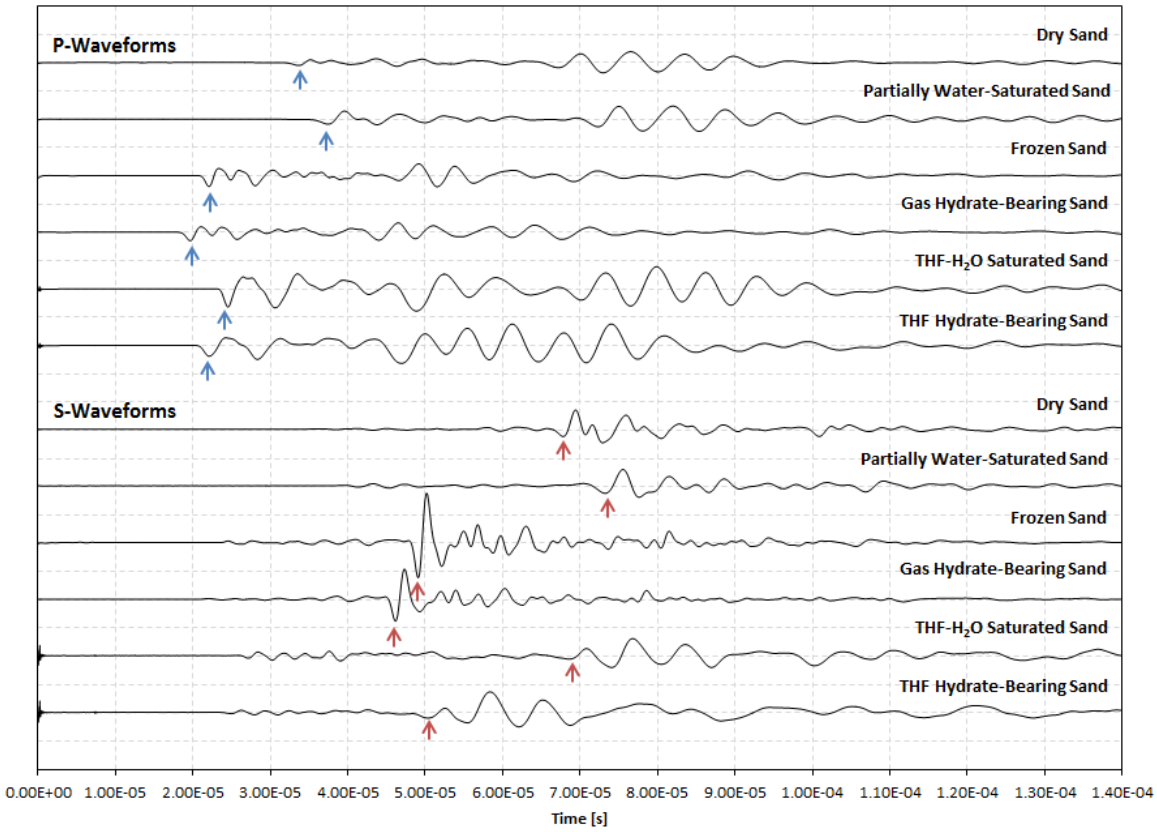

Figure 2.8: Waveforms recorded for different sample types. Arrows indicate the arrival time picks for the p- and s-waves

The respective velocities were calculated using Equation 3, where L is the initial length of the sample, t is the picked traveltime, DL is the change in length due to the applied confining pressure, and Dt is the traveltime of pulse with the transducer end caps in contact only with each other (dead-time).

$$v = \frac{L-DL}{t-Dt} \tag{2.3}$$

Dt showed temperature-dependency as the elastic properties of PEEK changed with temperature (T). Consequently, we calibrated the Dt as a function of temperature. The fits for Dt_p and Dt_s as functions of temperature (T) and the corresponding R^2-values are given by Equations 2.4 and 2.5, respectively.

$$Dt_P = (0.0135\,T[℃] + 14.714)\ \mu s \quad \text{with} \quad R^2=0.8551 \tag{2.4}$$

$$Dt_S = (0.0409\,T[℃] + 37.575)\ \mu s \quad \text{with} \quad R^2=0.8332 \tag{2.5}$$

2.4.1 Velocities in Dry, Partially Water-Saturated, and Frozen Sand

Figure 2.9 shows V_p and V_s recorded for dry Ottawa Sand F110 at effective pressures between 435psi (3 MPa) and 2715 psi (15 MPa). Both velocities showed noticeable hysteresis in their effective-pressure (P_d) dependency due to the compaction during loading. Only data obtained during unloading are depicted in Figure 2.9. When P_d was reduced from 2175 to 435 psi, v_p decreased from about roughly 1300 to 1000 m/s and v_s from 900 to 700 m/s. The relationship between P_d and velocities followed a power-law type relationship, where v_p and v_s were proportional to $P_d^{1/5}$. The measured

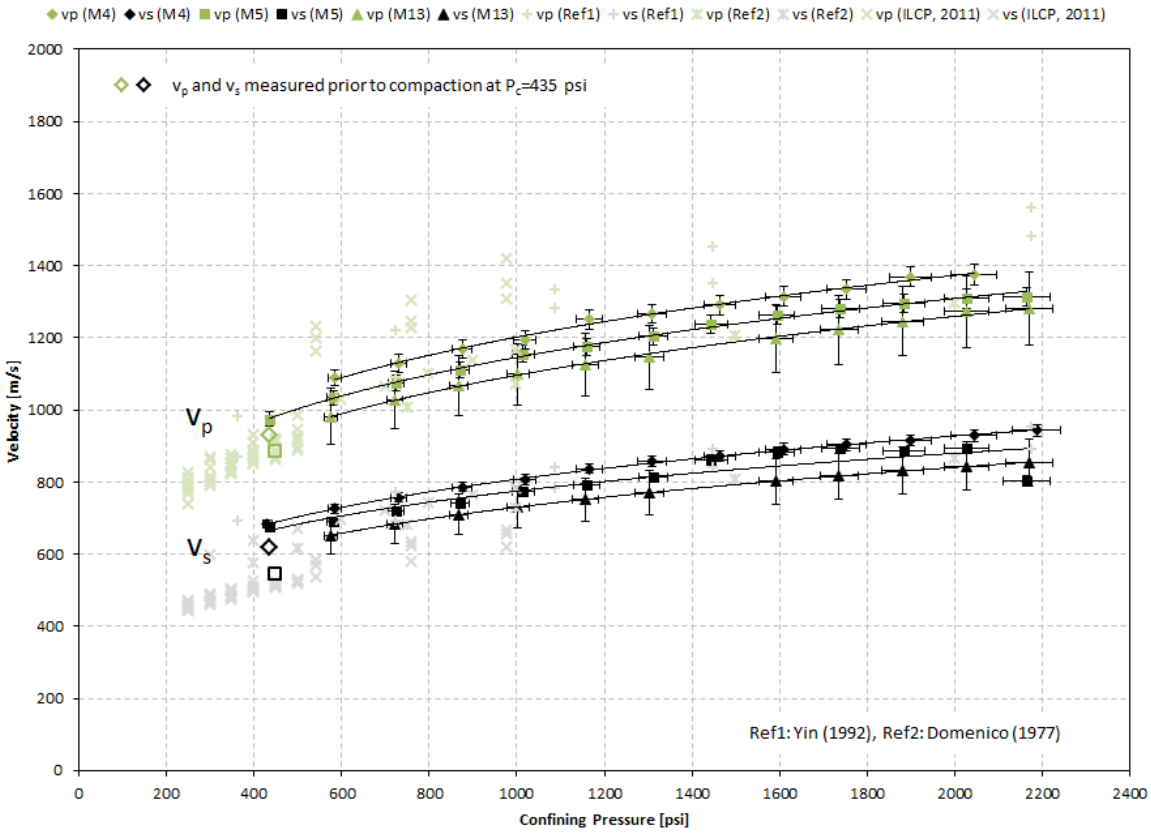

Figure 2.9: P- and s-wave velocities of dry Ottawa Sand F110 (in comparison with literature values)

v_p-v_s ratio was 1.50±0.05. These results are in good agreement with observations of previous studies [Domenico, 1977; Yin, 1992; Zimmermann et al., 2007a; Waite et al., 2011]. The respective data points all fell within ±100 m/s. We attributed the offset between our own measured velocities to sample packing and porosity differences [Zimmermann et al., 2007b]. In comparison, velocity data reported by the various authors exhibited a wider scatter due to dissimilarities in sample preparation and measurement procedures in addition to differences in specimen make-up [Waite et al., 2011]. Our data set best matched v_p and vs reported for Ottawa Sand by Domenico [1977].

Velocities recorded for partially water-saturated sandpacks (S_w=20%) during unloading are presented as a function of P_d in Figure 2.10. The partially water-saturated samples showed less hysteresis than the dry samples. The exponent of the pressure-dependency (1/n), however, is minimally elevated compared to dry sand with n=4.5. During unloading, v_p decreased from about 1200 to 950 m/s, and v_s from 800 to 550 m/s. As expected, v_p and v_s are slightly smaller compared to measurements in dry sand due to the increased bulk density with water added. As discussed earlier, the bulk modulus is not expected to increase significantly until the sample approaches full saturation [Schön, 1998]. Similar to the dry samples, velocity measurements were repeatable within ±100 m/s and showed good agreement with the majority of the literature data [Waite et al., 2011]. This gives us confidence that our preparation method for partially water-saturated samples provides specimens with reproducible water distributions.

Four of the five partially water saturated samples were frozen at -5°C. The results are depicted in Figure 2.11. As expected, hysteresis for the velocity data was negligible due to cementation of the unconsolidated sand grains by ice. Due to the increased sediment stiffness, values of v_p and v_s, for most samples more than doubled during freezing. v_p and v_s measured for the frozen samples were about 2600 m/s and 1700 m/s, respectively. Also, most frozen samples exhibited a decreased sensitivity to changes in P_d, and values for n increased above 20. The results for v_p and v_s showed a considerably higher variability than was observed for the previous tests of dry and partially water-saturated samples. Both v_p and v_s were scattered by ±200 m/s and n varied between 21 and 32. The data spread was comparable to that observed for frozen samples tested within the framework of the ILCP (Figure 2.11).

As was discussed above, v_p and v_s in frozen, unsaturated sediment primarily depend on temperature, ice saturation, and ice distribution. Nakano and Arnold [1973] measured v_p in Ottawa Sand as a function of ice saturation and temperature. Their results showed that at low ice saturations and temperatures below -4°C, the temperature impacts v_p to a much lesser degree than the ice saturation. Temperatures differences between samples were less than 0.5°C. Ice saturations may have varied between ±0.02 among the samples, which may have caused the differences in velocities measured. In addition, the freezing process may have caused water migration inside the sample. Water in sediment, as the sediment cools, tends to migrate toward the areas of initial ice formation [Waite et al., 2011]. All specimens in this study were cooled from the outside, which most likely caused a radial temperature gradient. In addition, cooling fluid circulates through the cooling coil from top to bottom, which may

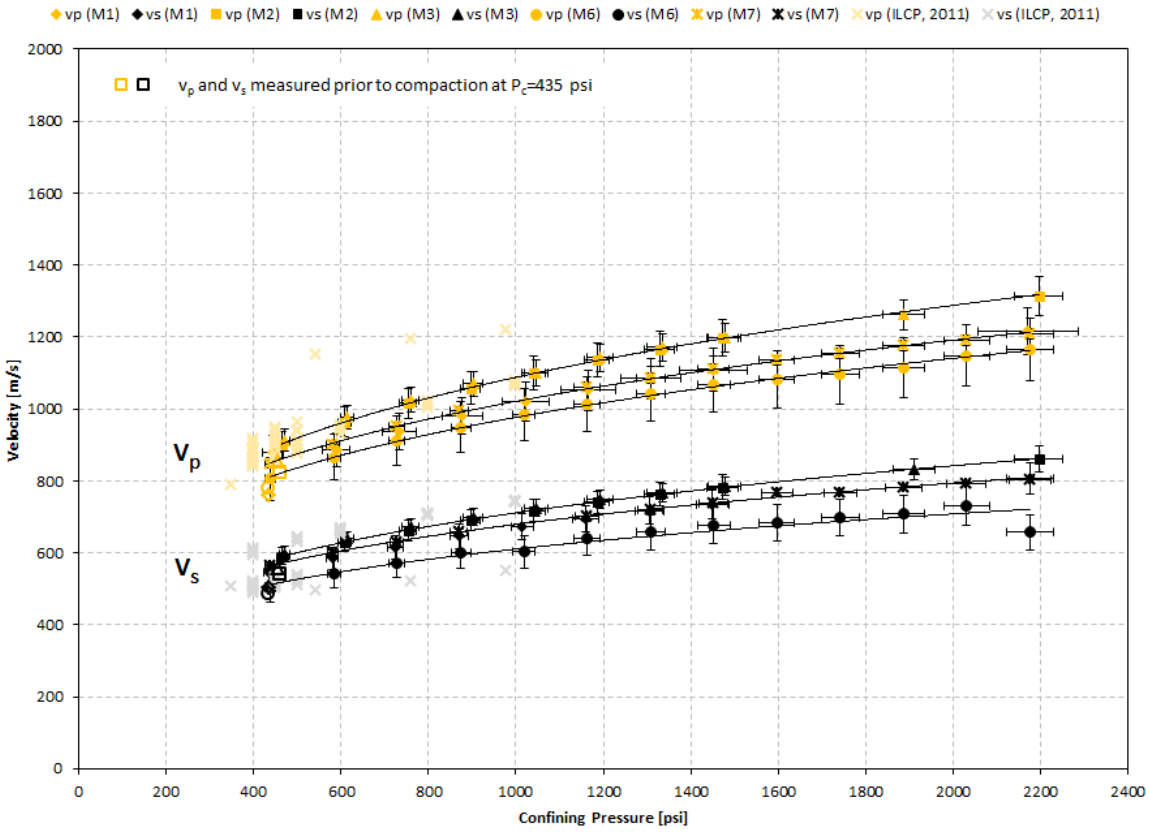

Figure 2.10: Results for p- and s-wave velocities of partially water-saturated Ottawa Sand F110

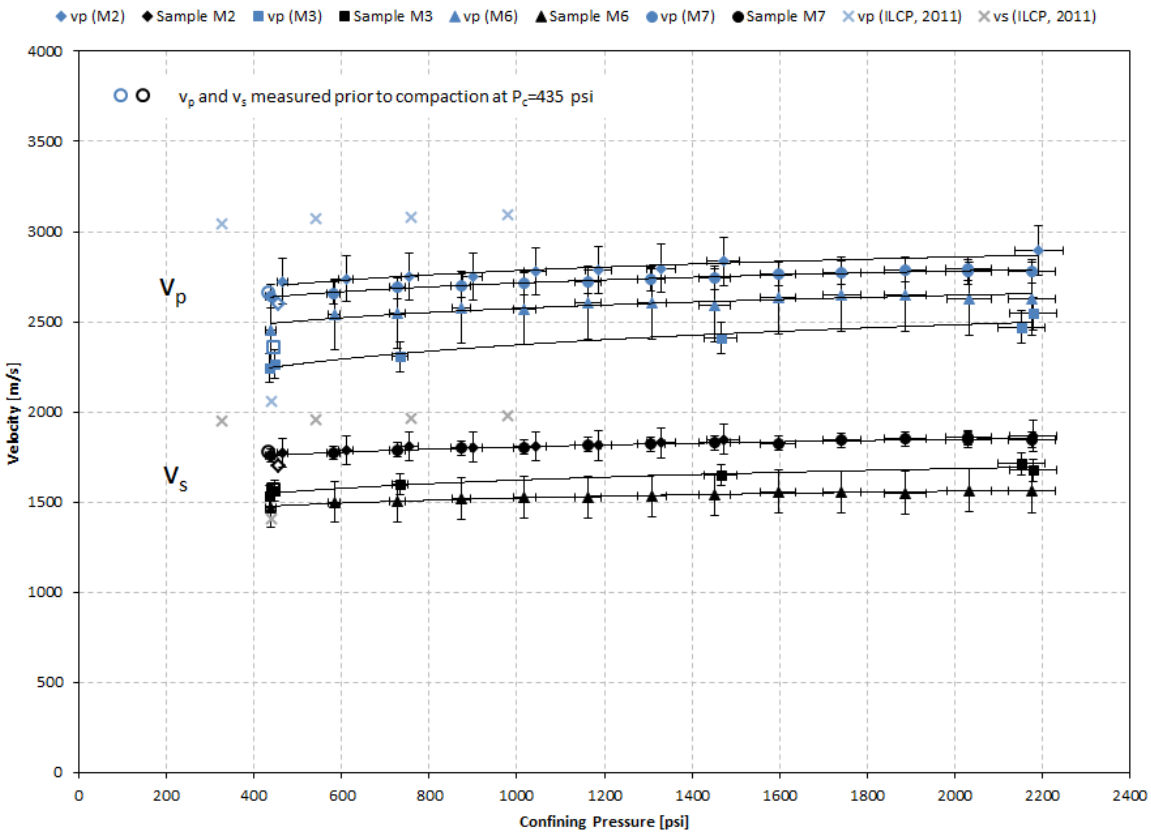

Figure 2.11: Results for p- and s-wave velocities of partially water-saturated frozen Ottawa Sand F110

have produced an axial temperature gradient inside the pressure vessel as well. Consequently, water may have moved up and to the sides, to areas of initial ice formation. On the other hand, the sample size was relatively small (2.54 cm in diameter, 2.00 cm in length). It is thus difficult to assess if small inconsistencies in the cooling procedure alone could have produced differences in the ice distribution that resulted in the observed spread in results.

2.4.2 Velocities in CH_4 Hydrate-Bearing Sand

Results for the CH_4 hydrate-bearing samples are shown in Figure 2.12. For all samples, a significant increase in both v_p and v_s was observed as a result of hydrate formation. Velocities measured in hydrate-bearing samples exhibited lower-level sensitivity to loading and unloading compared to the partially water-saturated specimens. Values recorded for v_p and v_s and n varied significantly from sample to sample. As with ice, we obtained highly variable values for n, which ranged from 11 to 27. Similar to ice, the velocity of CH_4 hydrate-bearing sediment formed through gas injection into partially water-saturated sediment depends on the hydrate saturation and distribution, as well as the amount of residual, unconverted water. All these properties are related to how water is initially distributed throughout the sample. Consequently, we attributed the high level of variability in recorded velocities to heterogeneous water distributions inside the sample prior to hydrate formation.

A main concern is the formation of water patches through fluid accumulation in smaller pores that depletes the surrounding areas. The patchy saturation impacts the overall velocity due to the velocity contrast between hydrate saturated and dry areas

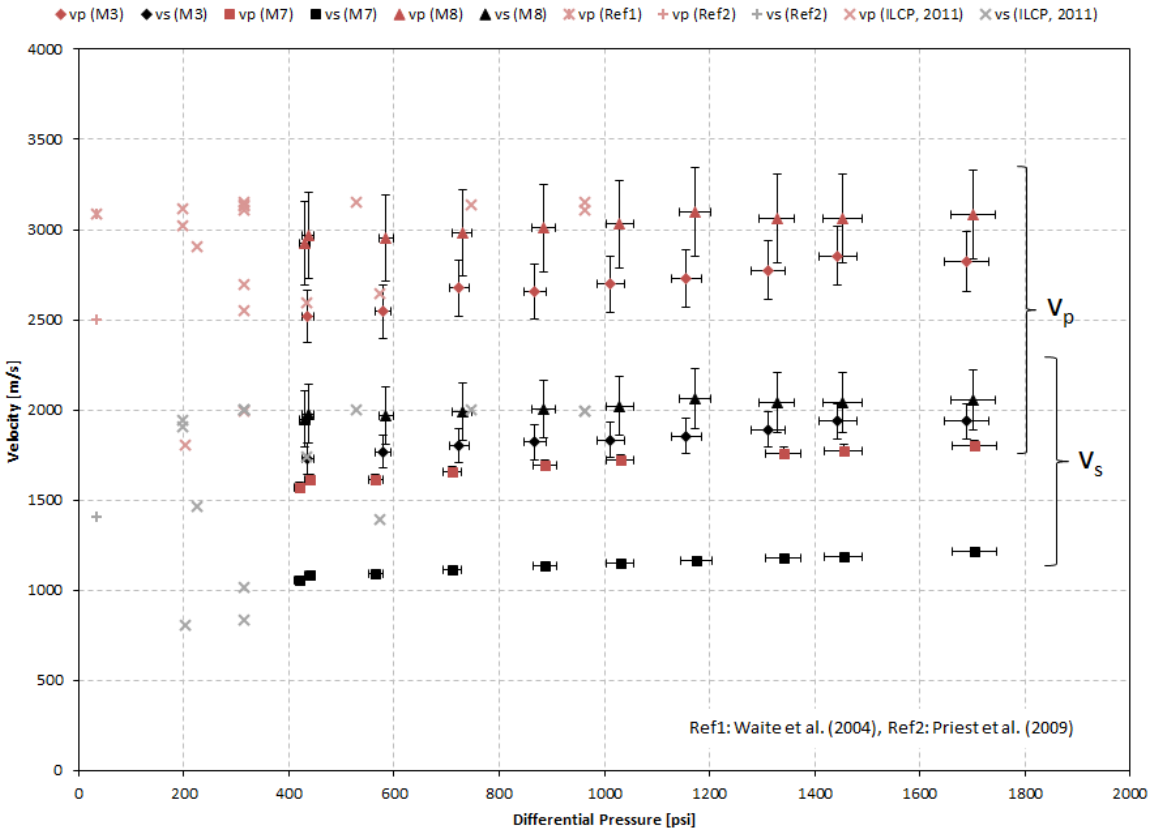

Figure 2.12: Results for p- and s-wave velocities of CH_4 hydrate-bearing Ottawa Sand

[Waite et al., 2011]. It may also lead to misinterpretation of the point where the recorded velocity approaches a constant value and complete conversion of water to hydrate is assumed. When gas hydrate forms from a free gas phase, it grows as a layer on the gas-water interface, which slows down the hydrate formation rate significantly as the gas molecules are required to diffuse through the hydrate layer to reach the water. In samples with patchy water distributions, the drop in hydrate formation rate can easily be interpreted as velocity stabilization due to water conversion nearing completion, even though relatively large amounts of unconverted water remain separated from the hydrate-forming gas phase.

Note that Sample 3 and 7 had already been frozen, melted and undergone several cycles of loading and unloading. All processes are likely to change the initial water distribution inside the sample. Sample M8 was a “fresh” sample that had not undergone freezing or compaction prior to hydrate formation. The highest values of v_p and v_s were recorded for this sample, which implies that it contained a higher amount of hydrate that was distributed more evenly compared to Samples M3 and M7. In addition to freezing, thawing, and the pressure cycle, the CH_4 inflow into the sample during pore-pressurization may have caused an uneven redistribution of the pore water. As the gas influx was controlled manually with a gas regulator, variations in flow rate can be expected. In conclusion, a key to improving reproducibility of velocity measurements of CH_4 hydrate-bearing sediments is to insure an even water saturation. This could be accomplished by using fresh samples and use pump-controlled, lower CH_4 injection rates. In addition, a means of monitoring the hydrate saturation and, ideally, the hydrate distribution should be implemented. This may achieved by accurately measuring the

gas consumption [Sloan and Koh, 2008] or using imaging techniques such as MRI [Baldwin et al., 2003] or X-ray CT [Kneafsey et al., 2007; Seol and Kneafsey, 2011]. (Note that the MXCT scanner used for measuring the sample length was not equipped with means of pressure-temperature control and could consequently not be used to characterize the ice or hydrate distribution inside a sand pack)

2.4.3 Velocities in THF Hydrate-Bearing Sand

Figure 2.13 shows v_p and v_s recorded under varying effective pressure (constant pore pressure) for THF hydrate-bearing sediments with a hydrate saturation of S_h=80%. Under THF hydrate formation v_p and v_s increased in Samples M20 and M21 by over 700 m/s (Table 2.2) at P_d=435 psi (3 MPa). The exponents of the pressure-dependency were determined as n=14±1 for both velocities in both samples. The velocities measured for Sample M25 deviated from those measured for the other two samples at lower effective pressures. With increasing confining pressure, all velocities approached the same value (±75 m/s). Even though the Sample M25 had been vacuumed prior to injection of the THF-H_2O solution, some air may have been remained in the sample, decreasing the overall velocity. Under loading, the air bubbles may have moved out of the sample with the drained water, thereby bringing the sample velocity up close to the levels recorded for M20 and M21. All data points recorded for each, v_p and v_s fell within 300 m/s.

Figure 2.14 shows the results in comparison with velocities we recorded under varying confining pressure for an additional two sets of THF hydrate-bearing sediments. Two THF hydrate-bearing specimens were prepared for each set using different sample

preparation methods. To prepare samples M9 and M10, the THF-H_2O solution was injected manually using a syringe. Following the fluid injection, the sample was sealed so no fluid could move in or out of the sample when applying a confining pressure. Samples M11 and M12 were drained prior to loading after THF hydrate formation had formed. Consequently, the main distinction between the different samples was the pore pressure that the THF hydrates were exposed to.

Table 2.2: Velocities measured in THF hydrate-bearing sand

	Before hydrate formation		After hydrate formation	
Sample	v_p [m/s]	v_s [m/s]	v_p [m/s]	v_s [m/s]
M20	1991±88	534±21	2476±118	1323±53
M21	1953±82	521±20	2717±114	1282±50
M23	1911±78	596±22	2476±102	1035±38

A volume increase can generally be observed when hydrate is formed, which will cause the pore pressure to increase during hydrate formation in Samples M9-M12 in their closed systems. Samples M11 and M12 were drained after hydrate formation allowing the excess pore pressure to be released from the interconnected areas (at 80% saturation, hydrate may have clogged pore throats, thereby trapping part of the remaining pore fluid). Sample M9 and M10 remained sealed. As the confining pressure increased, the pore pressure increased as well, thereby keeping the effective pressure it constant, which can explain why these samples exhibited lower v_p compared to the other THF hydrate-bearing samples. Samples M20, M21, and M25 were subjected to a constant pore pressure of 100 psi, and Samples M11 and M12 were measured with

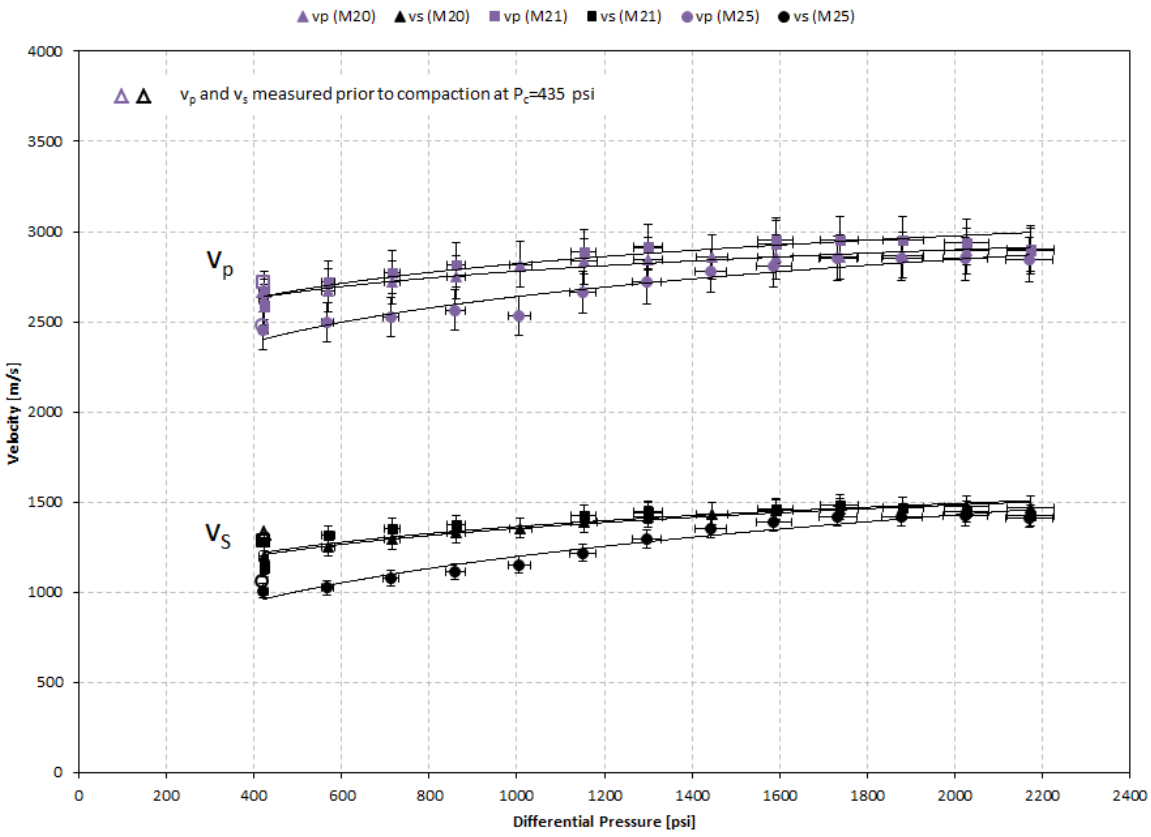

Figure 2.13: Results for p- and s-wave velocities of THF hydrate-bearing Ottawa Sand

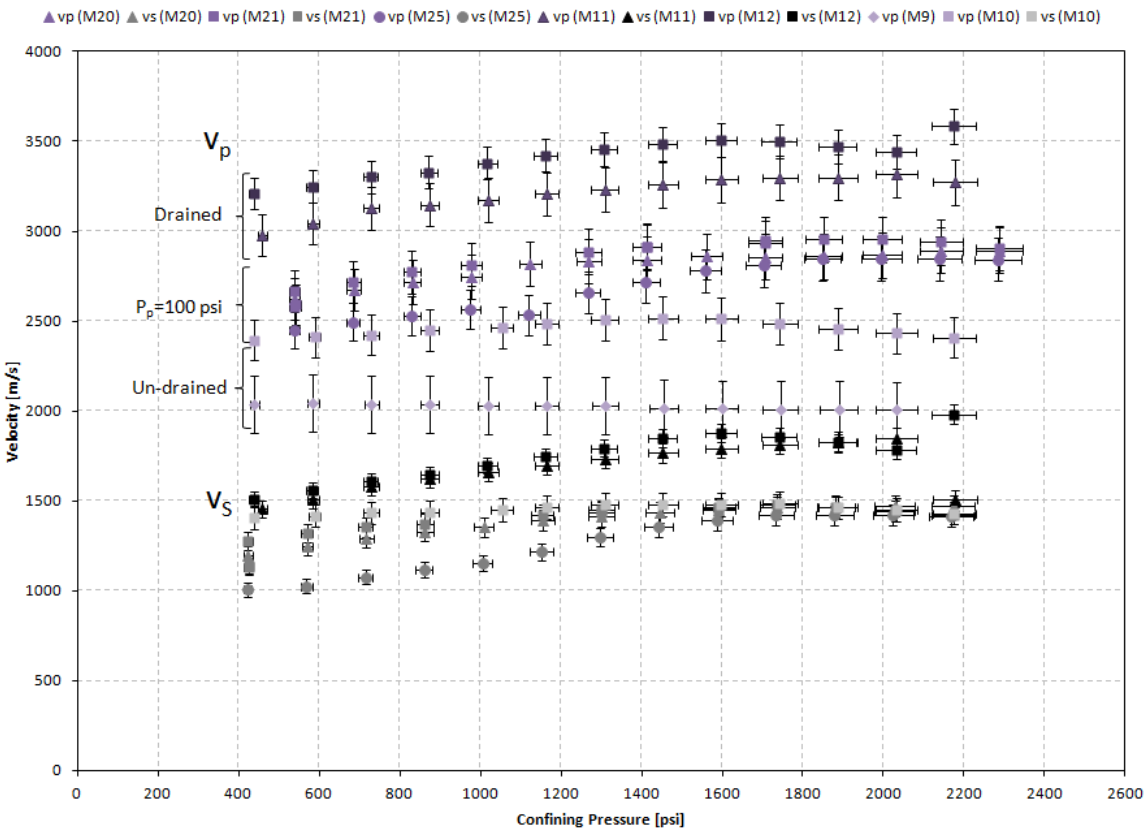

Figure 2.14: Results for p- and s-wave velocities of THF hydrate-bearing Ottawa Sand

atmospheric pore pressure. The effective pressure was the same for these two sets of samples. As can be seen in Figure 2.14, at constant effective pressure, higher v_p were recorded in THF hydrate-bearing samples with lower pore pressures. This result was counter-intuitive as we expected v_p to increase due to a lower possibility of gas bubbles in the pore fluid. Note that in Samples M9 and M10, v_p decreases at higher confining pressures, i.e. as higher pore pressures are generated. These observations suggest that in addition to the THF-H_2O ratio, the THF hydrate saturation may depend on the prevalent thermobaric conditions as well.

2.4.4 Error Analysis

The error for the ultrasonic velocities (Δv) is given by Equation 6, where ΔL, Δt, ΔDL, and ΔDt are the errors for the average initial sample length (L), traveltime of the ultrasonic pulse (t), change in length due to the confining pressure (DL), and the dead time correction (Dt), respectively.

$$\Delta v(L, DL, t, Dt) = \sqrt{\left(\frac{\partial v}{\partial L}\Delta L\right)^2 + \left(\frac{\partial v}{\partial DL}\Delta DL\right)^2 + \left(\frac{\partial v}{\partial t}\Delta t\right)^2 + \left(\frac{\partial v}{\partial Dt}\Delta Dt\right)^2} \quad (2.6)$$

The partial differential can be expressed as follows:

$$\frac{\partial v}{\partial L} = \frac{\partial}{\partial L}\left(\frac{L-DL}{t-Dt}\right) = \frac{1}{t-Dt} \quad (2.7)$$

$$\frac{\partial v}{\partial DL} = \frac{\partial}{\partial DL}\left(\frac{L-DL}{t-Dt}\right) = -\frac{1}{t-Dt} \quad (2.8)$$

$$\frac{\partial v}{\partial t} = \frac{\partial}{\partial t}\left(\frac{L-DL}{t-Dt}\right) = -\frac{(L-DL)}{(t-Dt)^2} \quad (2.9)$$

$$\frac{\partial v}{\partial Dt} = \frac{\partial}{\partial Dt}\left(\frac{L-DL}{t-Dt}\right) = \frac{(L-DL)}{(t-Dt)^2} \quad (2.10)$$

The partial differentials (Equations 7-10) are substituted into Equation 6, which can then be simplified into Equation 11, where ∆v/v is the relative error for v.

$$\frac{\Delta v}{v} = \sqrt{\frac{\Delta L^2+\Delta DL^2}{(L-DL)^2} + \frac{\Delta t^2+\Delta Dt^2}{(t-Dt)^2}} \quad (2.11)$$

Table 2.3 lists the initial sample lengths (L) which were measured with either a ruler, a digital caliper, or based on MXCT images that were acquired from perpendicular sides. The ruler and caliper measured L with precisions of ΔL'=±1.0 and ±0.5 mm, respectively. Length measurements based on MXCT scans (Figure 2.6) depended on the pixel size of image the MXT image and exhibited a precision of ΔL'=±0.1 mm.

The transducer endplates were not perfectly parallel, so for most samples, L was measured at different locations arount the sample. The error associated with the sample skewness (ΔL*) was taken as the standard deviation of L measured at varying azimuthal angles. In the few cases where only one value for L was obtained for a sample, ΔL* was assumed to be ±1.0 mm. The error for length measurements were calculated as the sum of ΔL' and ΔL*. The reduction of sample length with increasing confining pressure is determined by a linear motion potentiometer with a precision of ∆DL=±0.024 mm. The potentiometer failed during later measurements. The maximum change in length measured for a sample was about 1.1 mm, Consequently, ∆DL of ±0.60 mm was assumed for samples without potentiometer data.

Table 2.3: Sample-lengths measurements and associated uncertainties (all lengths are given in mm)

Sample	Tool	ΔL'	L_1	L_2	L_3	L_4	L	ΔL*	ΔL
M1	MXCT	±0.05	19.32	-	-	-	19.32	±1.00	±1.05
M2	MXCT/ Caliper	±0.05	22.02	21.34	20.33	20.22	20.98	±0.86	±0.91
M3	MXCT	±0.05	19.79	15.94	-	-	19.69	±0.14	±0.19
M4	Caliper	±0.10	19.70	19.90	-	-	19.80	±0.14	±0.24
M5	Caliper	±0.10	19.46	19.66	-	-	19.56	±0.14	±0.24
M6	Ruler	±1.00	20.00	-	-	-	20.00	±1.00	±2.00
M7	Caliper	±0.10	19.40	19.50	-	-	19.45	±0.07	±0.17
M8	Ruler	±1.00	20.00	-	-	-	20.00	±1.00	±2.00
M9	Ruler	±1.00	20.20	-	-	-	20.20	±1.00	±2.00
M10	MXCT	±0.05	21.24	20.57	19.42	19.58	20.20	±0.86	±0.91
M11	MXCT	±0.05	18.09	18.36	19.04	19.01	18.62	±0.47	±0.52
M12	MXCT	±0.05	20.93	20.74	20.61	19.91	20.54	±0.44	±0.49
M13	Ruler	±1.00	20.00	-	-	-	19.50	±1.00	±2.00
M20	MXCT	±0.05	19.77	19.68	19.29	20.31	19.76	±0.42	±0.47
M21	MXCT	±0.05	20.48	20.11	20.56	20.71	20.27	±0.41	±0.46
M25	Caliper	±0.10	18.50	19.00	19.00	19.00	18.88	±0.25	±0.35

ΔL' represents the precision of the measurement tool. L_i (i=1…4) were measured at different angles around the cylindrical sample, ΔL* is the standard deviation [Taylor, 1982] calculated based on L_i. For specimen with only L_1, ΔL* was assumed to be 1 mm. ΔL' and ΔL* were added to obtain an overall error for length measurements (ΔL).

The traveltime of the ultrasonic pulse could be picked with a precision of $\Delta t = \pm 0.1$ µs. This uncertainty was based on the as on personal visual judgment with respect to identifying first arrivals of p- and s-waves. We chose to pick the first minimum of the p- and s-wave as first arrivals as these features were more clearly identifiable than the onset of the event. Note that choosing the wave onset instead of the first minimum can result in higher velocity values. The difference in velocities resulting from choosing different picking locations can vary between 50 and 200 m/s depending of the frequency of the recorded waveform.

As mentioned above, the transducer dead-time correction depended on temperature. The temperature inside the pressure vessel varied less than 2°C during the confining pressure test. Taking into account the R^2, the resulting differences in dead-time correction for p- and s-wave traveltimes were assumed to be $\Delta Dt_p = \pm 0.031$ µs and $\Delta Dt_s = \pm 0.098$ µs, respectively.

The resulting relative errors ranged between 2 and 11% for both, v_p and v_s. The main contributor to this uncertainty was the precision in length measurements. Lower uncertainties, in the range of 2-5%, were estimated for samples with lengths measured using the MXCT or caliper, tools with relatively high precision. The lowest errors were obtained for samples with transducer endplates aligned close to parallel. The highest uncertainties of about 11% were estimated for samples whose lengths were measured with a low-precision ruler or those samples that exhibited the highest degree of skewness. Of the 2-11% overall relative error, about 1% was attributed to the accuracy of calculating the traveltime of the pulse. Note that a relative error of 11% approaches the sample-based variability of velocities found for most sample types. Waite et al.

[2011] assumed that the errors associated with the velocity data are negligible compared to the sample- or methodology-based variability of the reported data. Our results suggest that uncertainties associated with individual data points are not negligible and should be reported.

2.5 Conclusions

Delineation of natural gas hydrate deposits from seismic sections or well-logs requires reliable knowledge of the petrophysical properties of the hydrate-bearing sediments and the surrounding formations. To assess the accuracy and repeatability of laboratory velocity measurements commonly used for the calibrating for geophysical field measurements, we performed repeat measurements of ultrasonic velocities in dry, partially water saturated, frozen, THF- and CH_4- hydrate-bearing sandpacks. At least three specimens for each sample type were prepared and tested over a range of effective pressures.

For dry and partially saturated sand, velocities fell within a ±100m/s range, and our results agreed well with literature data. As expected, v_p and v_s in partially water-saturated sand were slightly lower than those in dry sand due to a small increase in bulk density with 20% of the pore space being filled with water. Velocity differences between samples were mainly attributed to small variations in packing and porosity.

When the sample was frozen, the effect of variations in the sample make-up was amplified, due to the increased complexity of the measured system and the more significant impact of a cementing solid, rather than a liquid pore-fill. The stiffness of the sediment increased significantly as ice cemented the unconsolidated sediment grains

causing v_p and v_s to triple and double, respectively. The actual velocity increase depended on the ice saturation, distribution, and amount of unconverted water between ice and grains. Inconsistencies in these parameters in addition to variations in porosity and packing doubled the data spread to ±200 m/s.

Of all sample types, the CH_4 hydrate-bearing sandpacks exhibited the highest level of scatter in the velocity data. At P_d=435 psi (3MPa), v_p of 1570±102 m/s, 2519±134 m/s, and 2923±234 m/s were measured for the three specimens, respectively. The corresponding values recorded for v_s were 1095±68 m/s, 1736±83 m/s, and 2146±172 m/s. We attributed the high variability to inconsistent water distributions prior to hydrate formation, which affected the amount and distribution of the hydrate as well as of the residual, unconverted water. Variations in the initial water distribution were caused by differences in the sample history and by high, inconsistent gas injection rates that likely caused water redistribution in the sample (Figure 3.3 in Chapter 3 shows some redistribution of water after gas injection). To increase the repeatability of futures measurements, we would consequently recommend the use of "fresh" samples, i.e. partially water-saturated samples that have not been exposed to repeated loading, unloading, freezing and thawing cycles. CH_4 injection into the sample should be pump controlled and done at a constant, slow rate to minimize movement of water. For samples with an even distribution of CH_4 hydrate, we would expect velocities to be comparable to those of the frozen partially water-saturated samples.

For THF hydrate, the most reproducible results were achieved when the sample was vacuumed prior to injection of the THF-H_2O solution, and the pore pressure was kept constant with a pump at 100 psi allowing draining during compaction. Velocities

recorded for these samples fell within a ±150 m/s range. At the same effective stress, but lower pore pressure, higher velocities were recorded for drained THF hydrate-bearing sediment. In un-drained samples, hydrate formation and loading caused pore pressure to increase, thereby reducing the effective pressure as well as the measured velocities.

Sample preparation and measurement procedures produced relative uncertainties between 2 and 11% for individual velocity-data points. The uncertainty associated with the sample length was the main contributor. Generally, lower errors could be achieved through the use of more reliable methods for measuring the initial sample length and length changes during changes in confining pressure. In addition, controlling the parallel alignment of the transducer endplates is advisable.

CHAPTER 3

EFFECT OF THE INITIAL WATER SATURATION ON THE ELASTIC PROPERTIES OF HYDRATE-BEARING OTTAWA SAND F110

Chapter 3 is the first of a four-chapter investigation of the effects hydrate formation has on the elastic wave velocities through hydrate-bearing, unconsolidated coarse-grained sediments. Chapters 3, 4 and 5 present the experimental and modeling results. The key observations of each chapter are brought together in Chapter 6 to create a unified picture, over the full range of possible initial water saturations, of how hydrate formation occurs and subsequently controls the wave velocities through hydrate-bearing sands.

Ultrasonic velocities were measured in conjunction with magnetic resonance imaging (MRI) in hydrate-bearing Ottawa Sand F110 during hydrate formation and dissociation. P- and s-wave velocities were determined as functions of gas hydrate saturation. Hydrate-formation techniques included the use of tetrahydrofuran (THF) and CH_4 injection into partially water-saturated samples. For the latter, samples with low and high **i**nitial water saturation (S_{wi}) were tested. The recorded velocities exhibited a noticeable dependence on S_{wi}. At low S_{wi} (about 20%), hydrate increased the ultrasonic velocities exponentially during hydrate formation. However, the overall rate of the velocity increase was reduced with increasing S_{wi}. At high initial water saturations (about 80%), the velocities increased linearly with increasing hydrate content. Ultrasonic velocities recorded in THF hydrate-bearing sediment during dissociation decreased

steadily with decreasing hydrate saturation. Below a hydrate saturation of 30-40%, velocities changed very little. Similar velocity trends were reported for sediment samples with varying THF hydrate saturations [Yun et al., 2005; Lee et al., 2010], as well as in glass bead packs subjected to CH_4 hydrate formation out of solution [Spangenberg et al., 2008].

3.1 Introduction

Natural methane (CH_4) hydrates are found worldwide in a variety of geological settings, such as oceanic sediments of outer continental margins, polar sediments on continents and continental shelves, and in deep-water sediments of inland lakes and seas [Kvenvolden & Lorenson, 2001; Collet et al., 2009]. Formation and distribution of natural CH_4 hydrate in natural sediment are controlled by a number of factors, such as pressure-temperature conditions, lithology, pore-water chemistry, CH_4 availability, as well as the mode of transport of CH_4 into the gas hydrate stability zone [Tréhu et al. 2006b]. CH_4 can migrate into the hydrate stability zone either by diffusion or advection [Paull et al., 1994]. Diffusion is a very slow process and would not likely form substantial gas hydrate accumulations over reasonable geologic timescales [Xu and Ruppel, 1999]. CH_4 migration by advection on the other hand is a very efficient process and can occur either with CH_4 as a free gas phase (bubble) or with CH_4 dissolved in upward moving water [Hyndman and Davis, 1992].

Which process dominates in the formation of natural gas hydrate systems depends on the geological settings of the hydrate “petroleum system” [Collett et al., 2009]. Gas hydrate deposits found in the Arctic (e.g. Prudhoe Bay) are believed to have

formed from a pre-existing conventional gas reservoir that cooled when the area was glaciated in the Pleistocene [Collett et al., 2009; Dai et al., 2011]. At Blake Ridge, low-saturation gas hydrates (<10% of the pore space) formed in fine-grained sediments from in-place biogenic gas [Paull et al., 1994]. At the Cascadia Margin, gas hydrate is assumed to have formed from gas-saturated water moving upward into fine-grained sediments inside the gas hydrate stability zone [Hyndman and Davis, 1996]. Both marine areas are characterized by high saturations at the bottom of the gas hydrate stability zone (GHSZ) and lower saturations within. In marine areas such as Alaminos Canyon in the Gulf of Mexico, Nankai Trough offshore Japan, or the Shenhu area in the South China Sea, coarse-grained sediment formations provide permeable conduits for the transport of gas either in solution or in form of bubbles [Hutchinson et al., 2008; Collett et al., 2009; Fuji et al., 2009; Wang et al., 2011]. The resulting gas hydrate-bearing zones have recently been targeted as potential energy resources due to their high intrinsic permeability and hydrate content.

The manner in which CH_4 hydrate forms influences the hydrate habit and distribution, both of which in turn impact the bulk physical properties, such as seismic velocities. Priest et al. [2009] observed this experimentally, showing that wave velocities increase dramatically in water-limited specimens as methane hydrate cements sediment grains. In contrast, wave velocities are much less sensitive to methane hydrate formation in gas-limited specimens, where hydrate forms away from the grain contacts and no cementation occurs [Priest et al., 2009]. This work by Priest et al. [2009] presents wave velocity results for specimens over a range of hydrate saturations only after the specimens reach their peak hydrate saturation, and Hu et al.

[2010] note this is true of most previous studies. In this study, we measure, visualize, and model how velocities change as hydrate saturation changes during the formation and dissociation processes. Establishing these relationships is critical for predicting how the reservoir properties near a production well change during hydrate dissociation and, potentially, during secondary hydrate formation while extracting methane from hydrate-rich sands as an energy resource.

In this chapter, we report ultrasonic velocities recorded during the formation of CH_4 and tetrahydrofuran (THF) hydrate in unconsolidated sandpacks. CH_4 hydrates were formed by injecting a free gas phase into partially water-saturated sand samples over a range of initial water saturations. THF, on the other hand, is completely miscible in water and thus forms hydrate out of solution [Lee et al., 2007]. The resulting CH_4 and THF hydrate-bearing samples are believed to represent end-members regarding their mechanical properties. Previous laboratory studies have shown that CH_4 hydrate formed from a free, continuous gas phase causes significant stiffening of the sediment [Waite et al., 2004, Priest et al., 2005], whereas hydrates formed out of solution generally do not seem to interact with the sediment until 40% of the pore space is saturated [Yun et al. 2005; Spangenberg et al., 2008; Lee et al., 2010]. Similar to hydrate formed out of solution, hydrate formed from a limited amount of free gas and a continuous water phase does not appear to affect the sediment stiffness [Priest et al., 2009].

Establishing relationships between hydrate content and velocities throughout the course of an experiment requires a reliable method of hydrate quantification that can be employed throughout the experiment. Previously, hydrate saturations have been

calculated based on the amount of CH_4 released during dissociation [Waite et al., 2004], as well as from the amount of water or CH_4 provided for hydrate formation [Priest et al., 2005; 2009]. Using THF, the hydrate saturation was determined by the composition of the THF-water solution [Yun et al., 2005; Lee et al., 2010]. Unfortunately, these methods only allow calculation of bulk hydrate saturations of the final product. Spangenberg et al. [2008], however, determined the hydrate saturation throughout the hydrate formation process by measuring the increase in pore-fluid conductivity as salt ions were excluded during hydrate formation. Ebinuma et al. [2008] calculated the hydrate content based on the CH_4 consumed by hydrate formation. Hu et al. [2010] employed time-domain reflectometry, a dielectric technique, to determine changes in hydrate content during formation.

In this study, magnetic resonance imaging (MRI) was used to determine hydrate saturations simultaneously with the ultrasonic velocity measurements. MRI measurements were first employed to monitor gas hydrate formation by Moudrakovski et al. [2002] and has since proved to be a valuable tool to determine the gas hydrate saturation and distribution within porous media [e.g. Baldwin et al., 2003; Gao et al., 2005; Ersland et al., 2010]. MRI detects hydrogen in the free water phase but not when it occurs in solid phases such as gas hydrate. The signal strength is assumed to decrease linearly with the amount of liquid water converted.

3.2 Experimental Setup and Procedure

This section describes the experimental equipment used to measure ultrasonic velocities during hydrate formation and dissociation in unconsolidated sandpacks. In addition, preparation of the THF and CH_4 hydrate-bearing samples is detailed.

3.2.1 Experimental Equipment

The experimental setup (Figure 3.1) consisted of a temperature-controlled pressure vessel filled with Flourinert™ which surrounded an instrumented sample holder. Flourinert™ is a fluorocarbon that contains no hydrogen and is, thus, invisible to the MRI. The pressure vessel was especially designed for use inside an MRI and consisted of a low-inductance fiberglass cylinder with titanium end pieces, which had multiple ports for fluid flow and temperature sensors. The Fluorinert™ was chilled with a temperature bath and circulated through the pressure vessel to cool the jacketed sample. The Fluorinert™ flow rate and the confining pressure it exerted on the specimen were regulated by a computer-controlled high-pressure Quizix™ pump. The sand sample itself was jacketed with heat shrink tubing and sandwiched between a pair of 2-inch diameter PEEK end caps that contained 500 kHz piezoelectric p- and s-wave crystals. The respective wave speeds were determined using the pulse-transmission technique. The use of PEEK provided improved impedance matching between transducer and sample and also shielded the transducers from the magnetic field of the MRI. Additionally, the end caps contained ports to enable fluid circulation through the sample. A second Quizix™ pump delivered the methane and provided the pore pressure necessary for hydrate formation and stability. The temperature of the confining

fluid (outside the sample), the confining and pore pressure, and the ultrasonic waveforms (Figure 3.2) were recorded throughout the experiment. In addition, two types of MRI scans were acquired: MRI profiles that illustrate the hydrogen distribution along the sample axis (Figure 3.3) and 3-dimensional images that depict the hydrogen distribution throughout the sample (Figure 3.4). Acquisition of 3D images took 2 hours whereas the acquisition of MRI profiles required less than a minute. MRI profiles were also utilized to determine the length of each sample with an accuracy of ±1 mm. More detailed information on experimental setup components and specifics about the MRI-data acquisition can be found in Ersland et al. [2010].

3.2.2 Sample Preparation

We investigated the dissociation of THF hydrate as well as the formation of CH_4 hydrate-bearing Ottawa sand. In the following, we describe preparation of the unconsolidated sandpacks, as well as the hydrate formation procedures employed in the experiments.

3.2.2.1 THF Hydrate-Bearing Sample

THF crystallizes as structure-II hydrate. The polar compound is completely miscible in water, thus forms hydrate out of solution and promises homogeneous synthesis of THF hydrate in sediment [Lee et al. 2007]. The ratio of THF and water in the solution determines the amount of hydrate formed in the pore space [Yun et al., 2005] as well as its equilibrium temperature. The solution used in this study contained 15 wt% THF and 85 wt% water, which yielded a hydrate saturation of about 80%. The equilibrium temperature of the resulting THF hydrate is about 3.8°C at atmospheric

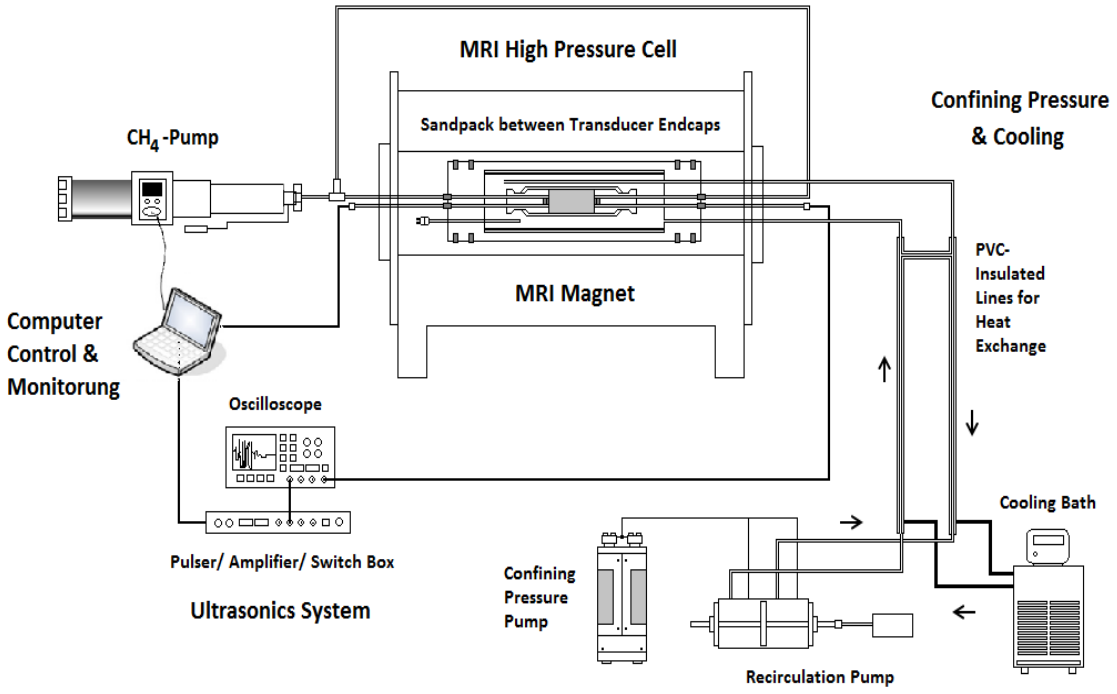

Figure 3.1: Experimental Setup (not drawn to scale, modified from Ersland et al. 2010)

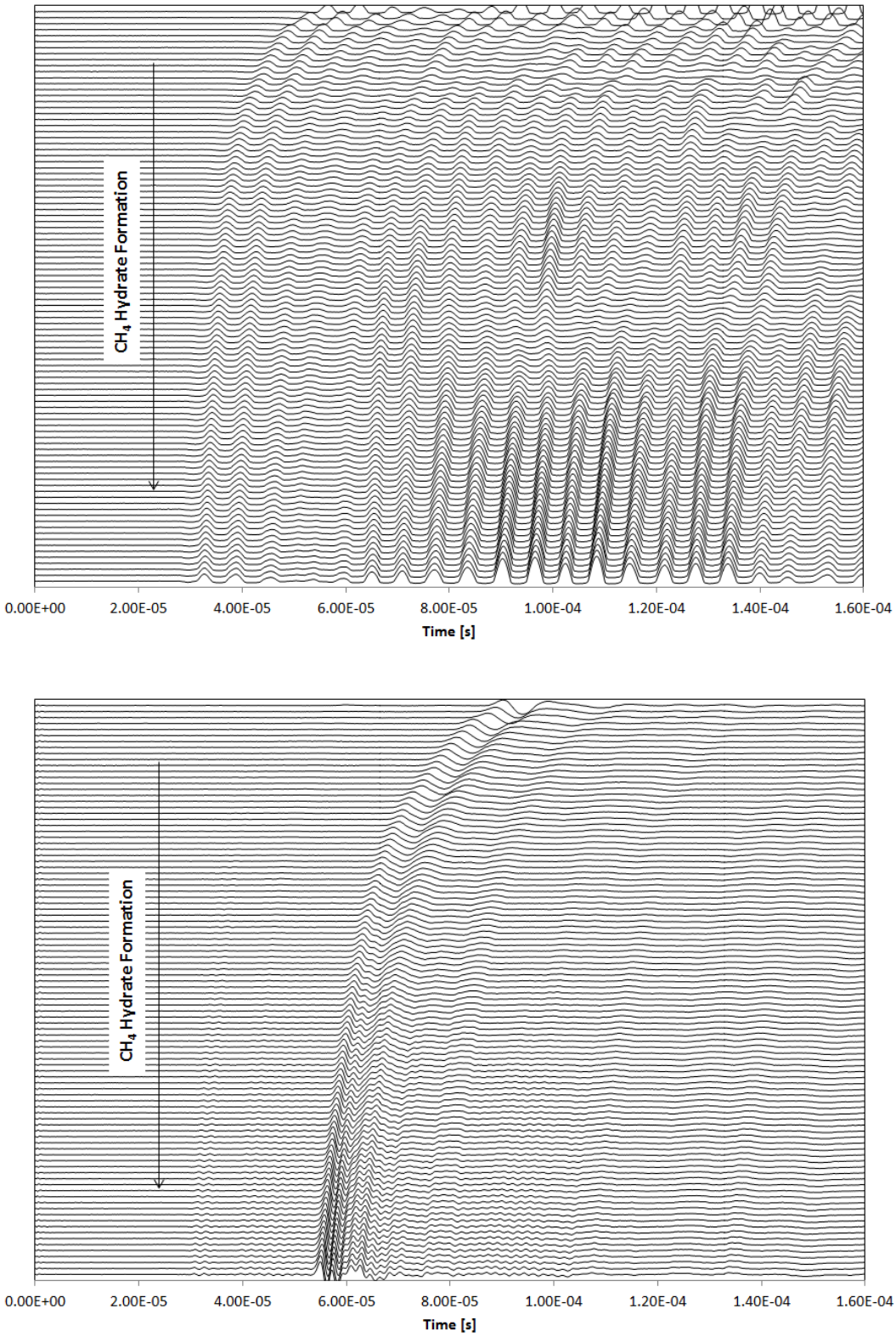

Figure 3.2: Ultrasonic waveforms recorded for p-waves (top) and s-waves (bottom) during CH_4 hydrate formation (Experiment 5, Formation F2)

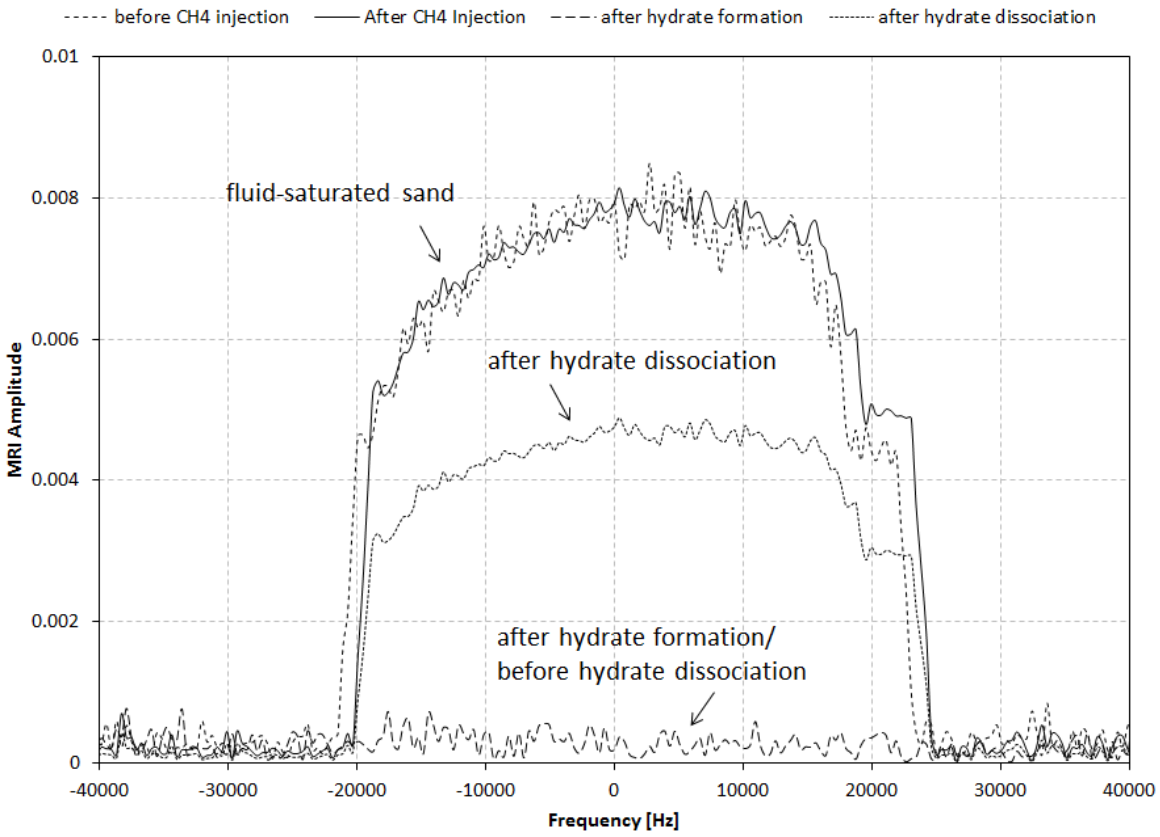

Figure 3.3 MRI profiles collected at different stages of the experiment (Experiment 5)

pressure [Gough and Davidson, 1971; Dyadin et al., 1973; see also Chapter 4]. The THF hydrate-bearing specimen was prepared with Ottawa sand F110, nearly pure quartz sand with a 50 to 400-μm grain size range. Dry sand was poured into a "mold" made up by pre-shrunk heat-shrink tubing and one transducer endplate. The specimen was tamped prior to affixing the second endplate. The sandpack was compacted until it reached a pre-determined volume (about 50 cm^3) that resulted in an average porosity of about 40%. Afterwards, the sandpack was placed inside the pressure vessel, vacuumed, and injected with the THF-H_2O solution. The saturated sample was subjected to a confining pressure of 340±27 psi (2.34±0.19 MPa) and cooled down to about 1.5°C inside a large-volume freezer. Ultrasonic waveforms were recorded sporadically every few hours (Table 3.2). A noticeable increase in both p- and s-wave velocity (v_p, v_s) indicated that THF hydrate had formed. The THF hydrate-bearing sample remained inside the freezer for three additional days to ensure complete hydrate conversion before being transferred to the MRI where the temperature of the confining fluid was raised in increments of about 1°C every two hours. Ultrasonic velocities and 3D (2-hour) MRI images were recorded at every temperature step (Figures 3.4 and 3.5).

3.2.2.2 CH_4 Hydrate-bearing Samples

Unlike THF hydrate, CH_4 hydrate is a structure-I hydrate, and was formed from two separate phases. CH_4 was injected as a continuous gas phase into partially water saturated sandpacks. Thus, the hydrate formation was limited by the amount of pore water present in the sample. For the CH_4 hydrate-formation experiments, four partially water-saturated sandpacks were prepared, two of each with "low" and "high" initial water

saturation (S_{wi}), respectively (Table 3.1). For each sample, dry sand and de-ionized water were mixed thoroughly in a plastic bag and then compacted into the sample mold. The resulting wet sandpacks contained 20% water in the pore space. To achieve higher saturations of about 80%, additional de-ionized water was injected after the sample was placed in the pressure vessel and positioned inside the MRI. The MRI profiles quantified the water distribution through the sample (Figure 3.3). The saturated samples were first subjected to an initial confining pressure of above 1600 psi (11.034 MPa) and afterwards injected with CH_4. Hydrate formation was achieved one of two ways: 1) The pore pressure (P_p) was raised to 1200 psi (8.276 MPa) and the pressurized samples were cooled into the hydrate stability region ("Formation 1" in Figure 3.6). After most of the water had converted into CH_4 hydrate, the sample's pore space was depressurized (while maintaining the confining pressure) causing the CH_4 hydrate to dissociate; 2) Post dissociation, two of the samples were re-pressurized into the CH_4-hydrate stability region to re-form hydrate ("Formation 2" in Figure 3.6).

Table 3.1: Properties of sandpack samples
(error of length measurement: ±0.01 cm, weight: ±0.001 g)

Sample	Guest	Length [cm]	Sand mass [g]	Water mass [g]	Porosity	S_{wi}
Experiment 1_D	THF	4.10	132.500	-	0.400	1.000
Experiment 2_F1	CH_4	4.17	132.520	27.000	0.408	0.782
Experiment 2_F2	CH_4	4.17	132.520	5.093	0.408	0.146
Experiment 3_F1	CH_4	4.15	132.504	7.009	0.406	0.205
Experiment 4_F1	CH_4	4.12	132.505	27.056	0.401	0.808
Experiment 5_F1	CH_4	4.35	132.510	7.010	0.394	0.216
Experiment 5_F2	CH_4	4.35	132.510	6.135	0.394	0.189

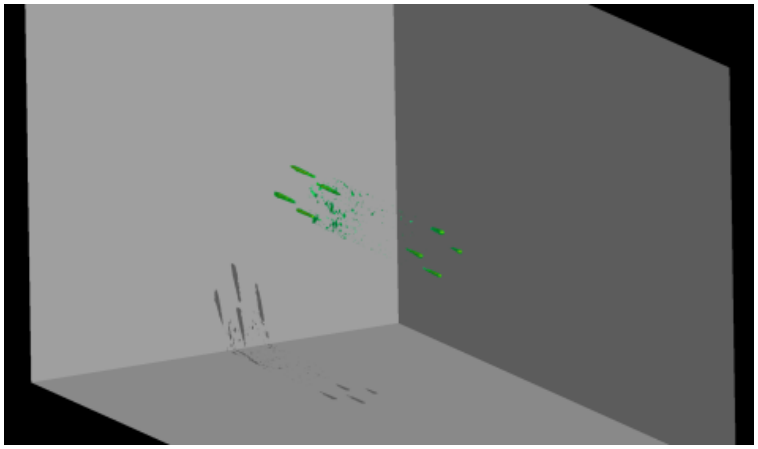

Figure 3.4a: 3D MRI images recorded during THF hydrate dissociation (8 hours, T=4.0°C)

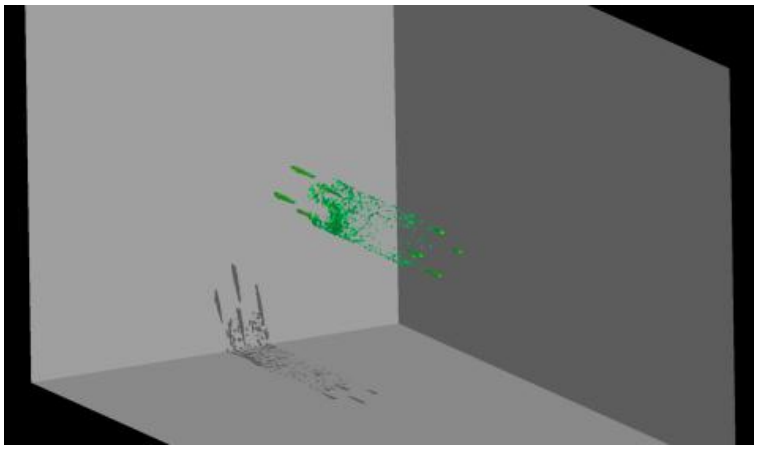

Figure 3.4b: 3D MRI images recoded during THF hydrate dissociation (9.5 hours, T=4.5°C)

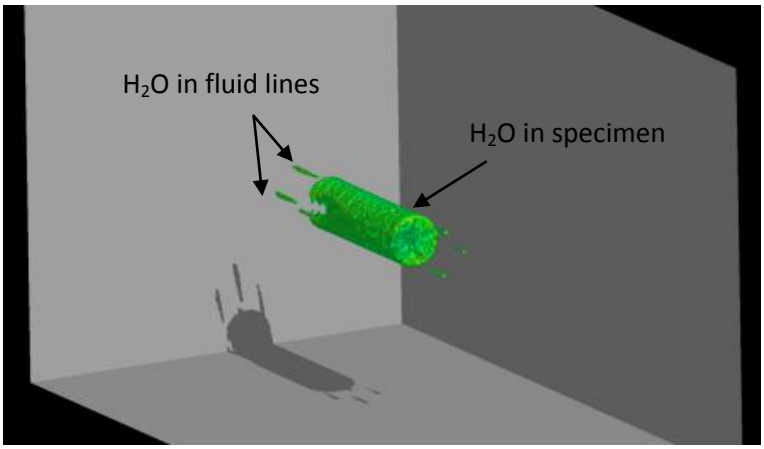

Figure 3.4c: 3D MRI images recoded during THF hydrate dissociation (11.5 hours, T=5.0°C)

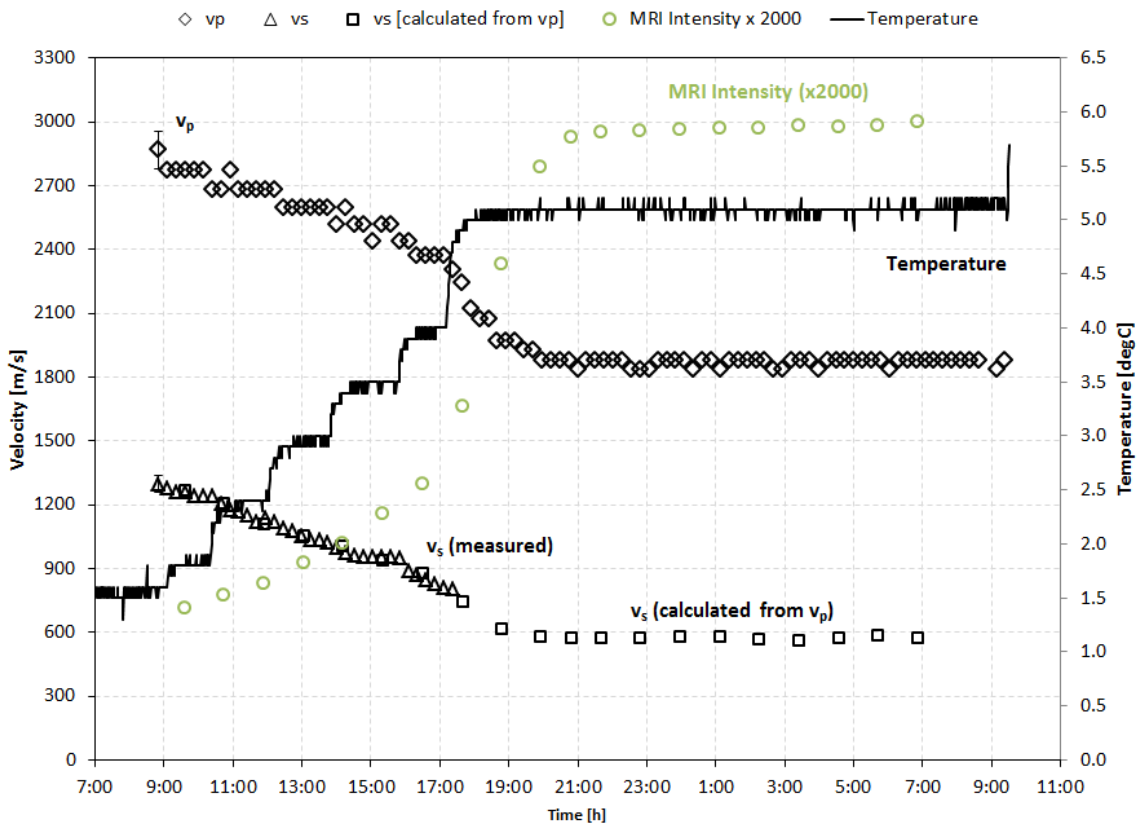

Figure 3.5: Temperatures, ultrasonic velocities, and MRI intensities recorded during THF-hydrate dissociation in Ottawa Sand. Experiment 1 was conducted without applying any pore pressure. However, in this un-drained sample, application of 337 psi (2.324 MPa) confining pressure may have increased the pore pressure.

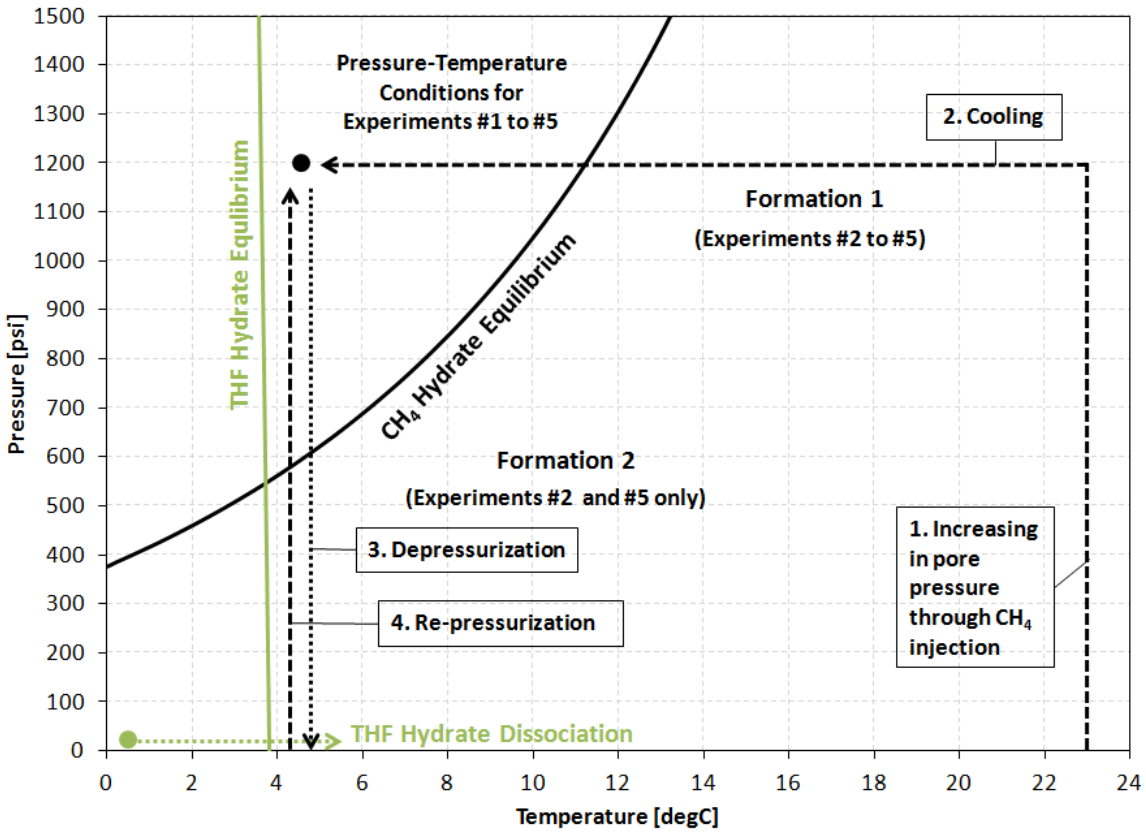

Figure 3.6: Pressure-temperature paths for THF hydrate dissociation as well as CH_4 hydrate Formation 1 (pressurization before cooling) and Formation 2 (cooling before pressurization). The phase-equilibrium curve for CH_4 hydrate was calculated with CSMGem [Sloan and Koh, 2008]. THF hydrate equilibrium data calculated after Gough and Davidson [1971]

3.3 Results

Below, results of these tests are summarized, starting with Experiment 1 (THF-hydrate dissociation), followed by Experiments 2-5 (CH_4-hydrate formation), concluding with an overview of error calculation and analysis. Pressure and temperature profiles as well as detailed velocity and MRI-intensity data recorded are presented.

3.3.1 THF Hydrate Dissociation (Experiment 1)

The first test was conducted on the THF hydrate-bearing sandpack (Experiment 1). Prior to the injection of the THF-water solution, ultrasonic velocities were measured for the dry sandpack under varying confining pressure. The results for v_p and v_s are listed in Table 3.2. Also given are the velocities measured on the fully saturated sample inside the refrigerator before and after hydrate formation. The values obtained for dry and saturated sandpacks agree well with results of other studies [e.g. Waite et al., 2011]. To initiate hydrate formation, the sample was subjected to a temperature of 1.5±0.1°C and a confining pressure of P_c= 337±27 psi (2.324 MPa). Assuming all THF had converted into hydrate, 80% of the pore space should have been filled with hydrate. While the specimen was stored inside the refrigerator, noticeable variations in v_p and v_s were observed that corresponded to changes in temperature (Table 3.2). Once the sample was placed inside the MRI, v_p and v_s for the THF hydrate-bearing sandpack were recorded as 2867±36 m/s and 1340±12 m/s, respectively, at T=1.6°C prior to hydrate dissociation (Figure 3.5).

Figures 3.4a-c show the 3D MRi images acquired before, after, and during THF hydrate dissociation. Note that in Figure 3.4, residual water can be seen concentrated in the back of the THF hydrate-bearing sample, while in the rest of the specimen all water

Table 3.2: Ultrasonic velocities measured for Ottawa sand F110 (THF Hydrate, Experiment #1)

Date/Time	T [degC]	P_c [psi]	Comment	V_p [m/s]	V_s [m/s]	v_p/v_s
04/23/2010 12:00	Room	500	Dry	886±19	579±13	1.53
04/23/2010 12:00	Room	450	Dry	878±19	571±13	1.53
04/23/2010 12:00	Room	400	Dry	860±19	553±13	1.55
04/23/2010 12:00	Room	350	Dry	817±18	528±12	1.55
04/28/2010 11:00	9.2	350	Saturated	2030±36	522±12	3.89
04/28/2010 14:54	4.9	350	Saturated	2050±37	528±12	3.89
04/28/2010 16:02	5.3	350	Saturated	2030±36	522±12	3.89
04/29/2010 08:25	2.3	350	Hydrate-Bearing	3000±43	1340±27	2.24
04/29/2010 10:50	1.8	350	Hydrate-Bearing	3154±45	1385±28	2.28
04/29/2010 13:30	2.4	350	Hydrate-Bearing	2929±44	1168±24	2.51
04/29/2010 16:33	3.3	350	Hydrate-Bearing	2867±44	1085±23	2.64
04/30/2010 08:24	3.8	350	Hydrate-Bearing	2971±44	1012±21	2.94
04/30/2010 10:20	2.4	350	Hydrate-Bearing	3178±45	1349±27	2.36
04/30/2010 11:20	1.3	350	Hydrate-Bearing	3280±46	1519±30	2.16
04/30/2010 13:30	1.1	350	Hydrate-Bearing	3388±46	1577±31	2.15
04/30/2010 15:10	1.5	350	Hydrate-Bearing	3417±46	1571±31	2.18
04/30/2010 16:33	1.2	350	Hydrate-Bearing	3306±46	1444±29	2.29
05/03/2010 07:56	2.9	350	Hydrate-Bearing	2828±44	1136±24	2.49

appears to have been incorporated in the hydrate. The distribution of THF hydrate is less homogeneous than expected. Figure 3.5 shows temperatures, MRI intensities and velocities recorded during warming of the THF hydrate-bearing specimen. In the first 8 hours, between 1.5°C and 4.0°C, the velocity decreased linearly with the temperature. This was a surprising observation, as the sample temperature had not yet reached the expected dissociation temperature of THF hydrate. However, the corresponding MRI-intensity increase suggested that hydrate decomposed. After the temperature inside the pressure vessel approached 5°C, the rate of hydrate dissociation increased, as indicated by a rapid increase in MRI intensity and a sharp drop in both v_p and v_s. Four hours later, THF hydrate dissociation ceased, and both the velocities and MRI intensity stabilized. In the waveforms acquired after hydrate had dissociated, the s-wave arrival occurred outside the recorded time range. Consequently, v_s was obtained by extrapolating the v_p/v_s-ratio as a function of temperature.

Note, that dissociation below the nominal equilibrium temperature of THF hydrate has previously been observed in differential scanning calorimetry measurements [see Chapter 5, Figure 5.2] as well as in thermal property measurements performed by Waite et al. [2005]. In addition, v_p and v_s recorded on the THF hydrate-bearing specimen while stored in the freezer (Table 3.2) exhibited a notable sensitivity to oscillating freezer temperatures. All these observations suggest the THF-hydrate saturation was not only a function of the initial fluid composition but also of temperature. This true in methane hydrate as well: Zatsepina and Buffett [1997] showed that, in the presence of CH_4 hydrates, the solubility of CH_4 in water decreased sharply with decreasing temperature. In other words, when hydrate is present and the temperature of the surrounding pore

water increases, the solubility of the hydrate former increases as well. Part of the gas hydrate will have to decompose to provide the CH_4 required to generate the increased equilibrium CH_4 concentration. Since the solubility of CH_4 is relatively low to begin with ($<0.05 \cdot 10^{-3}$ mole fraction, [e.g. Handa, 1990]), only a relatively small amount of hydrate is generally dissolved in laboratory settings where water volumes are limited. This temperature-dependent dissolution process can consume seafloor gas hydrate outcrops in natural systems, however [Lapham et al., 2010]. We expect the hydrate dissolution effects of a temperature-dependent solubility to be more pronounced for THF, which is completely soluble in water in the absence of hydrate [Lee et al. 2007]. We believe the finite, temperature-dependent THF concentration in the excess water following hydrate formation caused the partial decomposition (dissolution) of THF hydrate at temperatures below the hydrate equilibrium.

Figure 3.4a shows a 3D MRI image of the THF hydrate-bearing sample prior to dissociation. As can be seen in the image, Figure 3.7 shows v_p and v_s recorded during the dissociation of THF hydrate as a function of S_h. The velocities decreased steadily as THF hydrate composed and S_h was reduced. When S_h fell below 30-40% the rate of velocity reduction with decreasing S_h declined. These observations correspond to published results of previous studies on hydrates formed out of solution.

Figure 3.8 shows v_p-S_h trends obtained in this study in comparison with those reported by Yun et al. [2005], Pohl [2012], and Spangenberg et al. [2008]. Yun et al. [2005] reported v_p and v_s for a number of THF hydrate-bearing Ottawa sand samples with different hydrate saturations. Spangenberg et al. [2008] measured v_p and v_s during CH_4 hydrate formation from the dissolved gas phase in a glass bead pack. In both

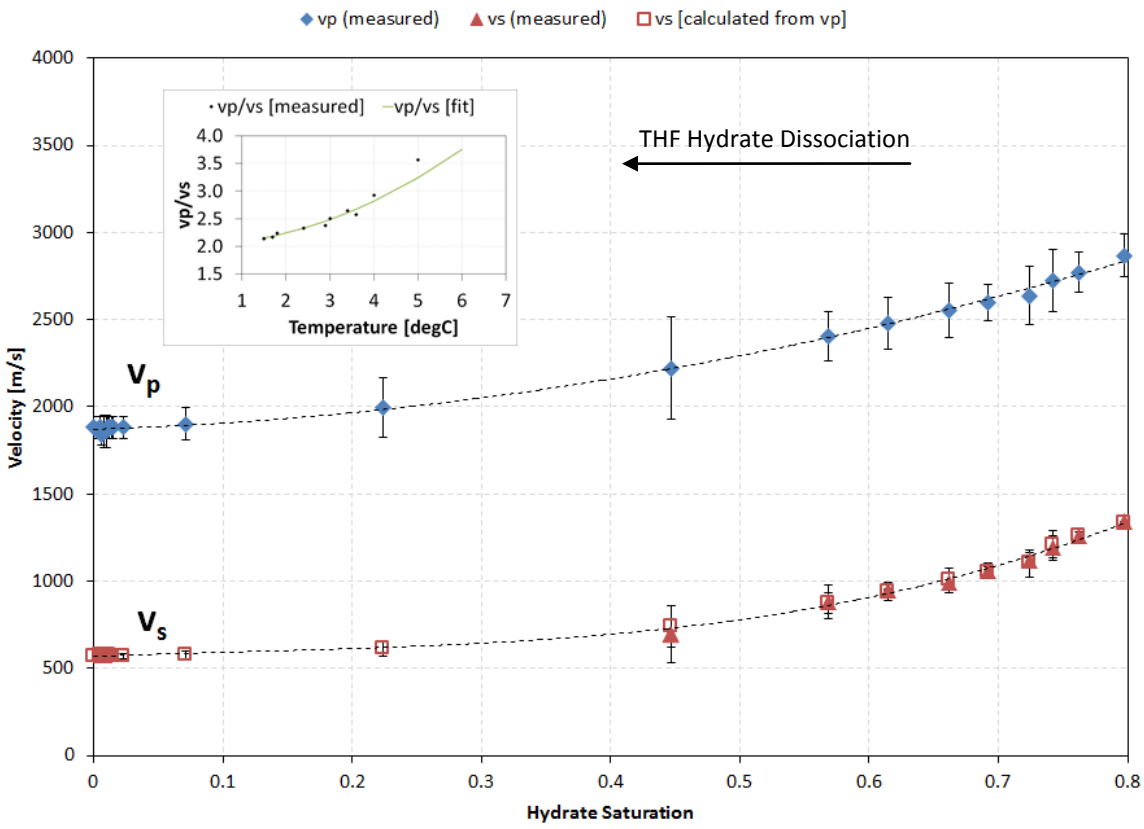

Figure 3.7: v_p and v_s as functions of hydrate saturation recorded during THF hydrate dissociation in Ottawa sand (Error bars for hydrate saturation have been omitted for clarity. The hydrate saturation uncertainty is the difference between neighboring data points).

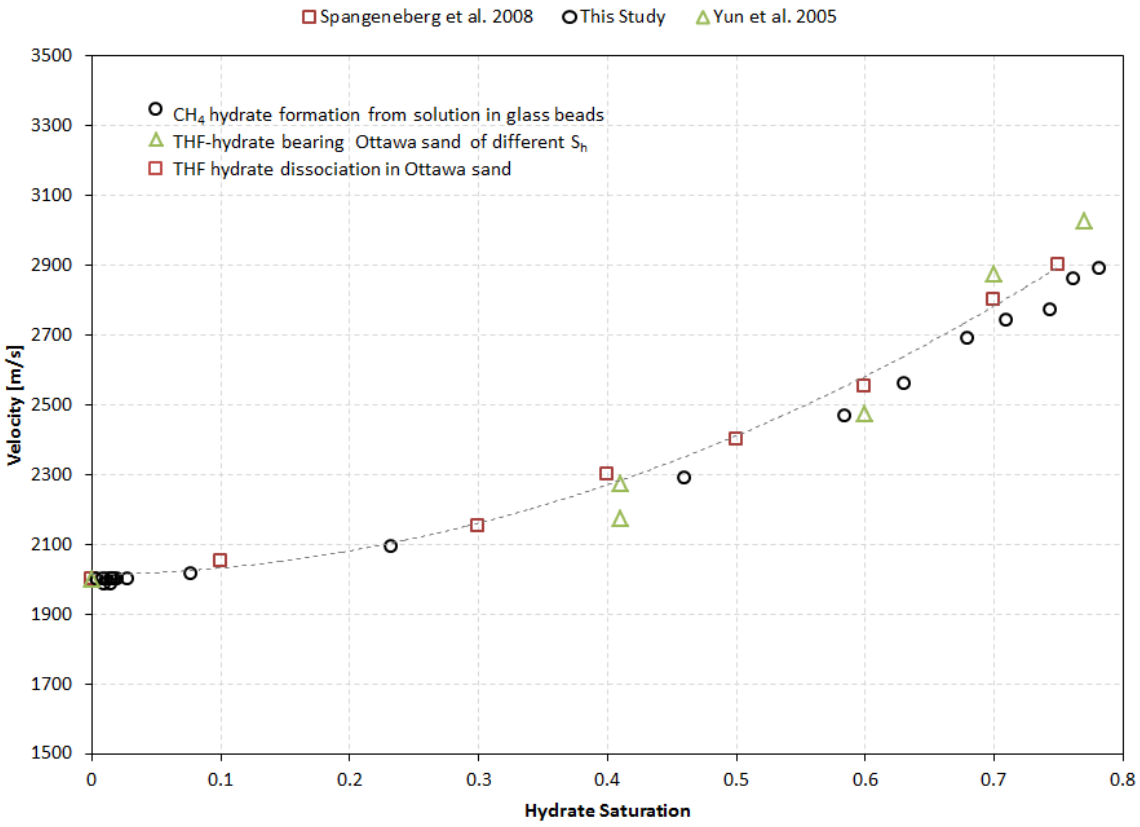

Figure 3.8: v_p as function of hydrate saturation recorded during THF hydrate dissociation (black circles) in comparison with velocity data recorded for THF hydrate-bearing samples of different S_h (green triangles) and velocity data recorded during CH_4 hydrate formation out of solution (red squares). Note that the velocities shown are shifted according to the effective stress differences so they have equal velocities at S_h=0.

studies, velocities were not significantly affected by the presence of THF or CH_4 hydrates unless the amount of hydrate present in the pore space exceeded 40%. Note that the data sets of the different studies were recorded at dissimilar confining pressures and sample make-up (porosity, porous medium). To facilitate the comparison of velocity change with hydrate saturation, the velocities shown in Figure 3.8 were shifted so v_p for S_h=0 were equal for all data sets. As can be seen, the same v_p-S_h trend can be observed irrespective of whether the velocities were measured during hydrate formation [Spangenberg et al., 2008], dissociation (this study), or in separate hydrate-bearing sediment samples with different hydrate saturations [Yun et al., 2005; Lee et al., 2010]. The manner in which THF hydrate forms and dissociates in sediment appeared to be reversible.

Note also that while formation and dissolution of CH_4 hydrate are likely to be reversible with respect to wave velocity, CH_4 hydrate formation and dissociation will not be. As the solubility of CH_4 in water is relatively low, and water in contact with methane hydrate must already be at the solubility limit for CH_4, more gas is stored in hydrates than could be taken up by the pore water during hydrate dissociation. Instead of ending up with a single phase of CH_4 saturated pore water, a free gas phase will develop. The presence of free gas would drastically reduce the bulk modulus of the sediment causing v_p to drop and hysteresis to occur in the measured velocity-saturation relationship.

3.3.2 CH_4 Hydrate Formation

Table 3.3 lists v_p and v_s measured for the partially water-saturated sandpacks prior to CH_4-hydrate formation. The velocities measured for specimens with low water

Table 3.3: Ultrasonic velocities for Ottawa Sand F110 prior to CH_4 Hydrate formation

Test	P_d [psi]	v_p [m/s]	v_s [m/s]	v_p/v_s
Experiment 2_F1	364.8±31.2	644±18	388±10	1.66
Experiment 2_F1	512.0±31.4	790±24	432±11	1.82
Experiment 2_F1	642.6±31.2	1048±36	471±12	2.22
Experiment 2_F2*	1446.5±52.9	1072±29	673±19	1.59
Experiment 3_F1	297.6± 0.7	790± 23	515±12	1.53
Experiment 4_F1	371.2±26.7	798±20	518±13	1.54
Experiment 4_F1	450.8±29.3	1731±44	575±14	3.01
Experiment 5_F1	312.9±19.9	749±17	502±12	1.49
Experiment 5_F2*	1574.3±30.2	1148±27	757±17	1.51

* Samples in Experiment 2 and 5 were re-pressurized after dissociation

saturation agree well with results from previous studies [Waite et al., 2011]. Initial velocities measured for low-S_{wi} samples prior to Formation 1 were lower compared to those recorded prior to Formation 2 because of the difference in effective pressure, (P_d). Velocities recorded for specimens with high S_{wi} were slightly lower compared to those of low-saturation samples. This was due to the increase in overall density (the square of the velocity is inversely proportional to density). The bulk stiffness, and hence the wave velocity, in partially-saturated sand does not increase significantly until the sample comes close to full saturation [Domenico, 1977]. This was seen in Experiment 4. As the confining pressure increased, the pore space was compressed due to a combination of gas being pushed out of the sample and gas bubbles being compressed, As a result, the water saturation increased and v_p jumped from 798±20 to 1731±44 m/s. The latter velocity was typically measured in fully water-saturated sand [Waite et al., 2011]

3.3.2.1 Experiment 2

Experiment 2 focused on CH_4 hydrate formation in a sandpack with high S_{wi} (=78.2%). The sample was pressurized to P_p=1200±8 psi (8.276 MPa) and cooled to 5±0.5°C (Figure 3.9). As the thermobaric conditions entered the CH_4 hydrate-stability region, the MRI intensity began to decrease, indicating that water was consumed by hydrate formation. The reduction in MRI intensity was accompanied by an increase in v_p and v_s. After 48 hours, the rate of velocity increase and MRI-intensity decrease slowed. At that time, the MRI intensity had been reduced to 21.7% of its original value. v_p and v_s had reached 2728±296 m/s and 1260±76 m/s, respectively, at P_d= 454±27 psi (3.131 MPa). Hydrate formation continued, but at a slower rate than before. After an additional 7 days, the MRI intensity had been reduced to 6.5% of its original value and both velocities stabilized at v_p=2818±235 m/s and v_s=1484±107 m/s at P_d= 417±27 psi (2.876 MPa).

To dissociate the hydrate, P_p was then dropped to 198.2±0.2 psi (1.368 MPa). The resulting gas expansion drove part of the water out of the sample, lowering the water-saturation to S_{wi}=14.6%. At a temperature of 5.0±0.1 °C, the pore-pressure was then increased back to 1200±44 psi (8.276 MPa) and CH_4 hydrate re-formed (Figure 3.10). Within two days the MRI intensity dropped to zero indicating that all water had been converted into CH_4 hydrate. At this point, v_p=3658±183 m/s and v_s=2080±79 m/s were recorded at P_d of 454±40 psi (3.131 MPa). Even though MRI intensities had reached zero indicating that no more CH_4 hydrate was formed, velocities continued to increase. This was attributed to annealing or aging of the hydrate crystals [Kuhs et al.,

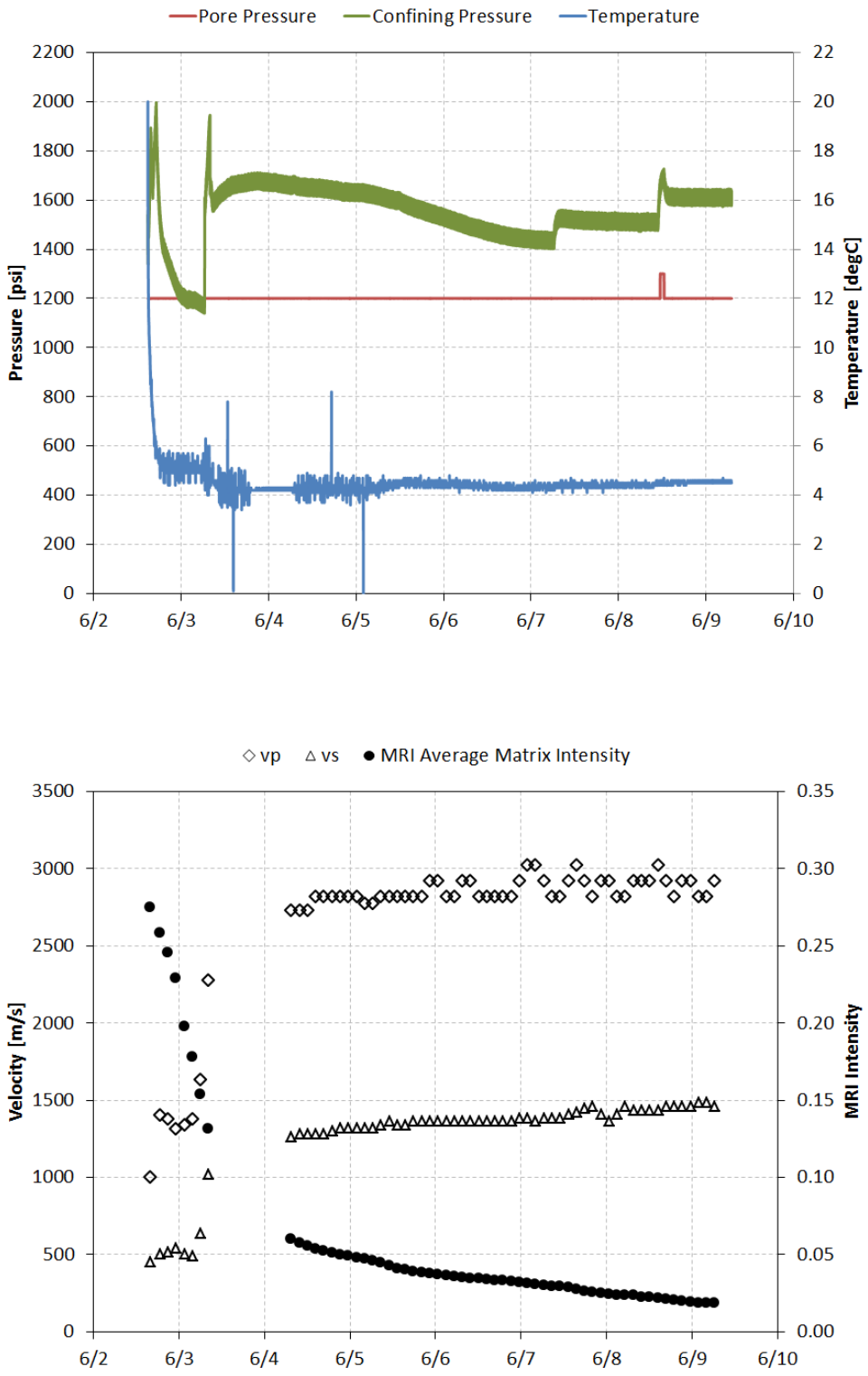

Figure 3.9: Experiment 2 (Formation 1) – CH_4 Hydrate Formation in partially water-saturated Ottawa Sand F110 high initial water saturation (S_{wi}=0.782)

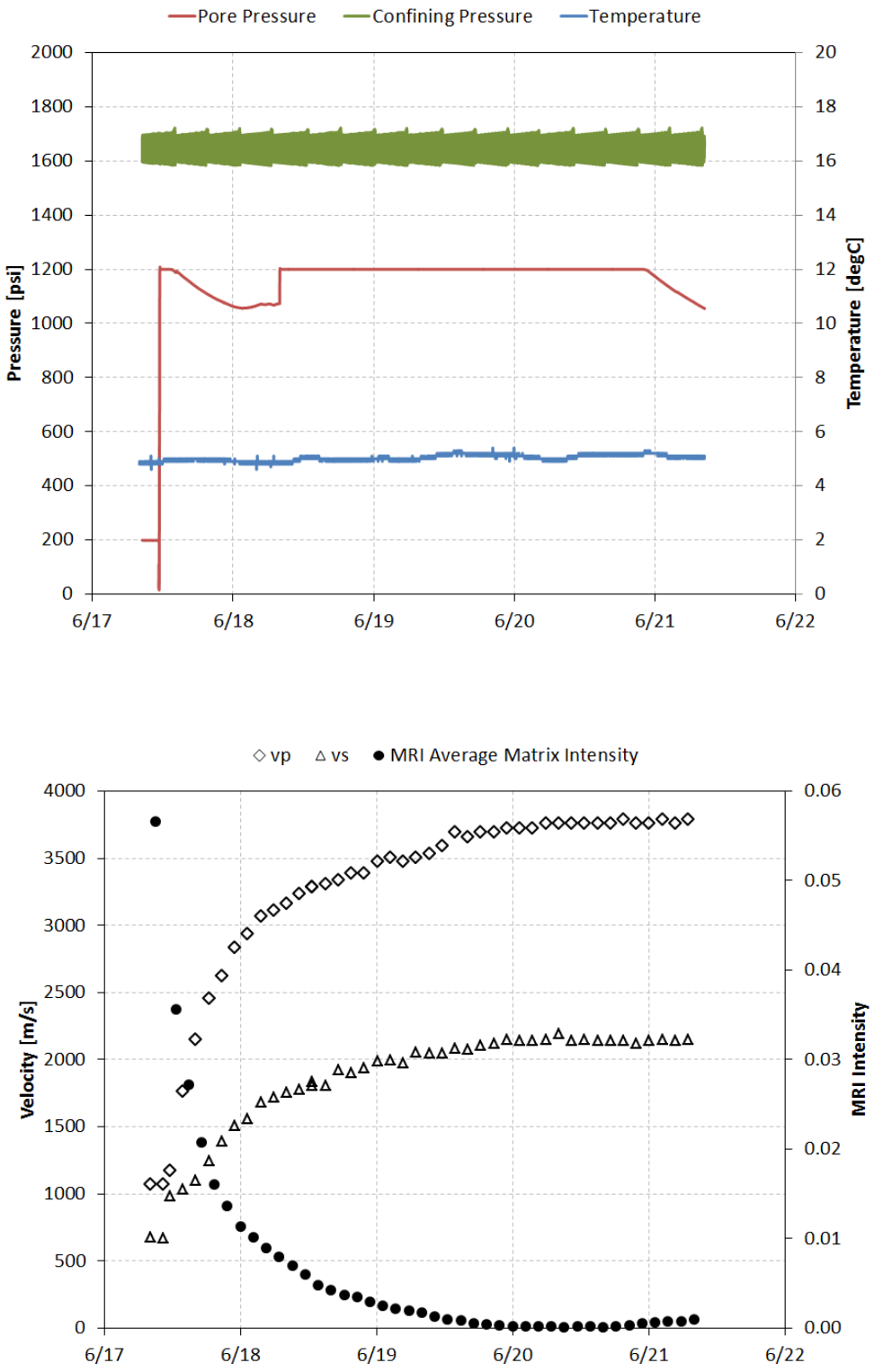

Figure 3.10: Experiment 2 (Formation 2) – CH_4 Hydrate Formation in partially water-saturated Ottawa Sand F110 low initial water saturation (S_{wi}=0.146)

2004; Prasad and Dvorkin, 2004]. At the end of the experiment, velocities reached v_p=3774±217 and v_s=2144±83 m/s with P_d=453±47 psi (3.131 MPa). Note that these velocities exceeded those of the first despite the lower overall hydrate content. Also, during the second formation velocities were unresponsive to changes in P_d, whereas velocities recorded during the first formation were noticeably affected.

3.3.2.2 Experiment 3

Experiment 3 was conducted to observe CH_4 hydrate formation in a wet sandpack originally prepared with a low S_{wi} (=20.5%). At a constant pore pressure of 1200±1 psi (8.276 MPa) the sample was cooled to 4.6±0.2°C (Figure 3.11). The resulting response of MRI intensity and velocities was similar to those observed in Experiment 2. A rapid change in both MRI intensity and velocities in the first few hours was followed by a significant decrease in the rate of change during the following days. In the first six hours, the MRI intensity decreased by 86.4% and velocities increased to v_p=2692±198 m/s and vs=1663±114 m/s at P_d=439±26 psi (3.028 MPa). In the following four days, the MRI intensity slowly decreased, for a total intensity reduction of 94.7%. At the end of the experiment v_p and v_s reached 2964±75 m/s and 1874±50 m/s at P_d=402±28 psi (2.772 MPa).

3.3.2.3 Experiment 4

In Experiment 4, a second partially water-saturated sandpack with high S_{wi} (=80.8%) was subjected to CH_4-hydrate formation at T=5.7±0.1°C and P_p=1200±1 psi

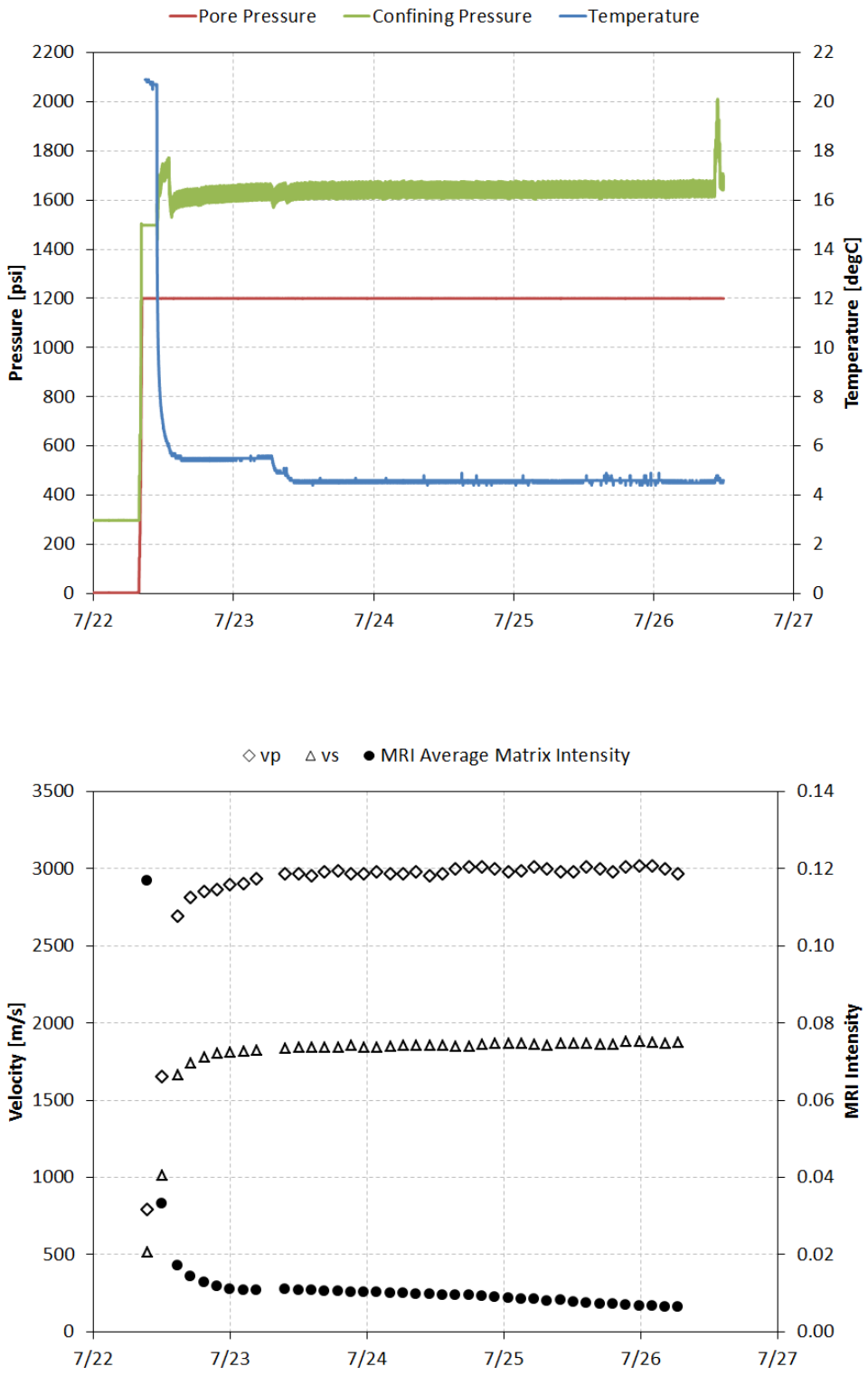

Figure 3.11: Experiment 3 (Formation 1) – CH_4 Hydrate Formation in partially water-saturated Ottawa Sand F110 low initial water saturation (S_{wi}=0.205)

(8.276 MPa). The sample was first pressurized and then cooled (Figure 3.12). T was higher than in Experiment 2, thus providing a lower driving force for hydrate formation. Consequently a lower hydrate formation rate was observed compared to Experiment 2. Over the course of three days, almost linearly increasing velocities and decreasing in MRI intensities were observed. This was attributed to the high ratio of water to CH_4 as well as to the relatively high temperature. After three days, the temperature was lowered to 4.7±0.3°C. The temperature decrease provided additional driving force for hydrate formation. As a result, the rate of velocity increase and MRI-intensity decrease increased for a short period of time. After 24 hours, MRI intensities and velocities stabilized. At this point, the MRI intensity had been reduced by only 49.5%. Subsequent gas-injection tests revealed that the fluid pathways into the sample had been congested by CH_4 hydrate plugs. It is likely that all the gas available for hydrate formation inside the sandpack had been consumed and that the inability to provide additional CH_4 had stopped the hydrate formation process. Nevertheless, the hydrate formation up to this point had increased v_p and v_s to 2497±83 m/s and 1005±30 m/s, respectively P_d=579±25 psi (3.993MPa). As a consequence of the fluid-flow difficulties experienced during Experiment 4, semi-permeable ceramic plates were added to the sample assembly for subsequent measurements for flow assurance.

3.3.2.4 Experiment 5

During Experiment 5, a series of 10-minute MRI profiles was acquired instead of the 2-hour 3D MRI images. This modification allowed an increased sampling rate of MRI intensities. The focus of Experiment 5 was the formation, dissociation, and re-formation

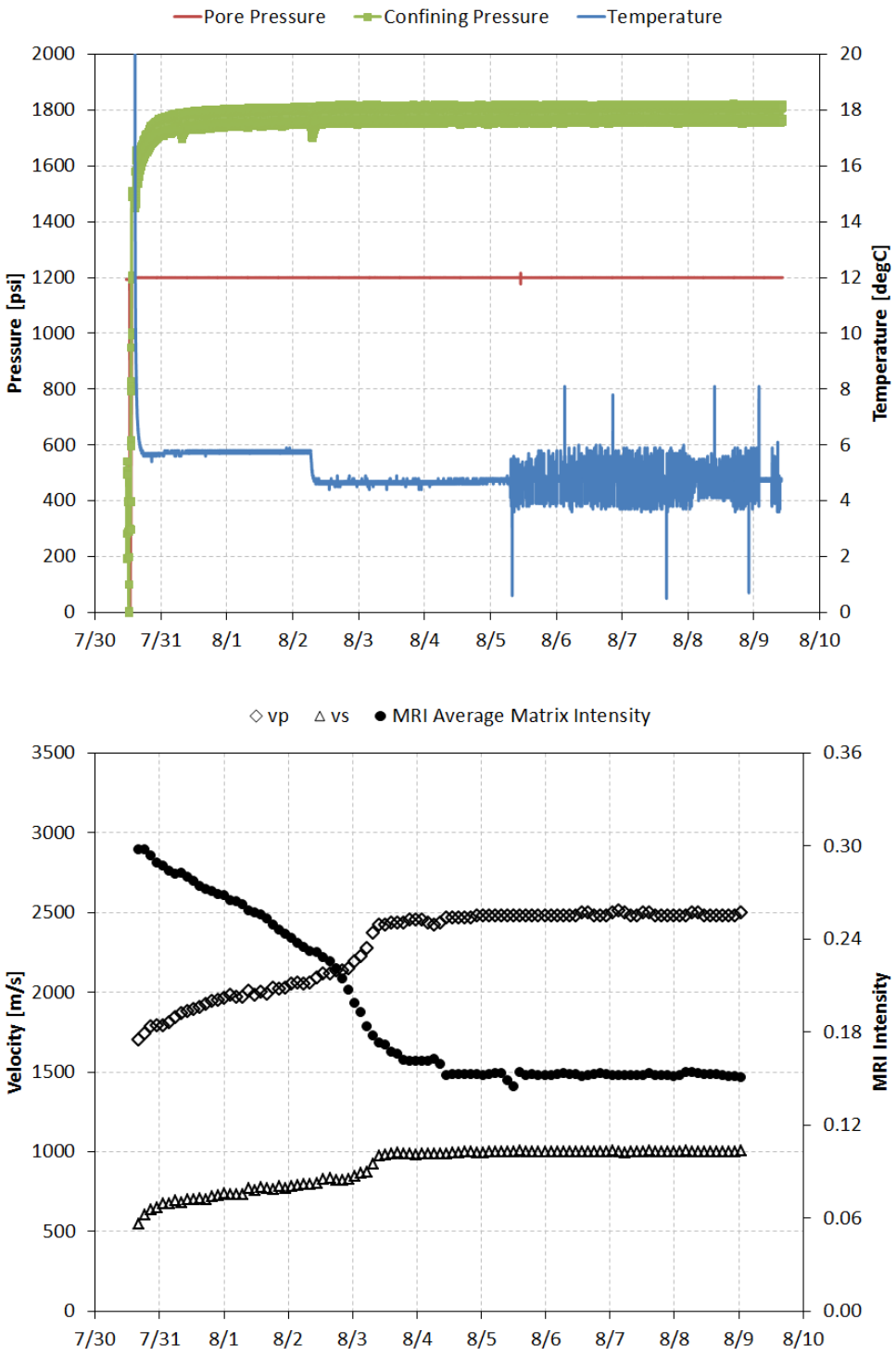

Figure 3.12: Experiment 4 (Formation 1) – CH_4 Hydrate Formation in partially water-saturated Ottawa Sand F110 high initial water saturation (S_{wi}=0.808)

of CH_4 hydrate in a partially water-saturated sandpack with low initial water saturation (S_{wi}=21.6%). The order of pressurization, cooling, de- and re-pressurization was the same as in Experiment 2, as was the observed response of MRI intensity and velocities to hydrate formation (Figure 3.13). A fast initial rate of hydrate formation preceded a significantly slower rate as indicated by the rates at which velocity increased and MRI intensity decreased. Hydrate-formation pressure and temperature during the first formation were P_p=1200±1 psi (8.276 MPa) and T=4.2±0.1°C, respectively. Within 24 hours, the MRI intensity dropped to 11.1% of its original value and v_p and v_s reached 2626±63 m/s and 1733±0 m/s at P_d=542±2 psi (3.738 MPa). After the subsequent depressurization, S_{wi} was reduced to 0.169. The second formation sequence occurred at the same thermobaric conditions as the first one (Figure 3.14). Velocities increased to v_p=3129±75 m/s and v_s=1951±46 m/s (P_d=540±26 psi, 3.734 MPa) over the course of 24 hours and MRI intensity decreased to 12.3% of its value at the beginning of the second cycle.

3.3.3 Ultrasonic Velocities as Functions of Hydrate Saturation

Figures 3.15 and 3.16 show v_p and v_s as functions of S_h. For hydrate formation in partially water-saturated sand with low S_{wi}, (Figure 3.15) v_p and v_s both increase exponentially with increasing CH_4 hydrate content. While the order of cooling and pressurization obviously affected the rate of hydrate formation (Section 3.3.2.1), the change in velocities with changing S_h appeared to be unaffected by whether the sample was cooled or pressurized first. Instead, velocities recorded during hydrate formation exhibited a noticeable dependence on S_{wi}. As can be seen in Figure 3.15, increasing S_{wi}

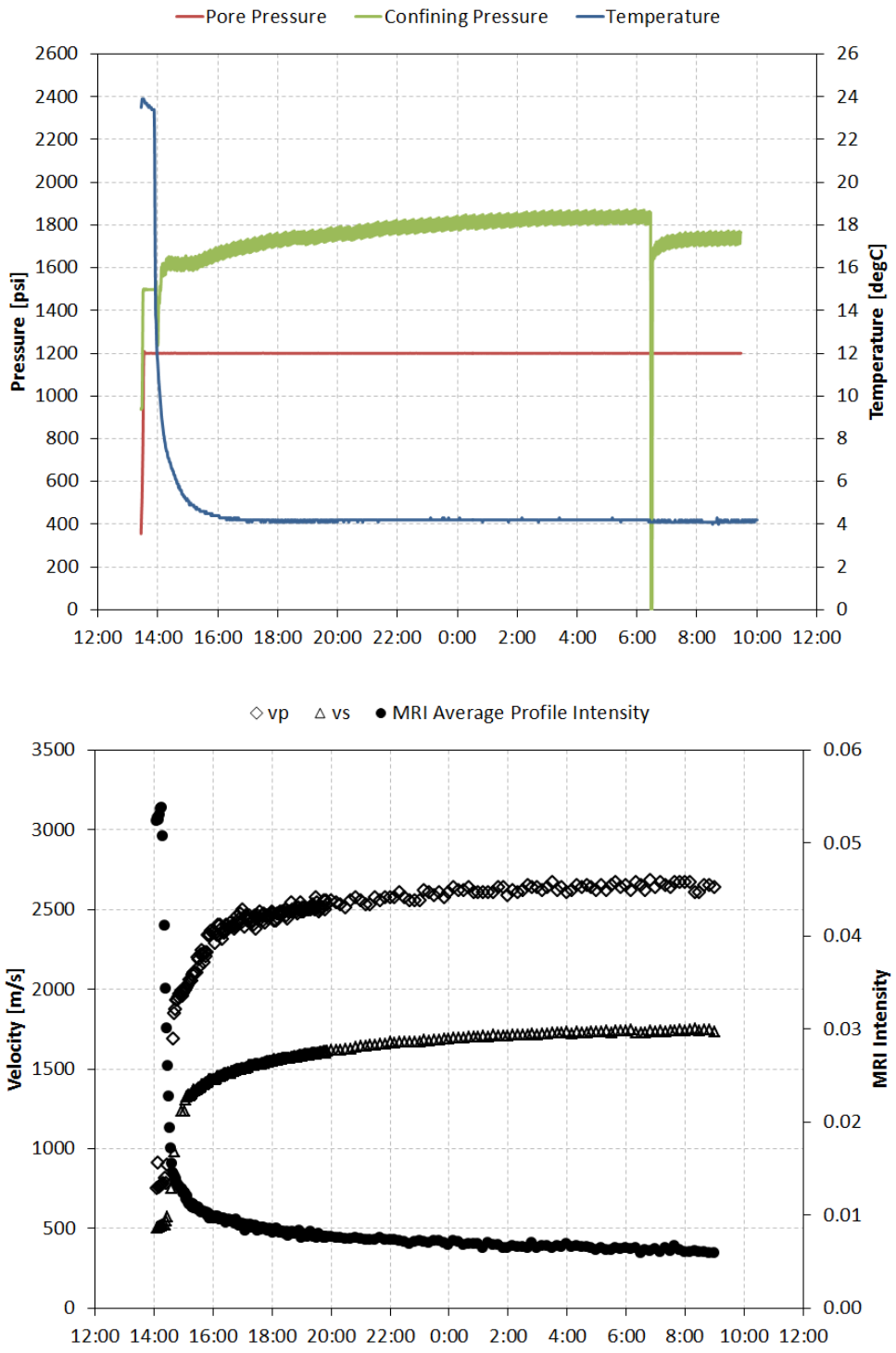

Figure 3.13: Experiment 5 (Formation 1) – CH_4 Hydrate Formation in partially water-saturated Ottawa Sand F110 low initial water saturation (S_{wi}=0.216)

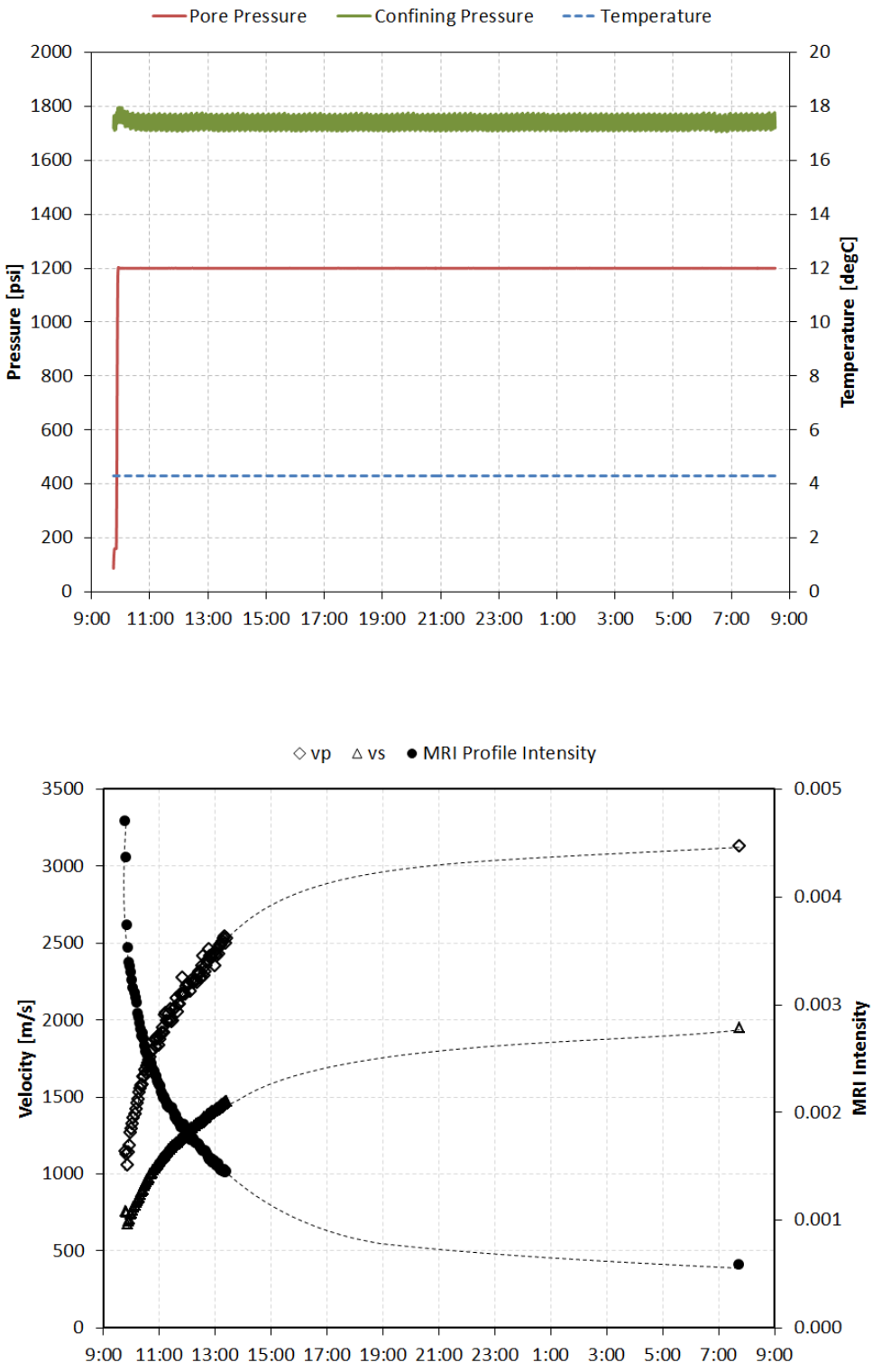

Figure 3.14: Experiment 5 (Formation 2) – CH_4 Hydrate Formation in partially water-saturated Ottawa Sand F110 low initial water saturation (S_{wi}=0.189)

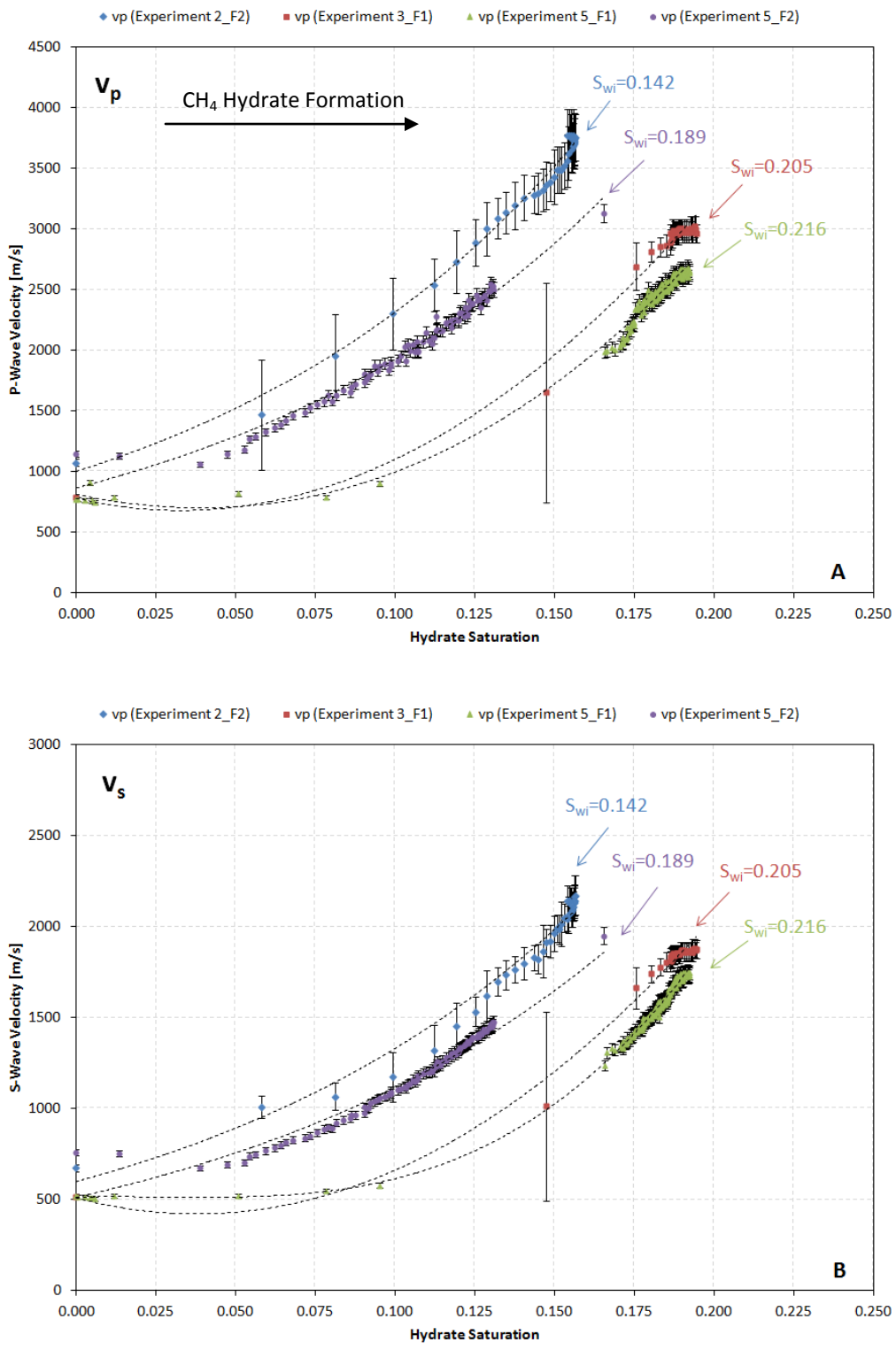

Figure 3.15: Measured v_p (A) and v_s (B) for CH_4 hydrate formation in sand with low S_{wi} (Error bars for hydrate saturation have been omitted for clarity. The uncertainty for the hydrate saturation overall is less than 0.05).

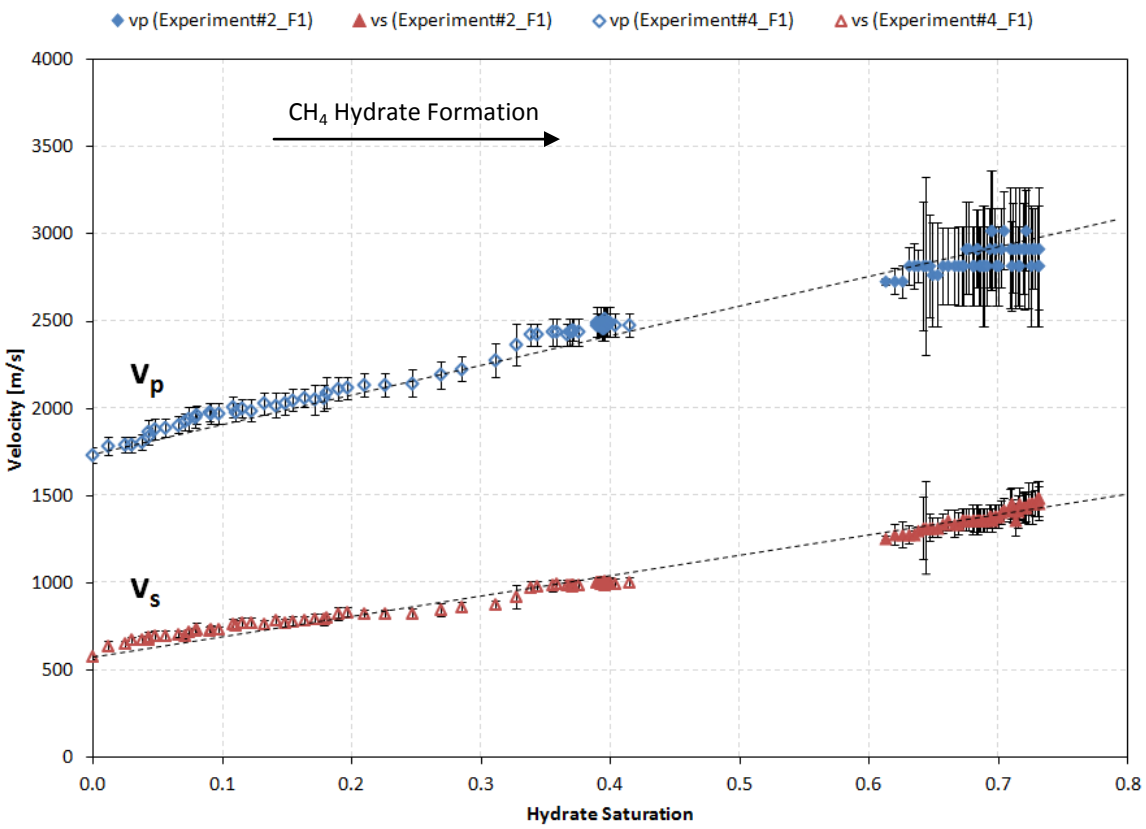

Figure 3.16: v_p and v_s of CH_4 hydrate formation in sand with high S_{wi} (Error bars for hydrate saturation have been omitted for clarity. The uncertainty for the hydrate saturation overall is less than 0.05).

resulted in a reduction in the overall rate of velocity increase during hydrate formation. CH_4 hydrate formation in specimens with high S_{wi} exhibited a linear increase in velocities (Figure 3.16) over the complete range of hydrate saturations.

The final velocities for each specimen also decreased with increasing initial water saturation. However, with exception of Experiment 2 (Formation 2), no specimen reached full conversion to hydrate. At the end of each experiment, 5-12% of the pore water remained unconverted in the pore space (Table 3.5). It is unclear if v_p and v_s would have exceeded the values obtained in Experiment 2 had all water been converted into hydrate. Results obtained in previous studies [Waite et al., 2004; Priest et al., 2005; 2009] suggest that this may be the case.

Table 3.4: Conversion of water to hydrate achieved in samples with low S_{wi}

Sample	S_{wi}	$S_{w,res}$	Conversion
Experiment 2_F2	0.146	0.000	1.00
Experiment 3_F1	0.205	0.011	0.95
Experiment 5_F1	0.216	0.024	0.89
Experiment 5_F2	0.189	0.023	0.88

Figure 3.17 shows v_p and v_s as functions of S_h obtained in this study in comparison with velocity data reported by Waite et al. [2004], Priest.et al. [2005; 2009], and Ebinuma et al. [2008]. In all studies, CH_4 hydrate was formed with CH_4 as a free gas phase. Similar to the study at hand, Ebinuma et al. [2008] measured ultrasonic velocities in during CH_4 hydrate formation. Waite et al. [2004] and Priest et al. [2005; 2009] only reported post-formation velocities of several CH_4 hydrate-bearing specimens

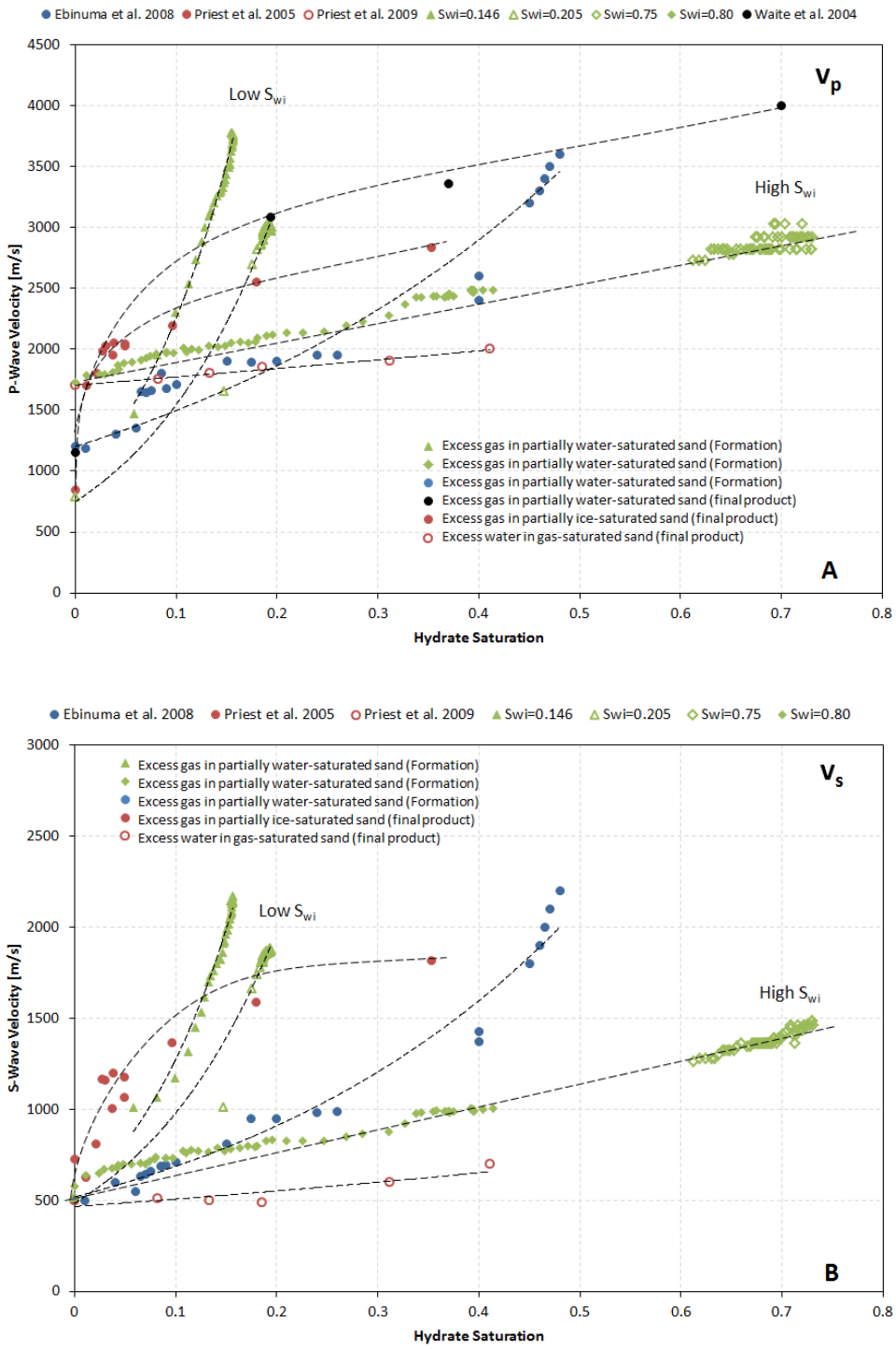

Figure 3.17: v_p (A) and v_s (B) as functions of S_h - Comparison of velocity trends observed during hydrate formation (green and blue data points) and those recorded for gas hydrate-bearing samples with different S_h (Note that Waite et al. [2004] and Priest et al. [2005] did not report velocities measured prior to hydrate formation. Consequently, values for S_h=0 reported for the ILCP were used here)

each with a different hydrate saturation. During the formation of the samples formed for this study, velocities increased exponentially, whereas the velocities measured in the final product showed a steep increase in v_p and v_s at low S_h. At S_h>20-30%, the velocities continued to increase but at a significantly slower rate.

Note that in addition to forming CH_4 hydrate-bearing samples through gas injection into partially water-saturated sand, Priest et al. [2009] also used the "excess water method", whereby water is injected into a gas-saturated sample. Thereby the initial gas volume determined the resulting hydrate saturation. Similar to hydrate formation out of solution, v_p and v_s in did not change significantly with S_h when the hydrate-bearing samples were formed with the excess water method.

3.3.4 Error Calculations

The errors reported for the recorded velocities depended on the uncertainties associated with measuring sample length and picking the arrival time of the ultrasonic pulse. The relative errors for the velocities were determined through error propagation calculations (Equation 1):

$$\frac{\Delta V}{V} = \sqrt{\left(\frac{\Delta L}{L}\right)^2 - \left(\frac{\Delta t}{t}\right)^2} \tag{3.1}$$

where L is the sample length and ΔL the error associated with measuring L. t is the arrival time of the ultrasonic pulse and Δt the error associated with picking t. As mentioned above, L was measured with a precision of ΔL=±0.001 m based on MRI profiles of the partially water-saturated sample. Δt was assumed to correspond to the

sampling interval of the ultrasonic waveform. Values for Δt varied among experiments and are listed in Table 3.6. During most experiments, $\Delta V_{p,s}$ ranged between 2.3 and 2.7%. These relative errors are on the lower end of the uncertainty range reported in Chapter 2. The samples used in this study were twice as long as the ones tested for the inter-laboratory comparison study presented in Chapter 2. In addition, the pre-shrunk heat-shrink tubing surrounding the sample provided a guide rail for the end plates, so that they were well aligned and parallel. As a result, the relative error could be kept relatively small. In most cases, acquiring the 3D MRI images took up to two hours, during which time the hydrate saturation and ultrasonic velocities continued changing. Each data point of average MRI intensity corresponds to a range of hydrate saturations and ultrasonic velocities. To plot ultrasonic velocities as a function of hydrate saturation, velocities obtained at the beginning and end of each 3D MRI data-set were averaged and their difference used as the respective error.

Table 3.5: Sampling rate of waveforms

Sample	Δt [s]
Experiment 1_D	$5 \cdot 10^{-7}$
Experiment 2_F1	$1 \cdot 10^{-6}$
Experiment 2_F2	$5 \cdot 10^{-7}$
Experiment 3_F1	$1 \cdot 10^{-7}$
Experiment 4_F1	$2 \cdot 10^{-7}$
Experiment 5_F1	$1 \cdot 10^{-7}$
Experiment 5_F2	$1 \cdot 10^{-7}$

3.4 Summary of Key Observations

Ultrasonic velocities were recorded during hydrate formation from gas-phase CH_4 in partially water saturated Ottawa F110 sand as well as during the dissociation of hydrate formed out of solution from THF. Simultaneously with the velocity measurements, MRI intensity data were recorded which allowed the calculation of v_p and v_s as functions of the hydrate saturation during hydrate formation or decomposition. The following observations were made concerning the formation of CH_4 hydrate and the dissociation of THF hydrate:

- In partially water-saturated sand with low S_{wi} (about 20%), v_p and v_s increase exponentially during hydrate formation.
- With increasing S_{wi}, the increase in velocity with S_h decreases. For the same S_h, samples with lower S_{wi} exhibit higher v_p and v_s.
- In partially water-saturated sand with high S_{wi} (about 80%), v_p and v_s increase almost linearly during hydrate formation.
- The velocity-S_h trend for CH_4 hydrate-bearing sediments (final product) that have been formed from free gas differs from the one observed during hydrate formation. For the latter case, velocities increase exponentially with increasing S_h, while in the first case velocities increase inverse exponentially.
- In THF hydrate-bearing sediment, v_p and v_s decreased steadily with decreasing hydrate saturation during hydrate dissociation. Below S_h of about 30%, velocities were nearly constant with S_h.

- The same velocity trend is observed for THF hydrate dissociation, THF hydrate-bearing sandpacks with varying final hydrate saturations, and CH_4 hydrate formation out of solution.
- The v_p-S_h trend for THF hydrate appeared to be independent of whether velocities are measured during formation, dissociation, or of final product. Thus, the manner in which THF hydrate forms and dissociates seems to be reversible. The same is not true for the dissociation of CH_4 hydrate formed out of solution.
- THF hydrate showed signed of dissociation (decrease of velocity and MRI intensity) despite temperatures still being inside the hydrate stability region. This was likely due to the temperature-dependent THF-solubility of the surrounding pore water causing dissolution of the THF hydrate.

In the subsequent chapter, we compare the experimental data reported in this chapter to theoretical values calculated from current rock physics models for gas hydrate-bearing sediments. These models describe the relationship between the pore-scale distribution of gas hydrate in sediment and velocity. The comparison will enable us to interpret the experimental results presented here and relate the method of hydrate formation (i.e. the initial water saturation) to the pore-scale distribution of the hydrate and the resulting ultrasonic velocities of the hydrate-bearing sediment.

CHAPTER 4

COMPARISON OF ROCK PHYSICS MODELS FOR GAS HYDRATE-BEARING SEDIMENT WITH LABORATORY DATA

In this chapter, state-of-the-art rock physics models for gas hydrate-bearing sediments, such as the effective medium theory, Lee's weighted equation, the three-phase Biot theory, and Santamarina's cemented soil model are reviewed and used to calculate p- and s-wave velocities (v_p and v_s) as a functions of hydrate saturation (S_h). The calculated velocities are compared to results of hydrate-formation experiments in unconsolidated sediment samples with varying initial water saturations (S_{wi}). In comparing experimental and modeled data, we apply the models in a non-standard fashion, adjusting the fitting parameters inherent in the rock physics models to examine velocity-S_h trends observed during hydrate formation rather than after hydrate formation is complete. By linking experimental hydrate formation methods with the hydrate pore scale distributions described by the models, we gain insight on how the water saturation prior to hydrate formation controls the distribution of water and gas in the pore space, which, in turn determines the hydrate habit and how velocities increase during hydrate synthesis. In particular, by taking into account the effect of gas present and incorporating the empirically determined relationship between initial water saturation and hydrate habit parameter, the cemented soil model from Santamarina and Ruppel [2008, 2010b] manages to capture the effect of hydrate formation on ultrasonic velocities in unconsolidated sediment over the full range of initial water saturations

4.1 Introduction

In Chapter 3, we observed that when hydrate is formed from an excess free gas phase in partially water-saturated samples, the initial water saturation (S_{wi}) prior to hydrate formation determines the rate of velocity increase with increasing hydrate saturation. For samples with low S_{wi} velocities increase exponentially. The rate of velocity increase, however, decreases with increasing S_{wi}. At high S_{wi}, velocities increase almost linearly. When hydrate is formed out of solution, velocities do not increase until a hydrate saturation (S_h) of about 30-40% is exceeded. In this chapter, we compare our experimental results with velocities calculated with rock physics models for gas hydrate-bearing sediments to gain insight into the physics that govern the observed behavior of ultrasonic velocities in unconsolidated sediment during hydrate formation.

A handful of rock physics models have been developed for gas hydrate-bearing sediments that relate elastic velocities to the gas hydrate saturation. These models include the effective medium theory [Helgerud et al., 1999; Sava and Hardage, 2009], Lee's weighted equation [Lee et al., 1996], the three-phase Biot Theory [Lee and Waite, 2008], and Santamarina's cemented soil model [Santamarina and Ruppel, 2008, 2010; Santamarina et al., 2001]. Each model accounts for the pore-scale distribution of hydrate in one way or another. The effective medium theory comprises four models, each of which describes a separate hydrate morphology. Lee's Weighted Equation, Santamarina and Ruppel's Cemented Soil model, and the Three-Phase Biot-Theory each contain fitting parameters that are adjusted based on the pore-scale distribution expected for the respective hydrate-bearing system. Here we review the different rock physics models with respect to the method of hydrate synthesis and calculate v_p and v_s

as functions of hydrate saturation. The theoretical velocity curves are then compared to the laboratory data described in Chapter 3 and summarized above.

As the rock physics models presented here were developed to determine S_h in natural gas hydrate reservoirs based on v_p and v_s measurements, such as seismic or sonic logging, they were designed for static three-phase systems composed of sediment, hydrate and either water or gas. The experimental data acquired here however, were measured during the dynamic processes of hydrate formation or dissociation. As discussed in Chapter 3, the relationship between v_p, v_s, and S_h is not necessarily the same for hydrate formation, dissociation, or separate samples with different hydrate saturations: for THF hydrate, the velocity-S_h trend is the same for the static and dynamic systems, but this is not true for CH_4 hydrate. Consequently, though we expect the models to accurately predict the velocity-S_h trends after CH_4 hydrate formation is complete, we do not expect model fits to match the velocity-S_h trends during CH_4 hydrate formation. However, by adjusting available fitting parameters related to the hydrate habit so as to match v_p and v_s acquired for the dynamic systems, we can 1) extend the models to dynamic systems and 2) gain insight into probable distributions of hydrate in the pore space. The latter will allow conclusions to be drawn about how hydrate forms in unconsolidated sediment.

Additionally, the calibrated rock physics models will allow ultrasonic velocities to be used as tools for estimating the hydrate saturation in sandpacks used in laboratory experiments designed to study physical properties of hydrate-bearing sediment other than ultrasonic velocities. Note, however, that before the ultrasonic-velocity data obtained in the laboratory can be applied to low-frequency velocities acquired in the

field (sonic logs or seismic), dispersion and attenuation has to be studied in gas hydrate-bearing sediments as their elastic properties may be frequency-dependent [Priest et al., 2006; Kingston et al., 2008; Pohl, 2012].

4.2 Review of State-of-the-Art Rock Physics Models

The following section provides an overview of the rock physics models we considered for gas hydrate-bearing sediments. We begin with a brief summary of the effective medium theory for gas hydrate-bearing sediment. This theory encompasses four different models, each describing a different type of hydrate morphology. We will then present the semi-empirical relationships starting with the Weighted Equation proposed by Lee [1996], followed by the Three-Phase Biot Theory [Lee and Waite, 2008], and conclude with the Cemented Soil Model proposed by Santamarina and Ruppel [2008, 2010]. The objective is to highlight fitting parameters in these models and their physical significance with respect to the hydrate pore-scale distribution.

4.2.1 Effective Medium Theory

Ecker et al. [1998] developed an effective medium theory for gas hydrate-bearing sediments. This theory considers two mechanically extreme hydrate morphologies [Chand et al. 2004]: “cementing” and “non-cementing.” The cementation models consider gas hydrate to be part of the sediment matrix either as a grain contact cement (“contact-cementing”) or as enveloping whole grains (“enveloping-cementing”). The theory is based on the cementation model by Dvorkin & Nur [1996]. Effective elastic moduli are calculated for a pack of idealized identical spheres cemented by the hydrate.

Normal and tangential stiffness of the pack are a function of the ratio of the cemented contact radius to the grain radius, which depends on the respective hydrate habit. The non-cementing model considers gas hydrate to be part of the pore fluid and not to affect the strength of the sediment frame ("pore-filling"). Hertz-Mindlin theory [Mindlin, 1949] and the modified lower Hashin-Shtrikman bound [Dvorkin and Nur, 1996] are utilized to obtain the effective moduli of the dry sediment frame. In both the cementing and non-cementing cases, Gassmann fluid substitution [Gassmann, 1951] accounts for the type of pore fluid present. The theory was extended by Helgerud et al. [1999]. The extension distinguishes porosities higher and lower than the critical porosity (ϕ_c) by utilizing both upper and lower modified Hashin-Shtrikman bounds. In addition, the "load-bearing" model was introduced. In this model, the hydrates are treated as non-cementing mineral components that contribute to the matrix stiffness. The elastic moduli of the mineral matrix are calculated using Hill's mineral-modulus average [Hill 1952]. Sava & Hardage [2009] then proposed the use of Walton's contact theory [Walton, 1987] instead of Hertz-Mindlin to calculate the effective moduli of the sediment framework. Walton's model assumes no friction between grains, which results in zero tangential stiffness and reduces the effective shear modulus.

4.2.2 Lee's Weighted Equation

To calculate p-wave velocities in gas hydrate-bearing sediments, Lee et al. [1996] proposed a semi-empirical weighted average equation that combines Wyllie's time average equation [Wyllie et al., 1958; Pearson et al., 1983] and Wood's equation [Wood, 1941].

$$\frac{1}{v_p} = \frac{W\phi(1-S_h)^n}{v_{wood}} + \frac{1-W\phi(1-S_h)^n}{v_{wyllie}} \quad (4.1)$$

ϕ is the sediment porosity and S_h the hydrate saturation. W is the weighting factor and n the cementation factor. Both are empirical parameters. P-wave velocities v_{wyllie} and v_{wood} are calculated as shown below and represent mechanical end members. Wyllie's time average equation was developed for consolidated sediments, whereas the Wood equation describes particles in suspension. Wyllie's time average equation averages the inverse of the p-wave velocity (slowness) over the weighted volumetric sum of the different components. Timur [1968] extended the equation to three phases to predict velocities in frozen sediments before Pearson [1983] applied the following expression for gas hydrate-bearing sediments:

$$\frac{1}{v_{wyllie}} = \frac{\phi(1-S_h)}{v_w} + \frac{\phi S_h}{v_h} + \frac{(1-\phi)}{v_m} \quad (4.2)$$

v_w, v_h, and v_m are the p-wave velocities of water, hydrate and the host sediment, respectively. For the same three-phase system, the Wood equation is defined as follows [Lee et al. 1996]:

$$\frac{1}{\rho v_{wood}^2} = \frac{\phi(1-S_h)}{\rho_w v_w^2} + \frac{\phi S_h}{\rho_h v_h^2} + \frac{(1-\phi)}{\rho_m v_m^2} \quad (4.3)$$

ρ_w, ρ_h, and ρ_m are the densities of water, hydrate, and host sediment, respectively. The bulk density ρ is the volumetric average of the component densities. In Lee's weighted

equation (Equation 4.1), the cementation exponent (n) simulates the rate of cementation due the presence of hydrates. The weighting factor (W) represents the state of non-consolidation of the host sediment and is estimated from p-wave velocities in sediments without gas hydrates. Larger values of W favor the Woods equation and are appropriate for less consolidated sediments. The cementation exponent (n) accounts for the cementation of the sediment due to the presence of gas hydrate. It has to be adjusted with respect to the hydrate habit.

4.2.3 Three-Phase Biot Theory

Carcione and Tinivella [2000] modeled the elastic properties of water-saturated hydrate-bearing sediments based on Biot's theory of poroelasticity [Biot, 1962]. The model follows Leclaire et al. [1994, 1995] who developed the approach for frozen porous media. The model assumes the presence of two fluid-filled solid interwoven frameworks: sediment and hydrate. Each framework exhibits characteristic elastic moduli that are combined in a shear and a stiffness matrix (R_{ij} and μ_{ij}). At the low-frequency limit dispersion becomes negligible and the elements of R_{ij} and μ_{ij} are real. Following Lee & Waite [2008], p- and s-wave velocity can be calculated from the following equations:

$$v_p = \sqrt{\frac{\sum_{i,j}^{3} R_{ij}}{\rho_b}} \quad \text{and} \quad v_s = \sqrt{\frac{\sum_{i,j}^{3} \mu_{ij}}{\rho_b}} \tag{4.4}$$

ρ_b is the average bulk density. The elements of R_{ij} and μ_{ij} are functions of porosity, pore fluid viscosity, angular frequency, the individual density, bulk, and shear moduli of the

fluid, sediment and the hydrate, as well as the bulk and shear moduli for the hydrate and sediment frameworks (K_{hm}, μ_{hm}, and K_{sm}, μ_{sm}, respectively). Carcione & Tinivella [2000] derive K_{sm} from logs using inverse Gassmann fluid substitution. μ_{hm}, and K_{sm}, μ_{sm} are calculated after Krief et al. [1990] using Kuster-Toksöz moduli [Kuster & Toksöz 1974].

$$\mu_{sm} = \mu_{sm0} + (\mu_{mKT} - \mu_{sm0})(\phi_s/\phi)^{3.8} \quad (4.5)$$

$$K_{hm} = K_{hKT}(\phi_h/\phi)^{3.8} \quad (4.6)$$

$$\mu_{hm} = \mu_{hKT}(\phi_h/\phi)^{3.8} \quad (4.7)$$

μ_{sm0} is the wet rock shear modulus, ϕ_s and ϕ_h are solid grain and hydrate fraction, respectively. K_{mKT}, K_{hKT}, μ_{hKT}, are Kuster-Toksöz bulk and shear moduli for hydrate and sediment grains. Gei and Carcione [2003] generalized the approach for a partially saturated system composed of grains, hydrate, water and gas and included the effect of effective pressure on the sediment framework. The elastic moduli of the sediment framework were calculated as follows:

$$K_{sm} = \beta K_{HS}\left(1 - e^{-\frac{P_e}{P_e^*}}\right) \quad (4.8)$$

$$\mu_{sm} = \beta \mu_{HS}\left(1 - e^{-\frac{P_e}{P_e^*}}\right) \quad (4.9)$$

P_e is the effective pressure, K_{HS} and μ_{HS} represent Hashin-Shtrikman Upper Bounds [Hashin and Shtrikman, 1963], P_e^* and β are empirical factors that are obtained by

fitting moduli by Krief et al. [1990] and regional data, respectively. Lee & Waite [2009] derived the elastic moduli for hydrate and sediment frames (K_{hm}, μ_{hm}, K_{sm}, and μ_{sm}) using expressions by Pride et al. [2004] and Lee [2005]:

$$K_d = \frac{K_s(1-\phi)}{(1+\alpha\phi)} \quad \text{and} \quad \mu_d = \frac{\mu_s(1-\phi)}{(1+\gamma\alpha\phi)} \text{ , where } \gamma = \frac{1+2\alpha}{1+\alpha} \tag{4.10}$$

K_d and μ_d represent K_{hm} or K_{sm} and μ_{hm} or μ_{sm} respectively. K_s and μ_s are bulk and shear moduli of either hydrate or sediment grains. α is the so-called consolidation parameter, which accounts for sediment stiffening caused by consolidation. The location of the hydrate in the pore space is accounted for in the apparent porosity of sediment frameworks, which is given by $\phi_{as} = \phi_w + \varepsilon\phi_h$, where ϕ_w and ϕ_h are water and hydrate saturation, respectively. If the empirical parameter ε=1, the hydrate is pore filling and not contributing to the matrix stiffness. If ε=0, the hydrate is considered part of the mineral frame, forming load-supporting contacts between sediment grains [Lee & Waite, 2008].

4.2.4 Santamarina's Cemented Soil Model

Santamarina and Ruppel [2008, 2010] experimentally investigated the stress-dependency of shear wave propagation in unconsolidated sediments with and without THF hydrate. Based on their observations, they adapted the following semi-empirical expression for v_s:

$$v_s{}^2 = \theta\left(\frac{v_{s,h}S_h{}^2}{\phi}\right)^2 \Theta + \left[\alpha\left(\frac{\sigma_v+\sigma_h}{2kPa}\right)^\beta\right]^2 \tag{4.11},$$

where φ is the porosity, $v_{s,h}$ is the shear-wave velocity of hydrate, S_h is the hydrate saturation, and σ_v and σ_h are vertical and horizontal stress, respectively. The first term accounts for the presence of hydrate and the second one for effective stress. Equation 4.11 contains three fitting parameters, α, β, and θ. α represents v_s at an effective pressure equal to 1 kPa, and β accounts for the stress-dependency of v_s. The parameter θ represents the pore scale distribution of hydrate in sediment, or, in other words, the degree of cementation. As can be seen in Equation 4.11, at high hydrate concentration and/or high Θ, the v_s becomes hydrate-controlled. For hydrate that formed out of solution, such as THF hydrate, and which is generally considered as being located away from the grains, θ is about 0.15 [Yun et al., 2005]. For hydrate formed from a free gas phase, larger θ are expected as this type of hydrate is believed to cause cementation of sand grains [Santamarina and Ruppel, 2008, 2010]. v_p is calculated as a function of v_s with the following Biot-Gassmann-type equation [Santamarina et al., 2001]:

$$v_p{}^2 = v_s{}^2 \left(\frac{1-\nu_{sk}}{1-2\nu_{sk}} + \frac{4}{3}\right) + \frac{1}{\rho_{mix}} \left(\frac{1-\phi}{K_s} + \phi\left(\frac{S_h}{K_h} + \frac{1-S_h}{K_f}\right)\right)^{-1} \quad (4.12).$$

v_{sk} is the Poisson's ratio for the sediment frame (typically about 0.1), ρ_{mix} is the bulk density and depends on S_h. K_s, K_h, and K_f are bulk moduli for the sediment grains, hydrate, and pore fluid. In the following, the expressions proposed by Santamarina and Ruppel [2008, 2010] will be referred to as Santamarina's cemented soil model.

4.3 Comparison with Laboratory Data

Theoretical v_p and v_s were calculated as functions of S_h for three-phase systems made up of sediment, hydrate and either water or gas. The elastic properties of each component used in the calculations are listed in Table 4.1. Note that several authors reported elastic properties of pure gas hydrate [e.g Bathe et al., 1984; Waite et al., 2000]. The most comprehensive study was performed by Helgerud et al. [2003, 2009]. They derived empirical relationships for v_p and v_s as functions of P and T based on the results of ultrasonic velocity measurements of polycrystalline CH_4 hydrate. The results matched data measured for single crystal CH_4 hydrate [Kiefte et al., 1985]. No significant difference in elastic properties was obvious with respect to structures I and II at the temperature-pressure ranges used in the experiments. The sediment porosity in the model calculations at hand was assumed to be 0.39. Temperature, pore-, and differential pressure were chosen as 4°C, 8.2 MPa and 3 MPa, which approximately matched the experimental conditions of the laboratory velocity measurements.

The laboratory data used in the model comparison study was acquired through ultrasonic velocity measurement on THF and CH_4 hydrate-bearing Ottawa Sand F110, as was described in Chapter 3. The CH_4 hydrate-bearing samples were formed through CH_4 injection into partially water saturated sandpacks with initial water saturations of 20 and 80 percent ("Low and High S_{wi}"). MRI scans monitored changes in S_h during the formation of CH_4 hydrate formation. THF hydrate-bearing samples were formed outside the MRI scanner by cooling sandpacks that were fully saturated with a THF-H_2O solution. MRI scans then monitored changes in S_h during THF hydrate dissociation. Comparing the resulting velocity-S_h trends with literature data [Yun et al., 2005;

Spangenberg et al., 2008; Pohl, 2012] indicated that, in terms of elastic properties, THF hydrate formation and dissociation in sediment are reversible, with no observable hysteresis. The uncertainty associated with the measured velocity values was about 3.5% for both v_p and v_s.

Table 4.1: Elastic Properties used as Input Parameters

Component	ρ [kg/m^3]	K [GPa]	G [GPa]
Quartz	2650	36.6	45
Hydrate	925	8.38	3.52
Water	1000	2.25	0
CH_4	10.8	0.021	0

4.3.1 Effective Medium Theories

We calculated v_p and v_s using the four models of the effective medium theory for systems composed of quartz sand, hydrate, and methane gas (Figures 4.1 and 4.2) or water (Figures 4.3 and 4.4). For the calculations we assumed φ_c=0.40 [Mavko et al. 1998]. The contact number (C) was calculated as a function of porosity [Waite et al., 2004; Mavko et al., 1998]:

$$C = 21.62 - 43.76\phi + 25.98\phi^2 \quad (5.13)$$

The theoretical data are shown in comparison with measured velocities for THF and CH_4 hydrate-bearing Ottawa Sand. In the following, model data predicted by the

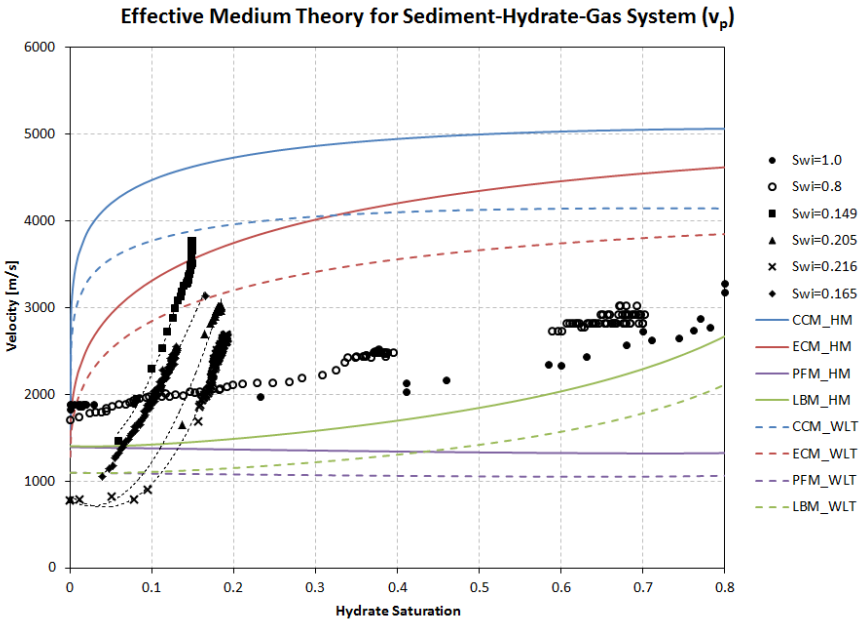

Figure 4.1: P-wave velocities measured and calculated with the Effective Medium Theory for a sediment-hydrate-gas system (solid and dotted lines represent theoretical curves obtained using Hertz-Mindlin and Walton Contact model, respectively)

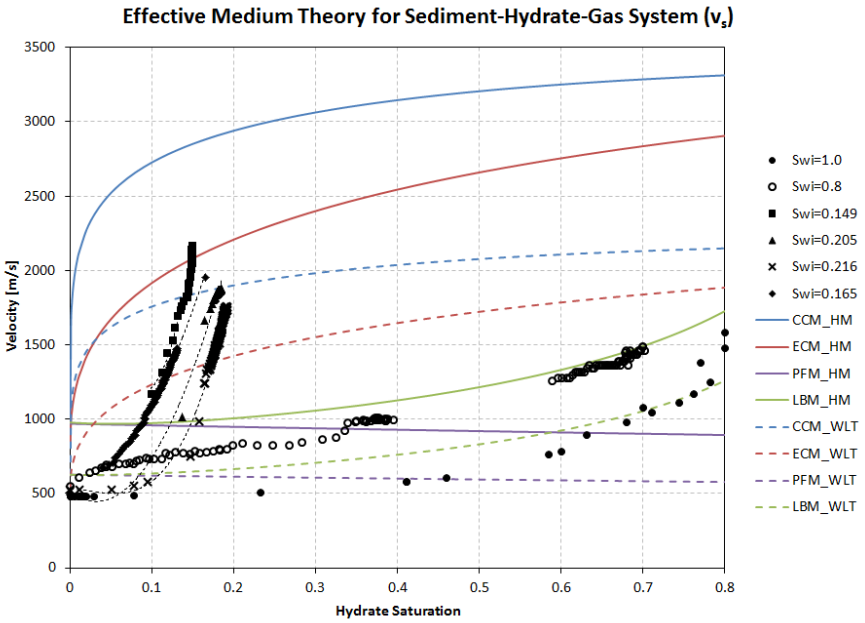

Figure 4.2: S-wave velocities measured and calculated with the Effective Medium Theory for a sediment-hydrate-gas system (solid and dotted lines represent theoretical curves obtained using Hertz-Mindlin and Walton Contact model, respectively)

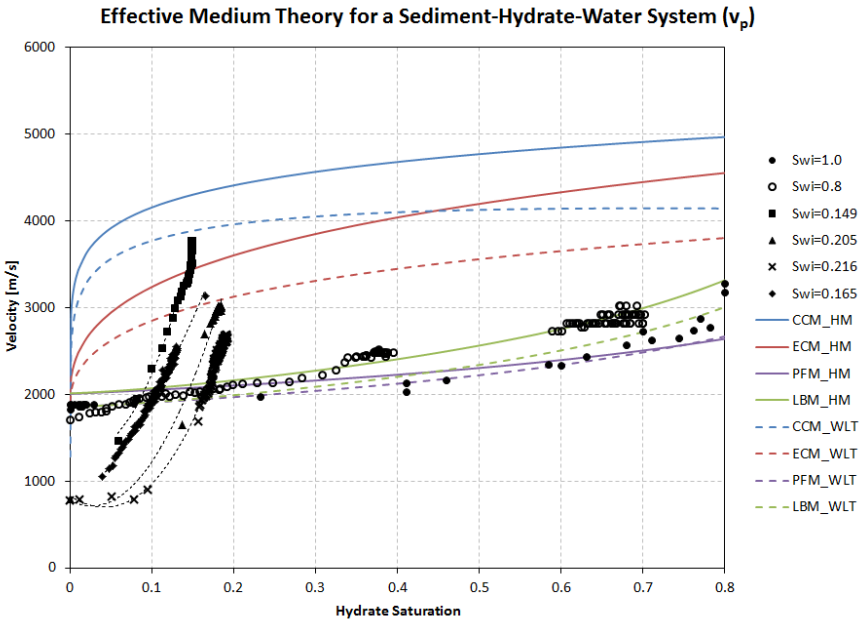

Figure 4.3: P-wave velocities measured and calculated with the Effective Medium Theory for a sediment-hydrate-water system (solid and dotted lines represent theoretical curves obtained using Hertz-Mindlin and Walton Contact model, respectively)

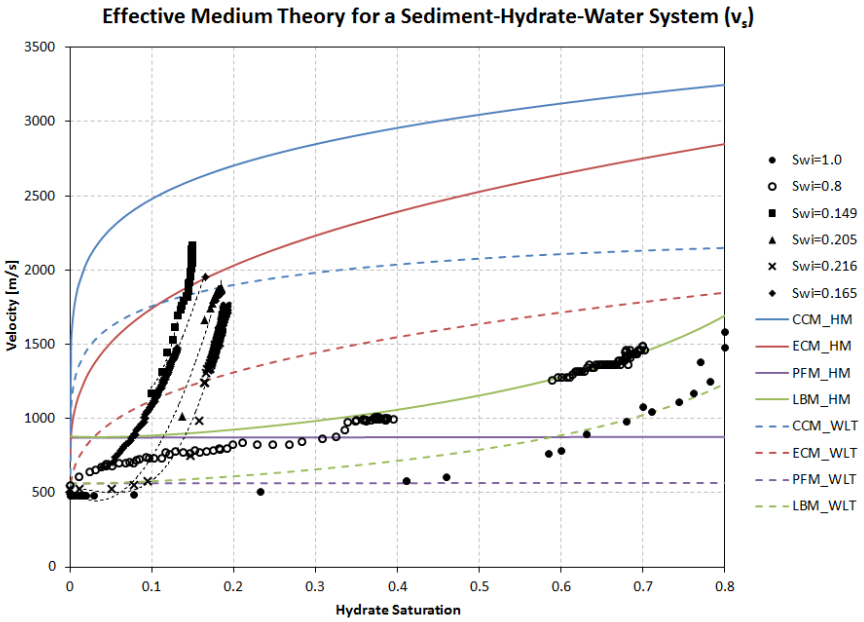

Figure 4.4: S-wave velocities measured and calculated with the Effective Medium Theory for a sediment-hydrate-water system (solid and dotted lines represent theoretical curves obtained using Hertz-Mindlin and Walton Contact model, respectively)

effective medium theories using Hertz-Mindlin or Walton model are referred to as EMT_HM or EMT_WLT, respectively.

For sand samples formed with high initial water saturations (S_{wi}) or containing THF-H_2O solution, the EMT_WLT for a fully water-saturated system best estimates v_p and v_s measured prior to hydrate formation ($v_{p,0}$ and $v_{s,0}$). For sand samples formed with low S_{wi}, EMT_WLT for a fully gas-saturated system provides the best estimate $v_{p,0}$ and $v_{s,0}$. However, the model overestimated both velocities by 100-250 m/s.

For THF hydrate-bearing sediment, v_p and v_s measured with decreasing/ increasing S_h followed the pore-filling model of EMT_WLT at saturations below 50% and the load-bearing model of EMT_WLT above. These results indicate that at low S_h, THF hydrate floated freely in the pore space but acted as a frame-supporting part of the mineral matrix at high S_h. Even after the transition from pore-filling to load-bearing, sediment and hydrate particles remained unconsolidated, allowing slip and rotation of individual grains.

For high-S_{wi}, CH_4 samples, the measured v_p and v_s initially followed the load-bearing model of EMT_WLT but began trending toward the load-bearing model of EMT_HM when S_h exceeded 2%, eventually converging with the EMT-HM curve above S_h = 60%. This result indicates that while sediment particles were initially able to rotate and slip, the presence of high-S_{wi} hydrate prevented further grain movement. In either arrangement, hydrate acted as a load-bearing component in the sediment.

We showed in Chapter 3 that for low-S_{wi} samples, velocity-S_h trends measured during hydrate formation behave differently from those observed for individual specimens that had already reached their individual peak saturation. As the EMT was

developed for the latter case, it is not surprising that that none of the theoretical EMT captured the evolution of v_p and v_s during the formation of CH_4 hydrate in sediment with low S_{wi}.

Only one of the low-S_{wi} samples reached full conversion while hydrate formation was observed (S_{wi}=0.149). The velocities recorded for the fully converted sample fell between theoretical values calculated using the envelope-cementing and the contact-cementing model of EMT_HM. This observation could mean that CH_4 hydrates in low-S_{wi} samples form as a mixture of envelope and grain-contact cement.

4.3.2 Lee's Weighted Equation

We used Lee's weighted equation (LWE) to calculate v_p for varying cementation exponents (n). First, the weighting factor (W) was adjusted to match $v_{p,0}$ with n=1. Figures 4.5 and 4.6 show the resulting v_p curves in comparison with laboratory-velocity data for high-S_{wi} and THF hydrate-bearing samples. v_p recorded for THF hydrate-bearing Ottawa sand follows the v_p-curve calculated using Wood's equation for unconsolidated particles in suspension. Similar to the proposition of the EMT pore-filling and load-bearing model, this observation suggested that THF hydrate is generally disconnected from the grains at lower saturations. v_p recorded for CH_4 hydrate-bearing Ottawa sand with high S_{wi} cuts across the theoretical v_p curves calculated for various n (Figure 4.7). As can be seen, n decreases with increasing hydrate saturation. We considered this behavior somewhat counter-intuitive as it suggested that hydrate becomes less cementing as more water is converted into hydrate. This could be the case if hydrate grew away from the grains into the pore space. Nevertheless, applying

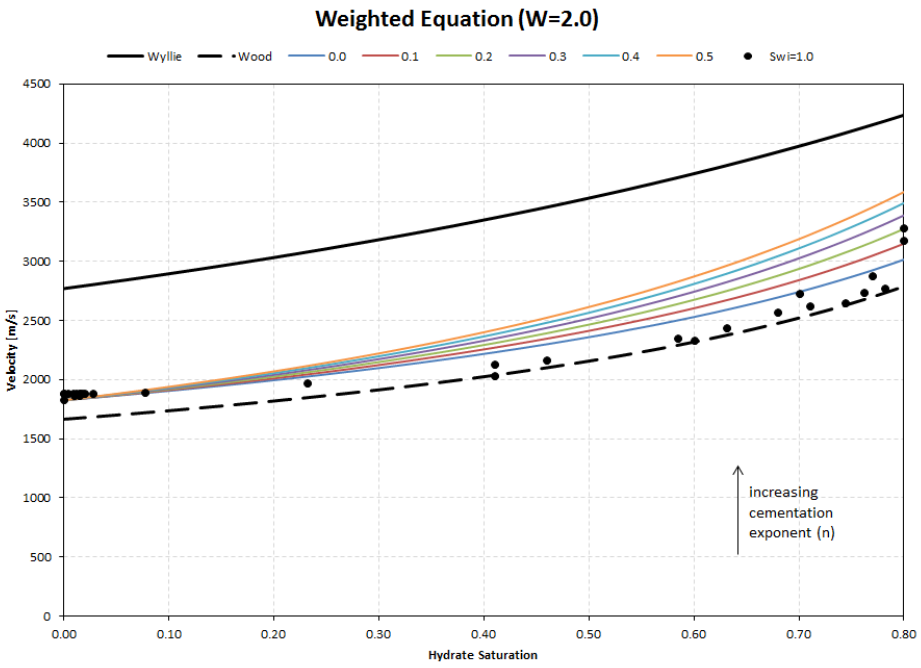

Figure 4.5: P-wave velocities calculated with the Weighted Equation by Lee [1996] (W=2.0) in comparison with laboratory data measured of Ottawa Sand with THF hydrates.

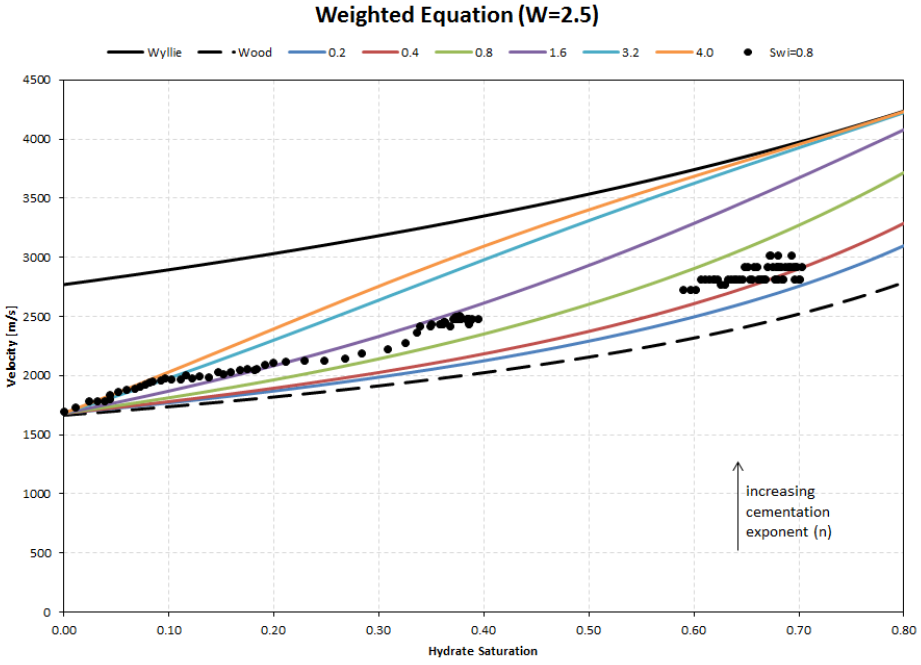

Figure 4.6: P-wave velocities calculated with the Weighted Equation by Lee [1996] (W=2.5) in comparison with laboratory data measured on Ottawa Sand with CH_4 hydrates formed from free gas with a high initial water saturation of $S_{wi} \approx 0.8$

the S_h-dependent n to LWE provides a satisfactory match between measured v_p and theoretical curves for hydrate formation in high-S_{wi} sand samples (Figure 4.8).

4.3.3 Three-Phase Biot Theory

The three-phase Biot theory (TPBT) failed to predict both $v_{p,0}$ and $v_{s,0}$ and the calculated v_p-curves must be shifted by +200 and -350 m/s, respectively, to match the onset velocities. Figures 4.9 and 4.10 show v_p and v_s calculated for a range of ε in the TPBT approach in comparison with laboratory data obtained for THF and CH_4 hydrate-bearing samples with high S_{wi}. In the figure, the model curves have been shifted to match the experimental $v_{p,0}$ and $v_{s,0}$.

Both, v_p and v_s measured during CH_4 hydrate formation in sand with high S_{wi} initially exceed the adjusted theoretical values. As the CH_4 hydrate-bearing sediment neared full conversion, v_p and v_s approached theoretical curves calculated with ε=0. This result seems to confirm what Lee's Weighted equation suggested, namely that the initial CH_4 hydrate weakly cements adjacent sediment grains, but subsequent hydrate growth into the pore space eventually establishes a predominantly load-bearing gas hydrate distribution.

Note that matching velocities recorded for CH_4 hydrate-bearing samples with low S_{wi} would require negative ε and to take into account the presence of gas. The TPBT does not account for any type of bonding between hydrate and grains that would strengthen the sediment beyond load-bearing capabilities.

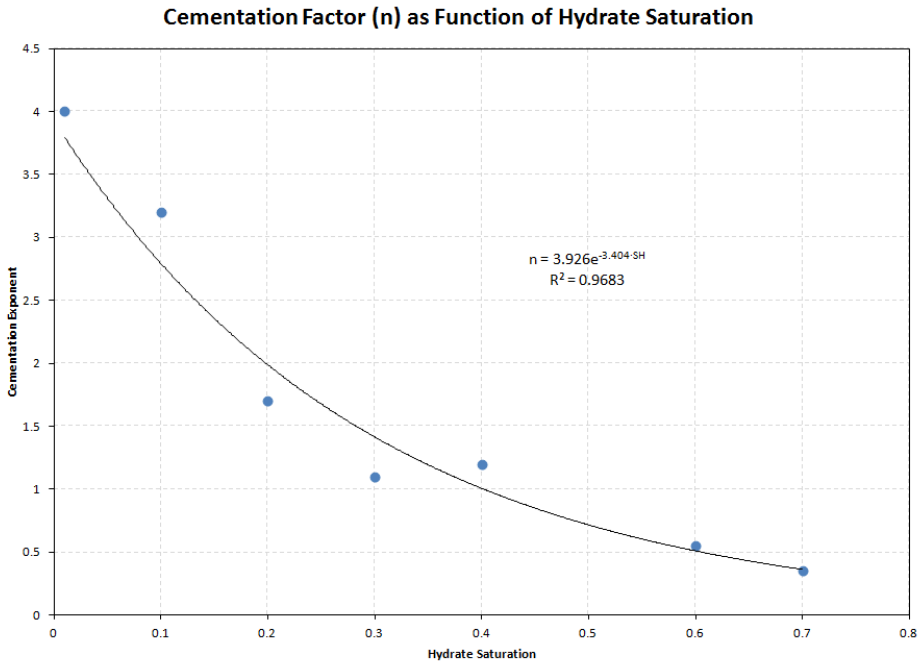

Figure 4.7: Cementation factor for high-S_{wi} sample as a function of gas hydrate saturation. As hydrate continues to grow in the pore space consolidation of the sediment increases (n decreases).

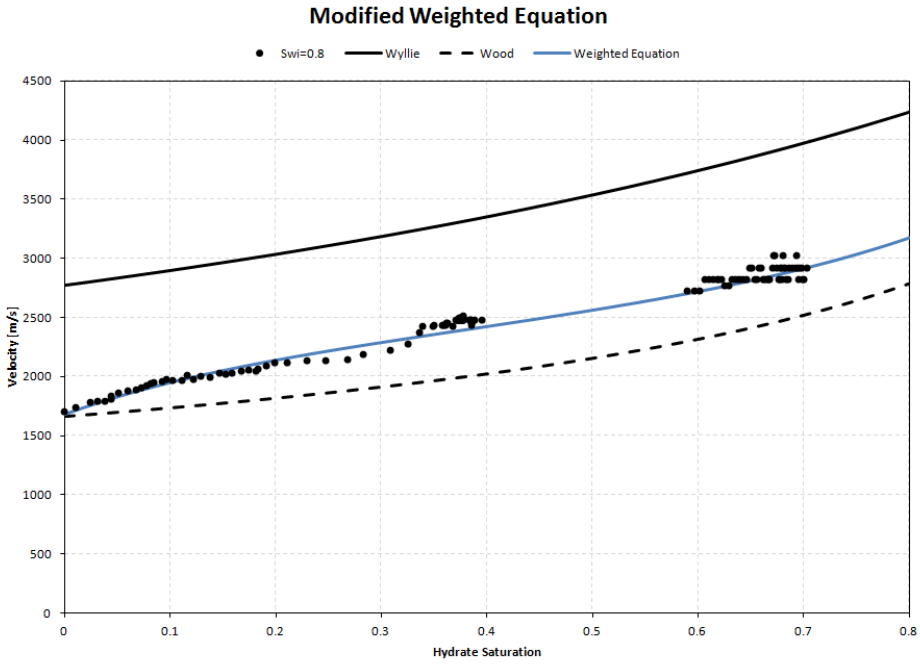

Figure 4.8: Adjusted model for varying cementation exponent with hydrate saturation using the exponential fit of the data in Figure 4.7 (p-wave velocity only).

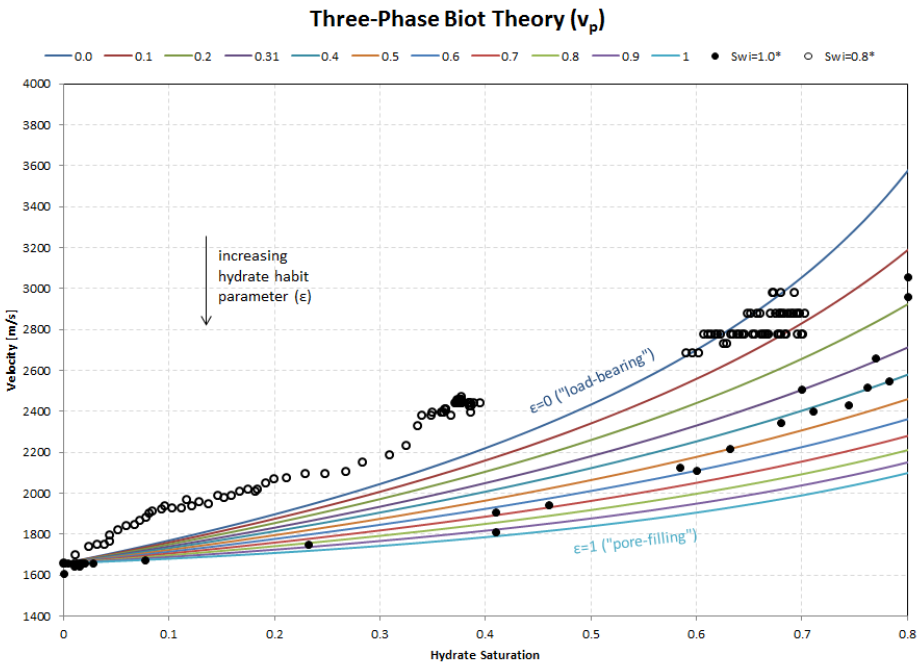

Figure 4.9: P-wave velocities calculated with the Three-Phase Biot Theory for varying ε in comparison with laboratory data measured of Ottawa Sand with high-S_{wi} CH_4 and THF hydrates

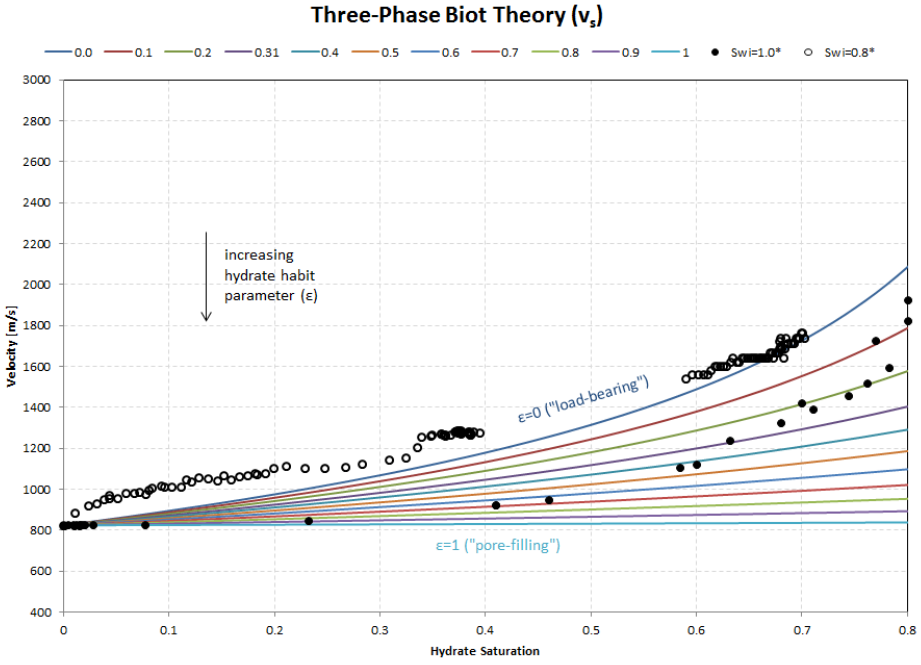

Figure 4.10: S-wave velocities calculated with the Three-Phase Biot Theory for varying ε in comparison with laboratory data measured of Ottawa Sand with high-S_{wi} CH_4 and THF hydrates

The predicted velocities for THF hydrate-bearing samples cut through theoretical curves calculated for varying ε. Figure 4.11 shows ε picked as a function of S_h for both v_p and v_s. As the THF hydrate saturation increases, ε decreases, i.e. as additional THF hydrate forms, the hydrate transitions from pore-filling to being frame-supporting. This trend corresponds to behavior suggested by both EMT and Lee's Weighted Equation. Figure 4.12 v_p and v_s calculated with the adjusted model in comparison with the experimental data.

4.3.4 Santamarina's Cemented Soil Model

We were able to match theoretical values of v_p and v_s to the experimental data by adjusting the parameter representing the stress-dependency of v_s (β), by accounting for the presence of gas, and by expressing θ as a function of S_{wi}. Santamarina and Ruppel [2008] experimentally determined that for sand α=80 m/s and β=0.25. We obtain a better overall agreement of our measured and modeled data with β=0.20. This value for the stress-dependency of v_s also corresponds to the one obtained from the stress-dependent velocity measurements presented in Chapter 2.

The presence of gas in the sediment prior to hydrate formation significantly reduces v_p while increasing v_s only minimally. The latter is due to the decrease in overall density. In partially-water saturated sediment, v_p depends on the distribution of gas and water [Helgerud et al., 1999]. At low initial water saturations, capillary pressure forces water into small pores and grain contacts [Lu and Likos, 2004]. The restricted water movement will prevent coalescence of water into larger accumulations, which results in a fairly homogeneous water distribution (Figure 4.13a). If water is evenly distributed in

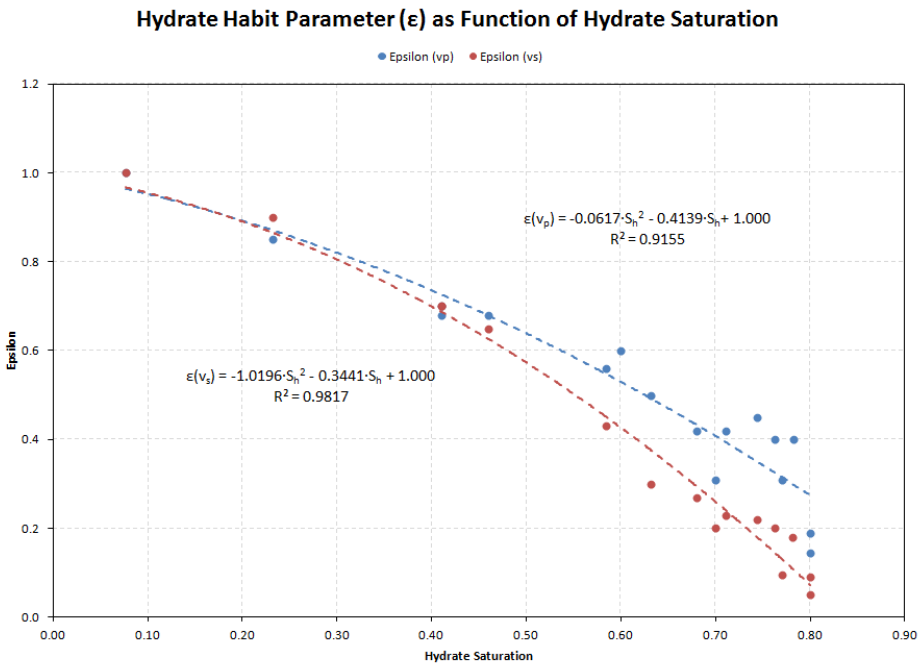

Figure 4.11: The hydrate habit parameter (ε) inherent in the Three-Phase Biot Theory as a function of gas hydrate saturation

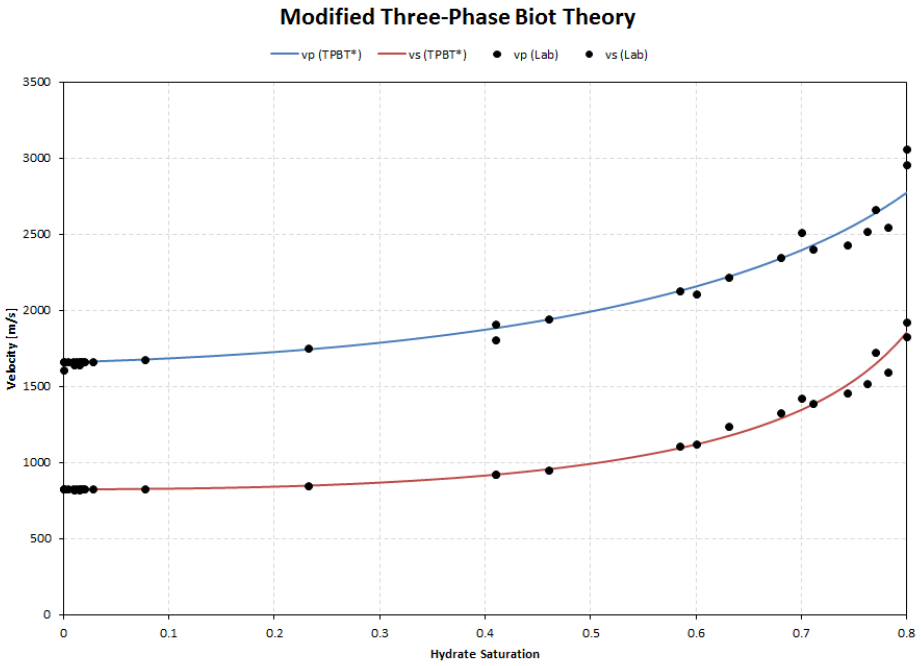

Figure 4.12: Adjusted model for varying hydrate-habit parameter (ε) with THF hydrate saturation using the polynomial fit of the data in Figure 4.11

an excess gas system, the pore-fluid bulk modulus (K_{fl}) can be expressed as the Reuss average of gas and water bulk moduli (K_g, K_w) [Helgerud et al., 2001]:

$$\frac{1}{K_{fl}} = \frac{S_w}{K_w} + \frac{S_g}{K_g} \quad (4.14).$$

As the water saturation increases, the liquid pore fluid will coalesce and accumulate in patches (Figure 5.13b). In the case of a patchy gas-water distribution, Equation 4.15 can be used to calculate an effective bulk modulus (K_{sat}) for the partially-saturated sediment [Dvorkin and Nur, 1998]:

$$\frac{1}{K_{sat}+\frac{4}{3}G} = \frac{S_w}{K_{sat,w}+\frac{4}{3}G} + \frac{S_g}{K_{sat,g}+\frac{4}{3}G} \quad (4.15),$$

where $K_{sat,w}$ and $K_{sat,g}$ represent the bulk moduli for gas hydrate-bearing sediment fully saturated with water and gas, respectively. The shear modulus (G) of sediment is independent of the pore fluid. In both gas-water distributions, the component with the higher compressibility, i.e. the gas, dominates the velocity increase [Schön, 1996] as can be seen in Figure 4.14. As can be seen, velocities begin to increase significantly only at relatively high water saturations (S_w>60% for patchy gas and water, and S_w>90% for an even “Reuss”-type water distribution). However, ultrasonic velocity data of partially water-saturated sediment measured in this and previous studies [Batzle et al. 2006] showed a stronger increase in velocities at lower S_w than predicted by Equations 4.14 and 4.15 (Figure 4.14). Using the Voigt average of K_w and K_g to calculate K_{fl}

provided a better match of modeled of measured velocities of sediments with high S_w (Figure 4.14). The Voigt average of K_w and K_g can be expressed as

$$K_{fl} = S_w K_w + S_g K_g \tag{4.16}$$

and describes a system with evenly distributed gas and water, where the increase in velocity is affected more strongly by phase with the lowest compressibility, i.e. the water. This may be the case for a partially water saturated system where gas occurs in smaller-than-pore-size bubbles (Figure 4.13c).

We note that the v_p dependence indicated schematically here will be frequency dependent. Batzle et al. [2006] demonstrated that the stiffer patchy saturation behavior can become closer to the Reuss (lower) bound as the frequency is lowered. Hence, separate calibrations may be needed for ultrasonic versus logging versus seismic measurements.

Figure 4.15 shows the best fits for the experimental v_p and v_s data Santamarina's cemented soil model (SCSM) accurately predicted v_p and v_s velocities recorded for THF hydrate-bearing sediment. This was expected as the model had been calibrated using laboratory velocity data for THF hydrate-bearing sand [Yun et al. 2005, Lee et al., 2010]. Based on these measurements, the hydrate-habit parameter Θ was determined to be 0.15. Santamarina and Ruppel [2008, 2010] expected larger values for the hydrate-habit parameter θ when the hydrate was formed in partially-saturated sediment.

We also achieved satisfactory matches between measured and calculated v_p and v_s for low S_{wi}. As predicted by Santamarina and Ruppel [2008, 2010] significantly higher

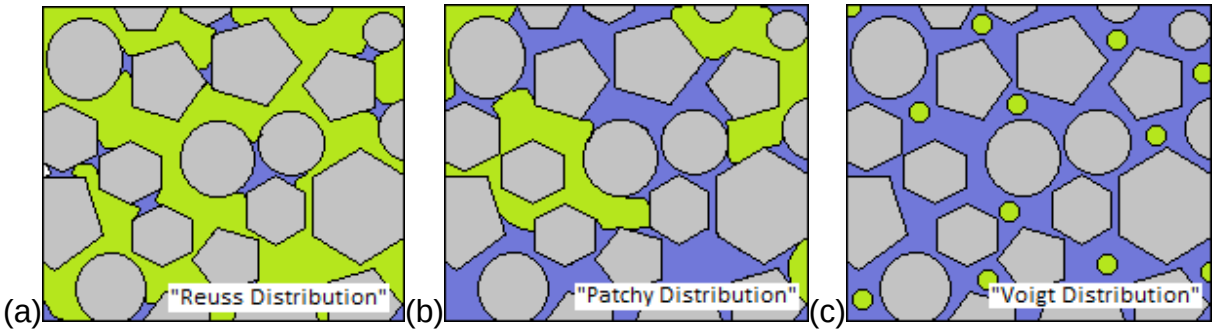

Figure 4.13: Gas-water distributions in sediment (grey, blue, and green areas represent sediment, water and gas, respectively). At low S_{wi} we assume that the water is distributed evenly (a) and K_{fl} can be calculated as the Reuss average of $_{Kw}$ and K_g. At intermediate S_{wi} the gas-water distribution may appear patchy (b). At high S_{wi}, gas may occur in small discrete bubbles (c). In this case K_{fl} can be calculated as the Voigt average of K_w and K_g.

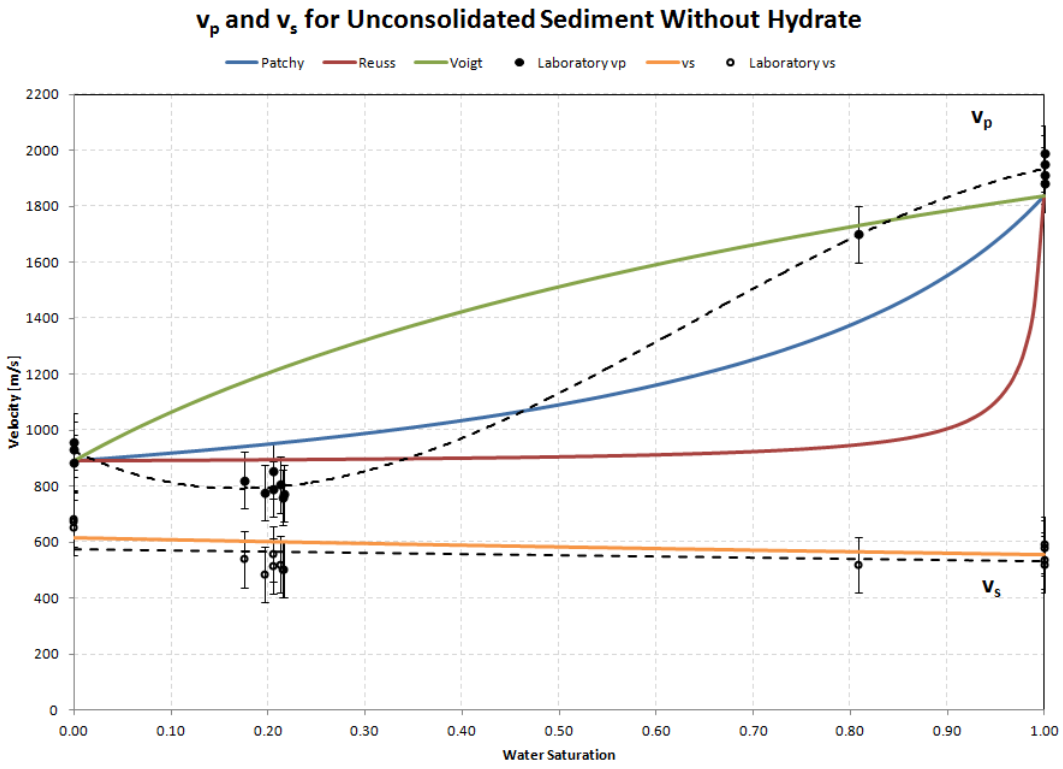

Figure 4.14: v_p and v_s measured and calculated with the Cemented Soil Model proposed by Santamarina and Ruppel [2008] for a hydrate-free sediment-water-gas system as a function of water saturation. (dotted lines is trendline between for v_p and v_s data points)

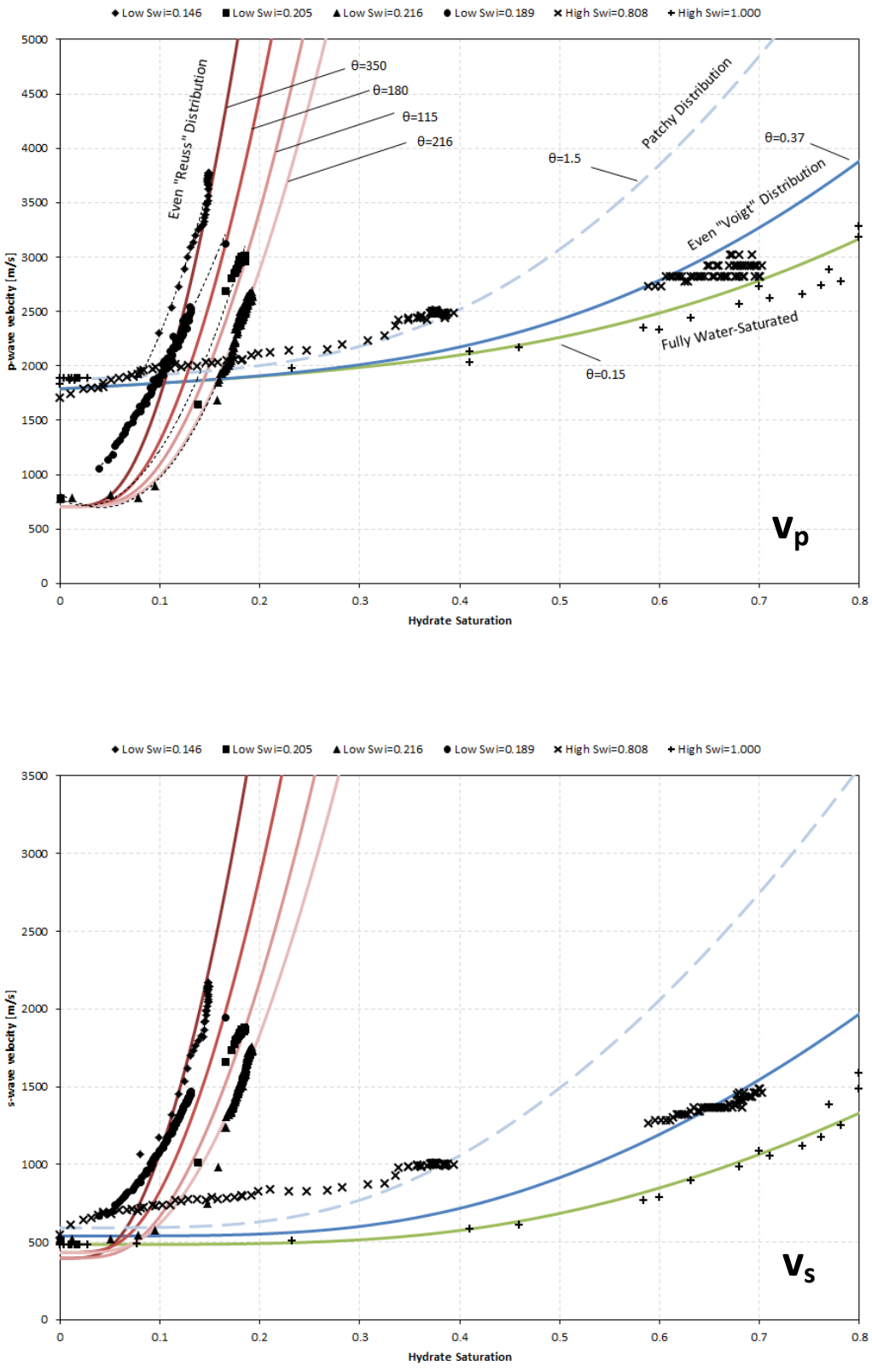

Figure 4.15: Best fits for experimental data and respective fitting parameters, v_p and v_s

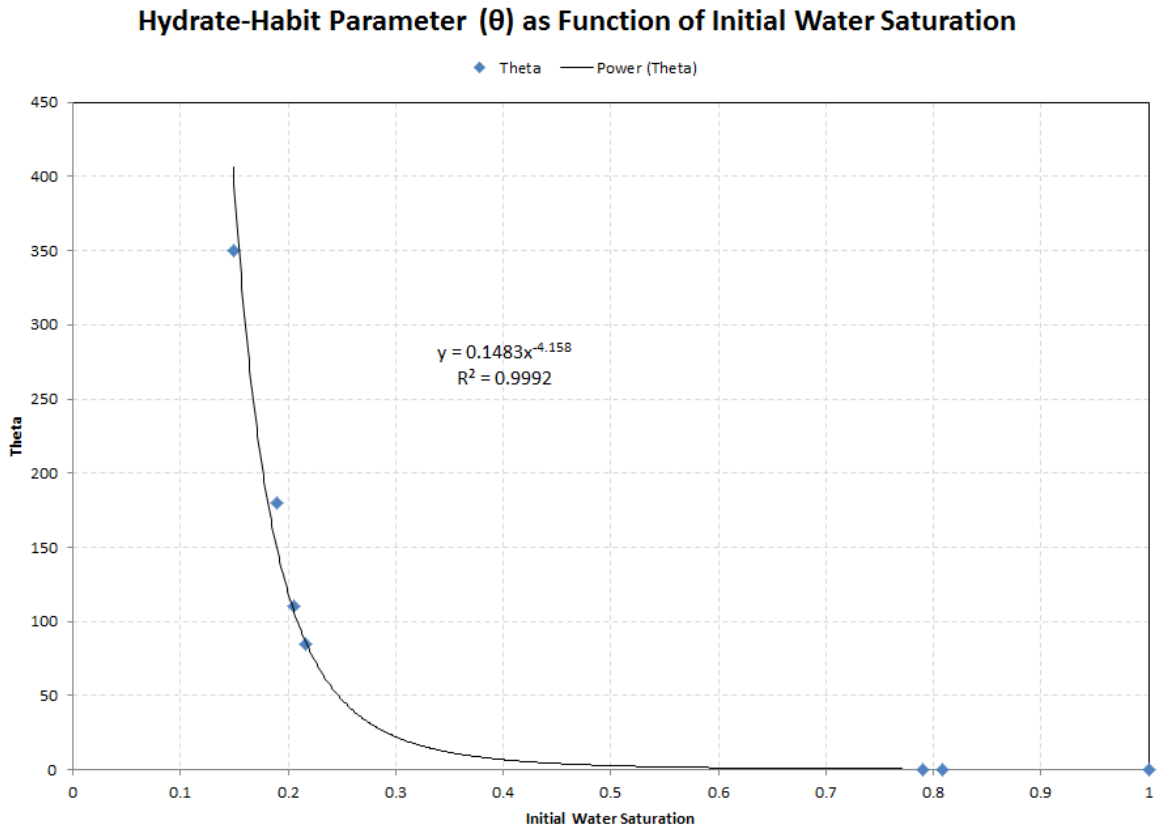

Figure 4.16: Hydrate-habit parameter (θ) inherent in the Cemented Soil Model proposed by Santamarina and Ruppel [2008, 2010] fitted as a function of the initial water saturation

values for θ were necessary to match laboratory and model data. For the four low-S_{wi} samples values, θ ranged between 400 and 150. For the high-S_{wi} samples, θ fell between 1.2 and 0.37. Similar to Lee's Weighted Equation, θ can be also expressed as a function of S_h during the initial hydrate formation and similar to the cementation exponent, θ decreases with increasing Sh. This supports the idea that as hydrate continues to grow, the added hydrate is located such that it is less effective as cement than the hydrate that formed initially.

Figure 4.16 shows the hydrate habit parameter expressed as a function of S_{wi}. The resulting relationship was employed to calculated theoretical curves of v_p and vs over the complete range of S_{wi} (Figures 4.17 and 4.18). Using a S_{wi}-dependent θ and incorporating different gas-water distributions allowed us capture two phenomena observed during hydrate formation in sediment: 1) the decrease in velocity increase with increasing S_{wi}, and 2) the reduction in v_p with decreasing S_{wi} measured prior to hydrate formation. Note that the difference in v_p with gas-water distribution is more pronounced at high S_{wi} and lower amounts of hydrate.

4.4 Summary of Key Observations

Rock physics models for gas hydrate-bearing sediments were reviewed and compared to ultrasonic velocity data obtained from laboratory measurements. The modeling results showed that for each type of hydrate bearing sample, namely THF hydrate-bearing, or CH_4 hydrate bearing with low or high initial water saturation, a separate velocity model had to be used to match the measured v_p and v_s. The fact that each of the models generally described a different hydrate habit, however, supported

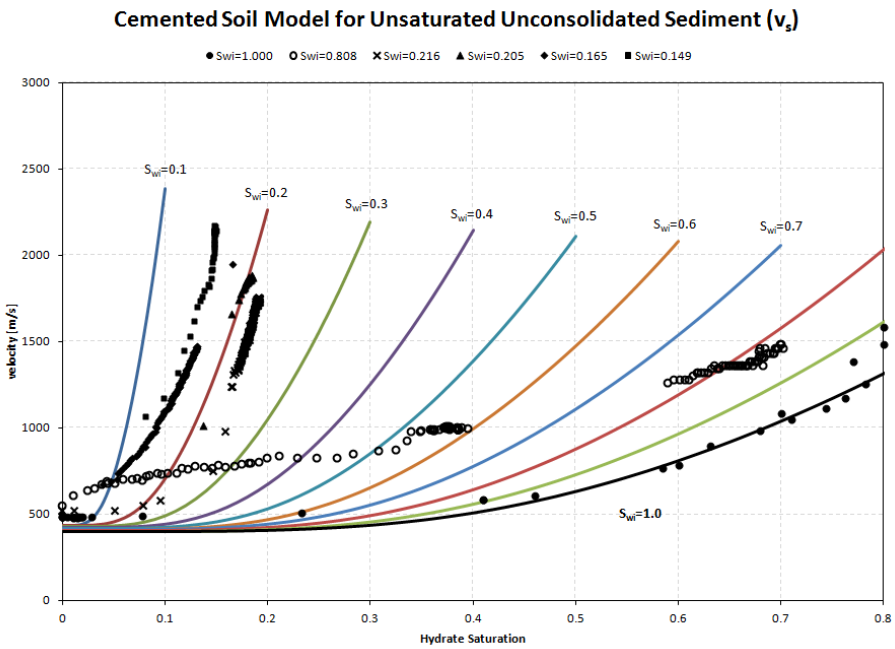

Figure 4.17: Measured v_s of CH_4 and THF hydrate-bearing Ottawa sand in comparison with the Cemented Soil Model-data adjusted using S_{wi}-dependent hydrate habit parameter (θ) for varying S_{wi}

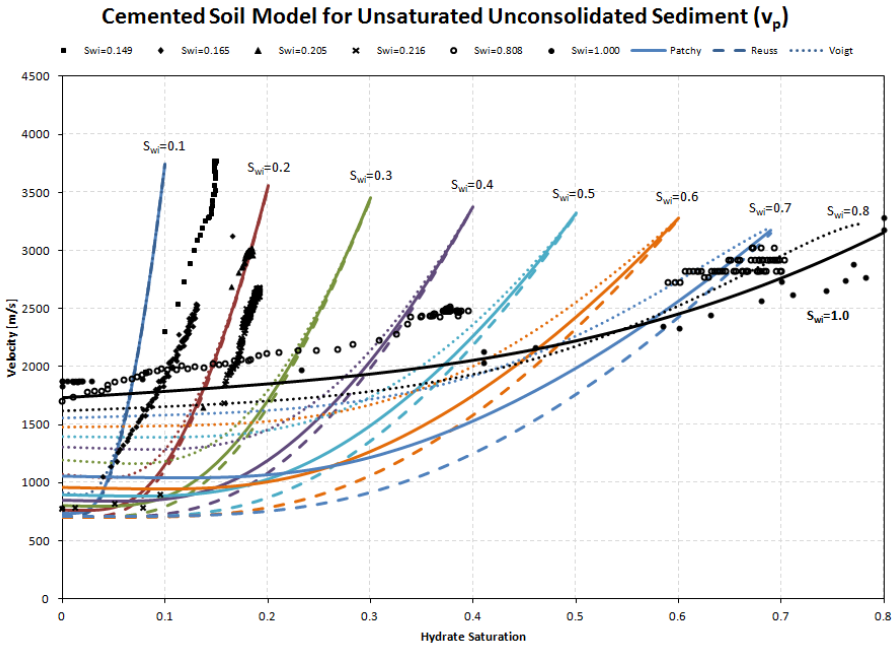

Figure 4.18: v_p measured for THF hydrate-bearing samples and samples containing CH_4 hydrate formed in sand with varying S_{wi}. The measured data is fit by model data obtained using the Cemented Soil Model by Santamarina and Ruppel [2008, 2010] assuming different water-gas distributions.

the hypothesis that different hydrate formation methods resulted in differences in pore-scale distribution of hydrate in sediment. From the comparison of model and measured velocity, the following observations can be made:

Velocities measured of THF hydrate-bearing sand can be matched using the Three-Phase Biot Theory with the hydrate-habit parameter (ε) expressed as a function of S_h. Measured v_p followed the trend predicted by Wood's equation which described particles in suspension. Pore-filling and load-bearing models of the effective medium theory employing the Walton contact model (grains slip and rotate) agreed well with v_p and v_s measured for S_h below and above about 40%, respectively.

For CH_4 hydrate formation in partially water-saturated specimens with high S_{wi}, Lee's weighted matched the measured v_p when the cementation exponent (n) was fitted as a function of S_h. With increasing S_h, n decreased. Similarly, the hydrate-habit parameter in Santamarina's cemented soil model decreased with increasing S_h. Also, the measured v_p and v_s initially exceeded values predicted for load-bearing hydrate by the Three-Phase Biot but eventually converged with the theoretical curve for ε=0 (load-bearing hydrate). The load-bearing model of the effective medium theory employing the Hertz-Mindlin (no slip or rotation of grains) fit the experimental data best at S_h>20-30%.

v_p and v_s measured for low-S_{wi} samples increased exponentially during hydrate formation and approached the cementing model velocity estimates of the effective medium theory. Velocities measured for the fully converted sample fell between theoretical curves for enveloping and grain-contact cementing hydrate suggesting a mix of both hydrate morphologies had formed. The measured velocities exceeded theoretical curves of both three-phase Biot Theory and Lee's Weighted Equation.

Adjusting Santamarina's Cemented Soil Model allowed v_p and v_s to be modeled as functions of S_{wi} for different distributions of gas and water within the sediment. Low-S_{wi} data best agreed with v_p and v_s calculated assuming a homogeneous "Reuss"-type gas-water distribution and high θ (>100). High S_{wi}-data best matched v_p and v_s calculated assuming a homogeneous "Voigt"-type gas-water distribution and low θ (≤1).

4.5 Conclusions

The experimental velocity data was collected during hydrate formation or dissociation in sediment. The models, however, generally, described three-phase systems of sediment, hydrate, and either water or gas, i.e. systems where hydrate formation was complete (final product). Nevertheless, the comparison of measured and model data suggested possible scenarios for hydrate formation in sediment depending on the method of hydrate synthesis that will be tested in Chapter 5 via magnetic resonance imaging and micro-computed tomography:

Comparison of model velocities and velocities measured for THF hydrate-bearing sediment suggest that THF hydrate begins to form in the pore center and where it floats freely in the pore water until a critical hydrate saturation is exceeded. At higher S_h, hydrate formation gradually transitions from pore-filling to load-bearing. Nevertheless, according to the models even at higher S_h, sediment grains and hydrate particles would still be allowed to slip and rotate. The matrix component may even behave as a suspension.

In partially-water saturated sediment, the initial water saturation (S_{wi}) determines the gas-water distribution in the sediment and consequently the location of initial hydrate formation. At low S_{wi}, the water is evenly distributed and the resulting hydrate

cements the grains. At higher S_{wi}, gas occurs in form of patches or bubbles within the pore space. The resulting hydrate particles would be load-bearing and, but do not allow grains to slip or rotate. Initially, hydrates may even partially cement the grains. It is likely that at intermediate S_{wi} gas and water occur as patches resulting in a mixture of load-bearing and cementing hydrate.

CHAPTER 5

MICRO X-RAY COMPUTED TOMOGRAPHY OF TETRAHYDROFURAN AND CYCLOPENTANE HYDRATE-BEARING GLASS BEADS

The pore scale distribution of tetrahydrofuran (THF) and cyclopentane (CP) hydrates in packs of 0.5-mm glass beads were imaged at sub-zero temperatures using micro-focus X-ray computed tomography (MXCT). THF hydrate forms from a single-phase solution, whereas CP hydrate forms from two separate liquid phases. The THF hydrates were synthesized from a THF-H_2O-$BaCl_2$ solution yielding a hydrate saturation of 80%. $BaCl_2$ was added to the mixture to enhance the image contrast between hydrate and pore fluid. MXCT images acquired of the frozen THF hydrate-bearing specimen showed that $BaCl_2$-bearing pore fluid occurred at the grain contacts and THF hydrate was located away from grains. In the CP hydrate-bearing specimen, CP hydrate and the frozen residual pore water mainly occurred where water had been located prior to hydrate formation. To establish how the initial water distribution depends on the water saturation, MXCT imagery was collected in a glass-bead pack over a range of water saturations. At low saturations, water collected at grain contacts or bridged neighboring glass beads, while air/gas represents the continuous phase. At high saturations, water occurred as a continuous phase with air/gas present in the form of bubbles or patches. At intermediate water saturations, water occurred as the continuous phase in some parts of the samples, while air/gas formed the continuous phase in other locations.

5.1 Introduction

In Chapter 4, comparison between laboratory and modeled data suggested that the initial water saturation determines the gas-water distribution in the sediment and consequently the location of initial hydrate formation. We concluded that at low S_{wi} (<20%) the water is evenly distributed and located at the grain contacts. The resulting hydrate cements the grains. At high S_{wi} (>80%) gas occurs as small bubbles inside the pore space. The resulting hydrate particles are load-bearing. At intermediate S_{wi} gas and water were thought to likely occur as large bubbles or patches, resulting in a mixture of load-bearing and cementing hydrate. The model comparison also reinforced our picture of hydrate-formation out of solution, where the hydrate particles do not interact with the sediment until a critical value for S_h is exceeded. In this chapter, we utilize images of partially water-saturated, and hydrate-bearing porous media to test our conclusions presented in Chapter 4 and to gain further insight into how the manner of hydrate formation, as defined by the initial water saturation, affects the pore-scale hydrate distribution in unconsolidated sediment.

Note, that in the following the term “continuous phase” will refer to the spatial distribution of the respective pore fluid and does not refer to its continued availability during the hydrate formation process. We will use the term “bubble” to describe accumulations that are confined to essentially one pore. Thereby, “large bubbles” are those that are approximately the size of the pore and are in contact with the grain surfaces. “Small bubbles”, on the other hand, are disconnected from the surfaces and can float in the pore space. The term “patch” here describes a pore-fluid distribution,

where one phase extends over multiple pore spaces but, on larger scale is isolated by the continuous second phase.

Hydrate formation in porous media has previously been investigated visually [Tohidi et al. (2001); Spangenberg et al., 2008; Jung and Santamarina, 2021], using magnetic resonance imaging [Xue et al., 2010; Zhao et al., 2011], micro-focus synchrotron and X-ray computed tomography (CT) [Jin et al., 2004; 2006; Kerkar et al., 2009]. The results of these studies will be discussed in Section 5.3.

In this chapter, we present micro X-ray CT images of partially water-saturated glass-beads as well as glass beads containing hydrates formed from tetrahydrofuran (THF, C_4H_8O) and cyclopentane (CP, C_5H_{10}). THF is completely miscible in water and THF hydrate forms out of solution whereas CP is immiscible in water and CP hydrate forms from two separate liquids. Both compounds form structure II hydrate and are stable at atmospheric pressure and temperatures above 0°C. We used THF and CP hydrates as proxies for gas hydrate formed from dissolved and free gas, respectively. THF and CP hydrate have served as substitutes for hydrate of natural gases in previous studies [e.g. Bondarev et al., 1996; Lee et al., 2008; Aman et al., 2012].

5.2 Experimental Section

Sections 5.2.1 to 5.2.3 present the experimental details of studies. In the following, we describe sample preparation procedures, hydrate formation methods, and the process for acquiring MXCT images of the THF and CP hydrate-bearing specimen.

5.2.1 Sample Preparation

THF and CP hydrate-bearing specimens were prepared externally prior to the scanning process. The experimental setup used for hydrate formation is shown in Figure 5.1. THF and CP hydrates were formed inside cylindrical 40-mL plastic containers that contained 0.5-mm borosilicate glass-beads (Sigma Aldrich) saturated with the respective hydrate-forming components.

THF hydrates were synthesized from a THF-H_2O-$BaCl_2$ solution. The mixture was composed of 80.75 wt% de-ionized H_2O, 15.0 wt% THF (Sigma Aldrich, ≥99.0 purity, inhibited with 250 ppm BHT), and 4.25 wt% anhydrous $BaCl_2$ (Fisher Scientific, laboratory grade). The fraction of THF in the solution controlled the THF hydrate saturation [Yun et al., 2005]. The THF-H_2O ratio used in this study yielded a THF hydrate saturation of about 83%. $BaCl_2$ was added to the mixture to achieve a better image by increasing the density contrast between the pore fluid and hydrate [Kerkar et al. 2009].

CP hydrates were formed from two immiscible fluids; CP (Sigma Aldrich, reagent grade 98%) and de-ionized H_2O. CP hydrate formation was limited by the amount of water present in the glass-bead pack. Glass beads were mixed with a few drops of water in a plastic bag. The borosilicate glass beads were hydrophilic and water consequently represented the wetting phase in the system. The wet glass beads were filled into the plastic sample containers and frozen at -24°C in a household freezer before being injected with cooled CP (T_{CP}<0°C).

The containers holding the respective saturated glass-bead samples were inserted into an aluminum stand inside an air-tight glass container. For the THF hydrate

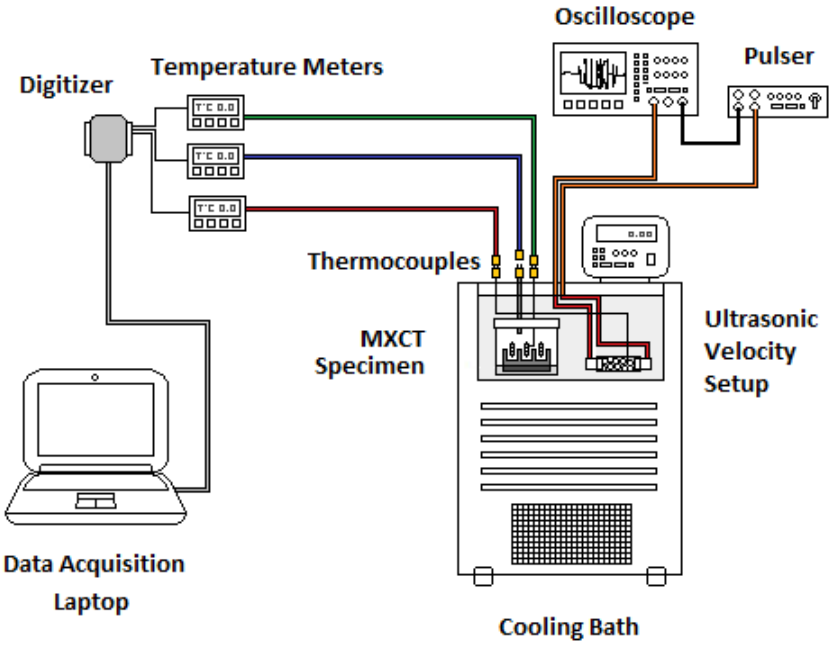

Figure 5.1: Experimental setup used for THF- and cyclopentane-hydrate formation in MXCT samples

samples, the bottom of the glass container was covered with liquid THF. The resulting THF atmosphere prevented the highly fugacious chemical from escaping the samples during an experiment. During CP-hydrate formation, the samples were completely submersed in cooled liquid CP.

Hydrate formation was achieved by cooling the samples into their respective hydrate stability regions using a refrigerated circulation bath (Thomas Scientific). The temperature setup was equipped with two k-type thermocouples. One thermocouple measured the temperature in the glass container (T1). The second thermocouple (T2) was placed inside one of the MXCT samples. As hydrate formation constitutes an exothermic phase transition, an increase in temperature indicated hydrate crystallization.

During hydrate formation, p-wave velocities (v_p) were measured in a separate pack of glass-beads that was placed in the cooling bath alongside the MXCT specimen. The glass-bead pack was saturated with the same THF-$BaCl_2$-H_2O solution used in the MXCT samples. The saturated specimen was enclosed by Tygon tubing and two PEEK endcaps which contained the ultrasonic transducers. The instrumented sample holder confining the sample was similar to the holder used for ultrasonic velocity measurements presented in Chapter 2. A pulser excited one of the transducers, which generated an ultrasonic pulse that propagated through the specimen and was detected by the second transducer. The resulting waveform was recorded with the oscilloscope. Changes in v_p were indicative of phase transitions in the pore fluids. A third thermocouple (T3) measured the temperature in the center of the ultrasonic specimen (THF hydrate-bearing sample only).

5.2.2 Hydrate Formation

The equilibrium temperature of THF hydrate depended on the fraction of THF in the sample [Yun et al., 2005] as well as on the $BaCl_2$ concentration. Based on differential scanning calorimetry measurements (Figure 5.2) it was determined that for the THF-H_2O-$BaCl_2$ mixture at hand, the sample temperature should fall between -3°C and -5.5°C to ensure hydrate stability and avoid the formation of ice. Figure 5.3 shows the temperature profile recorded for THF hydrate-bearing samples alongside the ultrasonic velocities measured. The temperature was decreased from 18°C to 6°C at 1°C every hour, left overnight, and then reduced further to -5°C in increments of 1°C every 90 minutes. A noticeable exothermic temperature peak as well as a significant

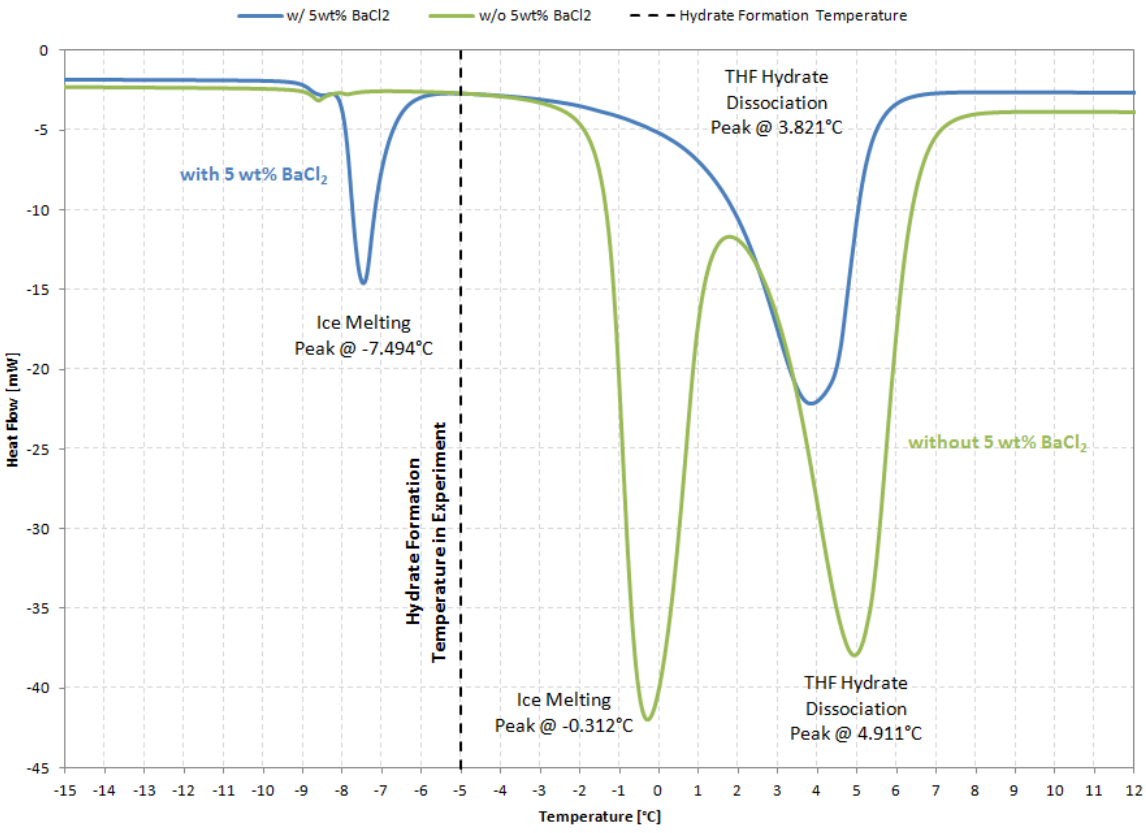

Figure 5.2: Differential Scanning Calorimetry (DSC) curves for THF-H_2O mixture with 4.25 wt% $BaCl_2$ added.

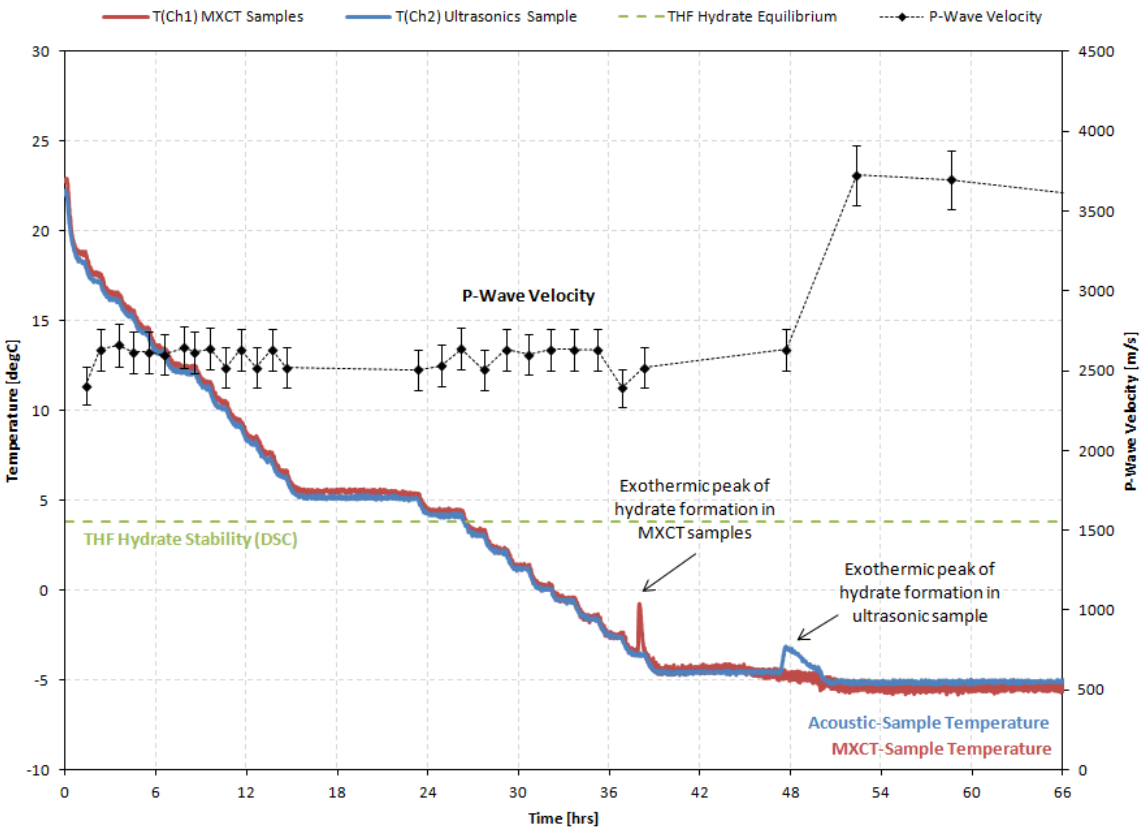

Figure 5.3: Temperature profile and ultrasonic velocities recorded during THF hydrate formation (Note that, v_p reported for THF hydrate-bearing samples in Chapters 2 and 3 are lower than the ones presented here as v_p measured for fluid-saturated packs of glass beads are generally higher than those for fluid-saturated sand [e.g. Spangenberg et al., 2008])

increase in v_p (from 2632 to 3725 m/s) indicated that THF hydrate had crystallized. The THF hydrate-bearing samples remained at this temperature for additional 48 hours. They were then taken out of the cooling bath and immediately quenched in liquid nitrogen to freeze the $BaCl_2$ in place. Previous tests showed that when the THF hydrate-bearing samples were cooled slowly to subzero temperatures, $BaCl_2$ would precipitate from the remaining pore water and THF hydrate and ice could not be distinguished. Prior to being scanned, the THF hydrate-bearing samples were stored in an ultra-low freezer at about -80°C. The storage time of did not exceed 3 days.

CP hydrate is stable up to about 7.8°C [Franks, 1973; Sefidroodi et al., 2013]. The formation of CP hydrates, however, requires a significant amount of sub-cooling [Corak et al., 2011]. To be able to form hydrate from the two liquid phases at temperatures above 0°C, advantage of was taken of the memory effect [e.g. Takeya et al., 2000; Ohmura et al., 2003; Sefidroodi et al., 2013]. Figure 5.4 shows the temperature profile and ultrasonic velocities acquired during CP hydrate formation. The samples were warmed up from -25°C to just above the dissociation temperature of around 8°C. As the temperature exceeded 0°C, ice began to melt and some hydrate formed in its place [Whitman et al., 2008; Zhang et al., 2008]. The p-wave velocity decreased from 3731 to 1667 m/s. At 8°C this hydrate dissociated as indicated by an additional decrease in v_p to 1094 m/s. The specimen was subsequently cooled back down to 1°C. After 15 hours, v_p had increased back to 1670 ms indicating that hydrate had re-formed. The samples remained at 1°C for an additional 4 days before being transferred to the ultra-low freezer. No exothermic peak was observed during hydrate formation. We assume the

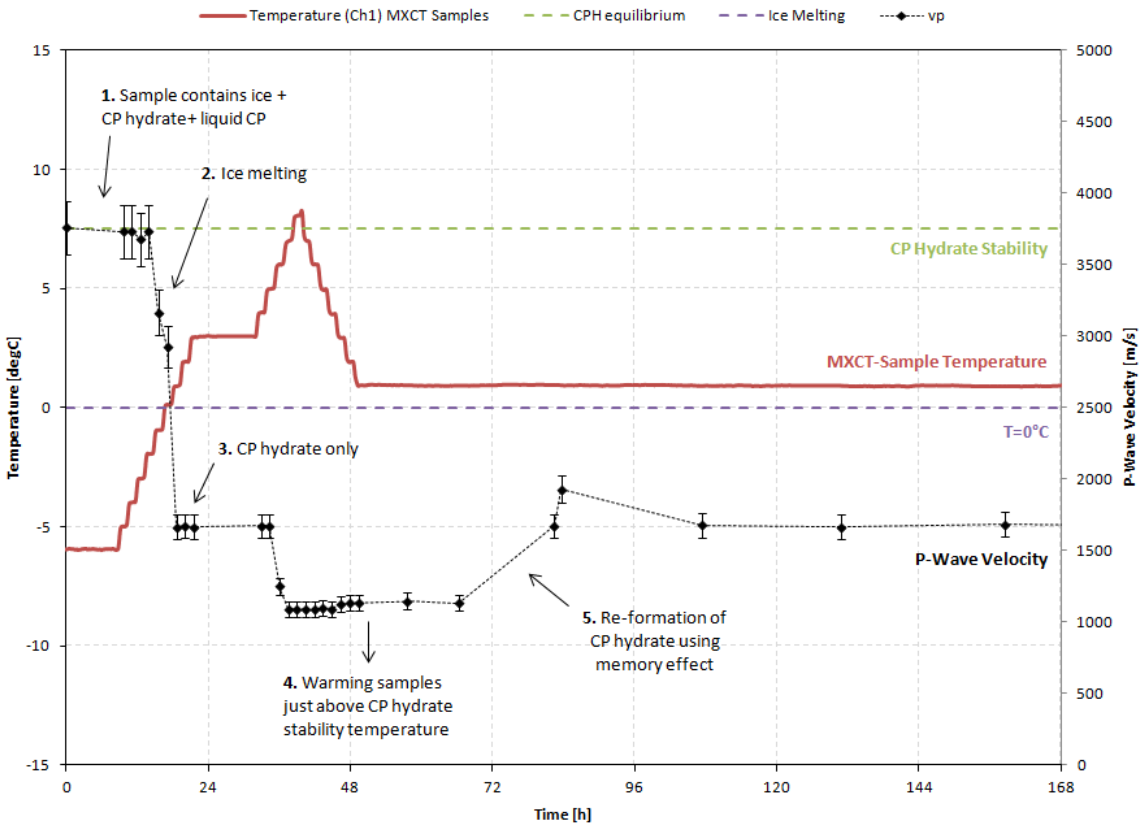

Figure 5.4: Temperature profile and ultrasonic velocities recorded during CP hydrate formation.

amount of hydrate that formed was too small to produce a thermal signature, or that hydrate formed well away from the single thermocouple.

In the test phase of the MXCT sample holder (described in Section 5.2.3), we realized that we had to cool the samples to the lowest possible temperatures prior to placing them into the sample holder to ensure hydrate stability for the duration of at least one scan.

5.2.3 Image Acquisition

Micro X-Ray CT is a non-destructive, three-dimensional micro-scale visualization technique. A number of projection X-ray images are acquired of the sample at different angles and reconstructed computationally into a three-dimensional (3D) representation that maps the x-ray attenuation across the specimen. The X-ray attenuation is closely linked to the density of the sample components [Wildenschild et al., 2002]. We scanned our hydrate-bearing sample with an Xradia µCT-400 scanner. The specimen was placed in a special sample holder that was constructed to enable cooling the top and bottom of the sample with dry ice (Figure 5.5). The sample holder was quickly positioned inside the micro X-ray CT scanner to be scanned. The images were recorded using a charged-coupled device (CCD) camera (pixel size=0.02 mm, area=1200x1200 pixels) in 1° angular increments from -101° to 101° with 500 ms exposure time to the 150 keV X-ray beam. One tomography scan took about 21 minutes. 5-8 tomographies were acquired for each sample to capture the hydrate dissociation. The 202 acquired projection images were reconstructed into a 1014-slice volume using Xradia's in-house reconstruction software. The individual slices were then exported as .tif-image files. We

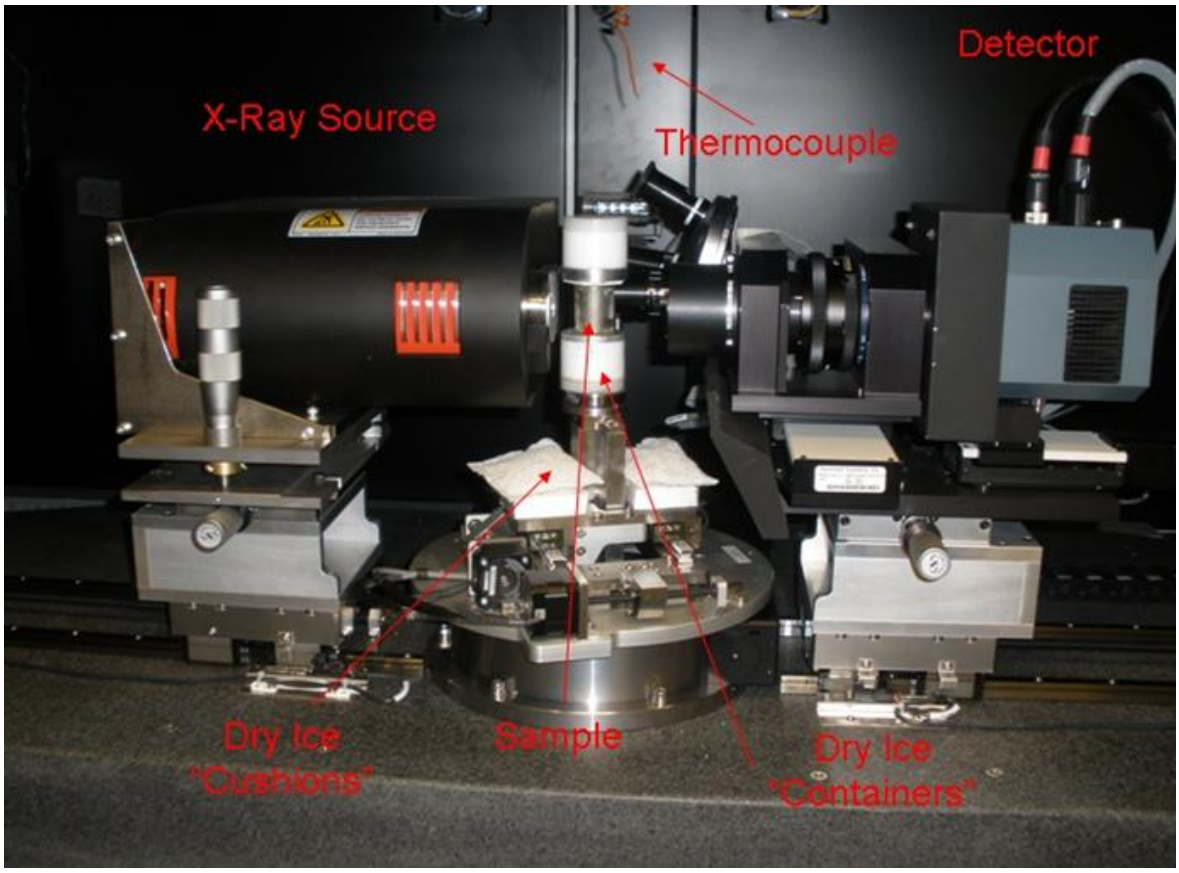

Figure 5.5: Cooled sample holder inside Micro X-Ray CT scanner (sample height = 2 cm).

used Image J, an open-source image processing and analysis software by the U.S. National Institute of Health (www.rsbweb.nih.gov) and the commercial image processing software AVIZO for visualization of the micro X-ray CT image files.

5.3 Results

We acquired MXCT images of a number of THF and CP hydrate-bearing glass-beads specimen. In the following, we show examples for both types of samples and describe and discuss the features observed with respect to the pore-scale distribution of hydrate in the porous medium.

5.3.1 THF Hydrate-Bearing Glass Beads

Figure 5.6 shows micro X-ray CT images acquired of two THF hydrate-bearing glass bead samples before, during, and after hydrate dissociation. Each component of the sample is represented by a different shade of gray in the image. Materials that attenuate X-rays more effectively are depicted in lighter colors than those that adsorb or scatter less beam energy. $BaCl_2$-bearing ice/water is shown in bright white glass beads in light grey, THF hydrate in medium gray, and air in dark grey (see also the more magnified views in Figure 5.7).

Note that, as $BaCl_2$ is excluded from the hydrate structure, and the pore water salinity increases, which suppresses the freezing point of the $BaCl_2$-H_2O solution (Figure 5.2). As the sample temperature was not measured during scanning, it is unclear whether the BaCl2-bearing phase identified in the images was ice or liquid water.

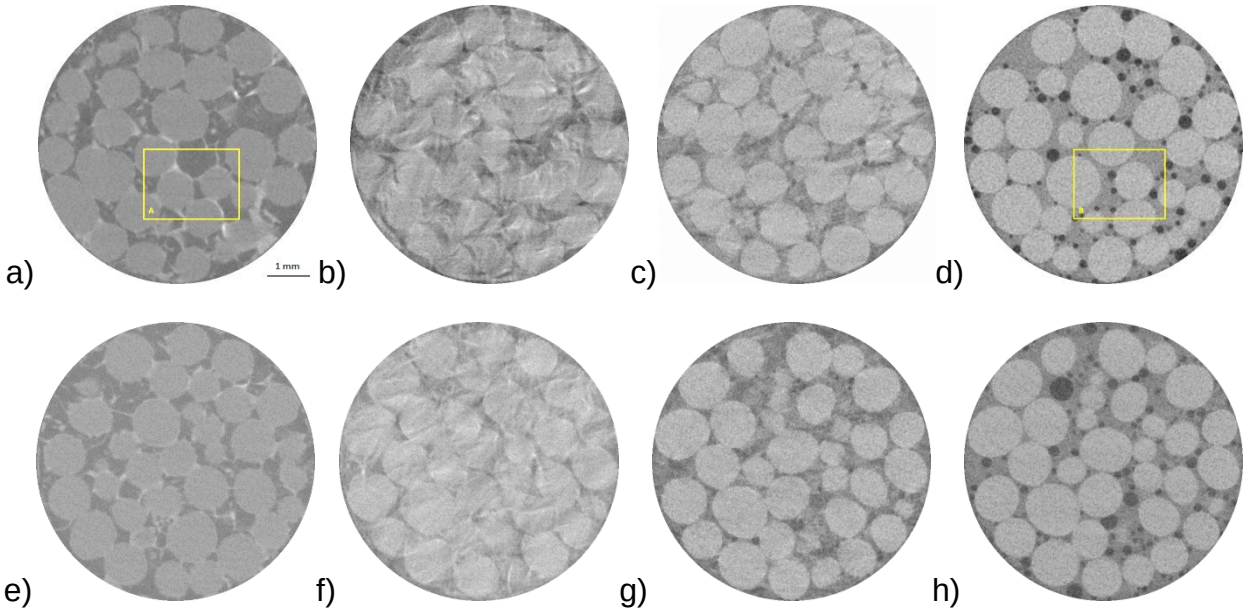

Figure 5.6: Micro X-ray CT images of two THF hydrate-bearing glass-bead Samples 1 (top) and 2 (bottom) during hydrate dissociation: a,e) THF hydrate is frame supporting (after 21 min), b,f) collapse of glass beads (after 42 min), c,g) Mixing of THF-H_2O and H_2O-$BaCl_2$ phases (after 84 min), and d,h) air bubbles within THF-H_2O-$BaCl_2$ solution post hydrate dissociation (after 126 min). The yellow squares indicate the subsections shown in Figure 5.7.

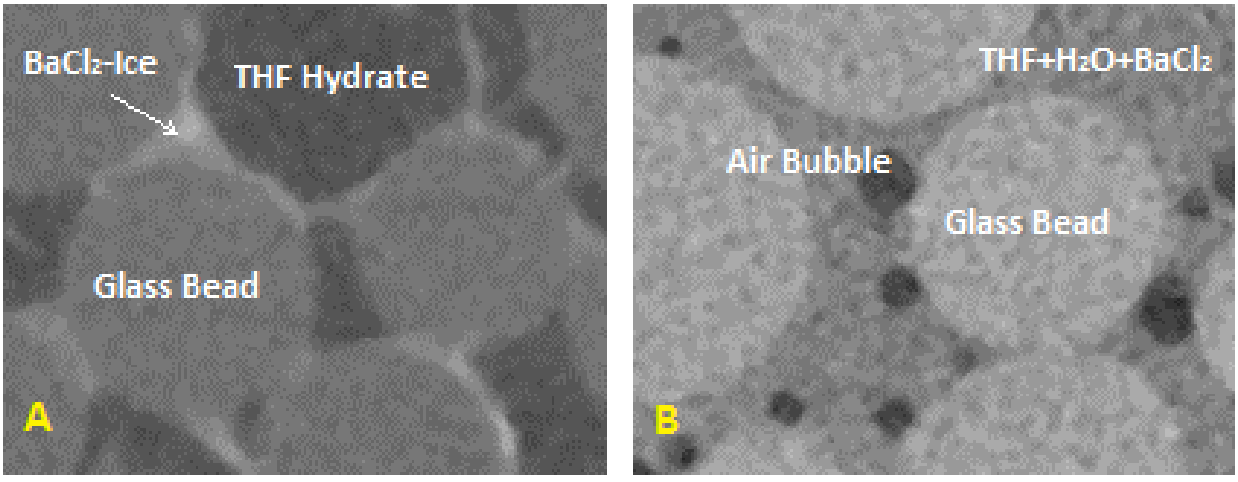

Figure 5.7: Segments of micro X-ray CT images acquired (A) before, and (B) after hydrate dissociation, indicating the areas of $BaCl_2$-bearing H_2O (ρ>2900 kg/m^3), glass beads (ρ=2230 kg/m^3), THF hydrate (ρ≈970 kg/cm^3), THF-H_2O-$BaCl_2$ mixture (ρ=1197 kg/m^3) and air bubbles (ρ≈1 kg/m^3).

During the first scan, the THF hydrate remained stable. THF hydrates were located mostly away from the glass-bead contacts and surfaces. The $BaCl_2$-bearing ice/water was observed primarily at the glass-bead contacts. In many scans, a layer of $BaCl_2$-bearing water was visible between the hydrophilic glass beads and the THF hydrate. During the second scan, THF hydrate decomposed, rearranging and consolidating the glass beads. This glass bead movement during the scan blurred the image (Figure 5.6b,f). In the end (after about 2.5 hours from the onset of hydrate dissociation), THF and water from the hydrates had mixed with the $BaCl_2$-bearing water and equilibrated in a homogeneous solution interspersed by small air bubbles that were previously trapped outside the field of view. Over time the small bubbles coalesced to form bigger bubbles.

Our micro X-ray CT images showed a variety of THF hydrate textures occurring in one sample. Often, THF hydrate occurred as polycrystalline agglomerates with characteristically sharp edges (Figure 5.8a). In other areas of the specimen, THF hydrate appeared to be made up of smaller components with inconsistent shapes (Figure 5.8b). Only in few areas did we observe that THF hydrates occurred as patches that penetrated adjacent pore spaces (Figure 5.8c). Similar textures of THF hydrate were also observed in previous studies. Kerkar et al. [2009] observed in micro X-ray CT scans that THF hydrate nucleated in the pore center away from grain surfaces. The nucleation sites appeared to be random and independent of the pore size. Xue et al. [2012] observed in magnetic resonance images that the location of first crystallization depends on the THF-H_2O ratio of the hydrate-forming solution. At low concentrations of THF, THF hydrate nucleation occurs in the pore center. As the THF-H_2O ratio

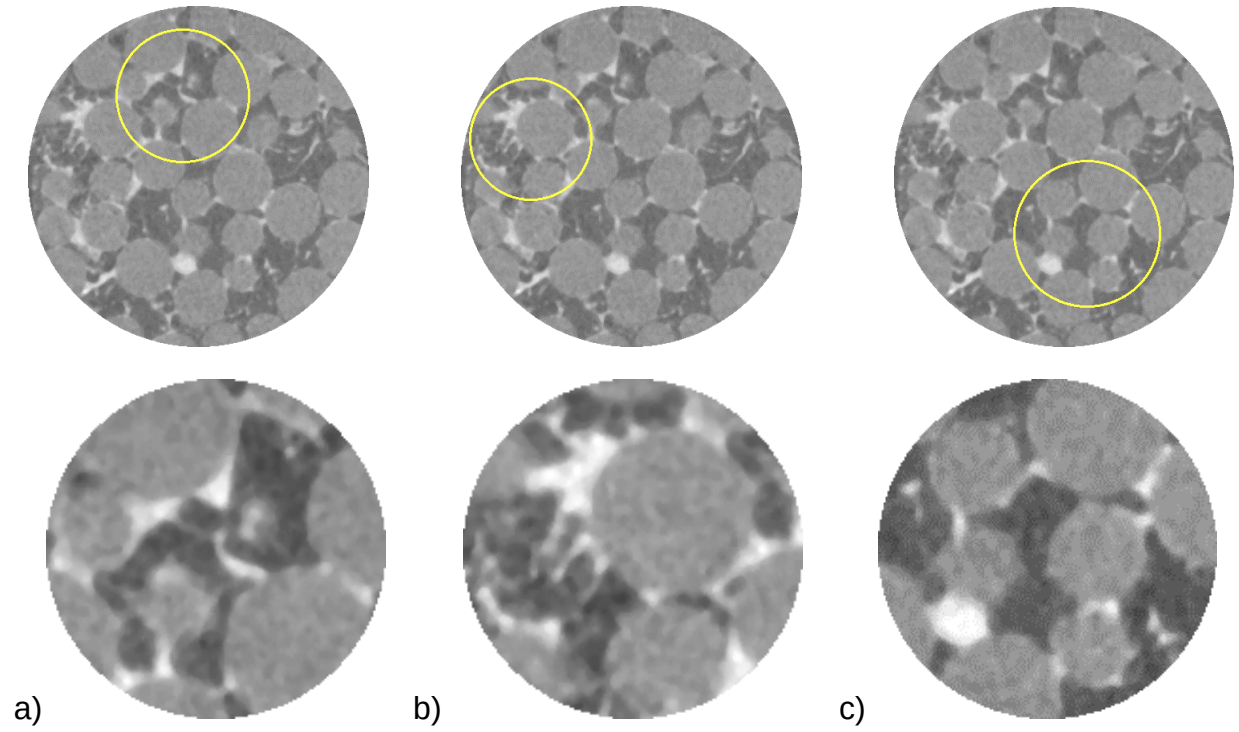

Figure 5.8: THF hydrate morphologies: large single crystals (a), pore-invading hydrate patches (b), and polycrystalline aggregates (c).

approaches the stoichiometric molar ratio of 1:17, THF hydrate nucleation sites migrate towards the grain surfaces. The micro X-ray CT images by Kerkar et al. [2009] showed that THF hydrate continued to grow until it filled the pore space and then penetrated pore throats and neighboring pore spaces. The resulting hydrate accumulations were large, interconnected patches with convexly curved edges. The magnetic resonance images by Xue et al. [2012] showed that, when synthesized from a stoichiometric mixture, THF hydrate formed pore-sized crystals with distinct, angular edges. In solutions with lower THF concentrations, hydrate appeared to be composed of smaller crystals with inconsistent shapes. Visual observation THF hydrate formation in glass micro-models by Tohidi et al. [2001] suggested that THF hydrate initially grew with a

convexly curved growth front which later evolved into angular margins with a hexagonal contour.

5.3.2 Cyclopentane Hydrate-Bearing Glass Beads

Micro X-ray CT images of CP hydrate-bearing glass beads are shown in Figure 5.9. The CP hydrate was formed from liquid CP and water. Neither fluid contained any additive for image enhancement ($BaCl_2$ did not dissolved in CP and water was the limiting phase with respect to hydrate formation). Consequently, we were not able to distinguish CP hydrate and water (frozen or unfrozen) in the micro CT images. In addition, the contrast between CP hydrate and liquid CP could not be resolved. However, since CP was a somewhat fugacious substance, it partially evaporated during storage, and the framework of ice and hydrate became partially visible. We used a glass vial filled with water, liquid CP and air as a grey-scale reference (Figure 5.10). The first scan in the series (Figure 5.9) shows the frozen CP-bearing glass-bead pack. During the second scan, glass beads shifted within the sample. It is likely that the ice present in the sample melted which and the glass beads collapsed. The third scan shows that after the collapse, solids are still present in the sample, most likely CP hydrate. Over the course of the following hour (scans d-h) CP dissociated as indicated by the receding CP hydrate surface (marked by the arrow in Figure 5.9). The last scan shows the distribution of the remaining water after CP hydrate dissociation was completed.
In the micro X-ray CT images, the shape of the CP hydrate surface appears to be somewhat uneven but overall corresponds to the outline of what should represent the CP-water interface. For comparison, we imaged partially water-saturated glass beads

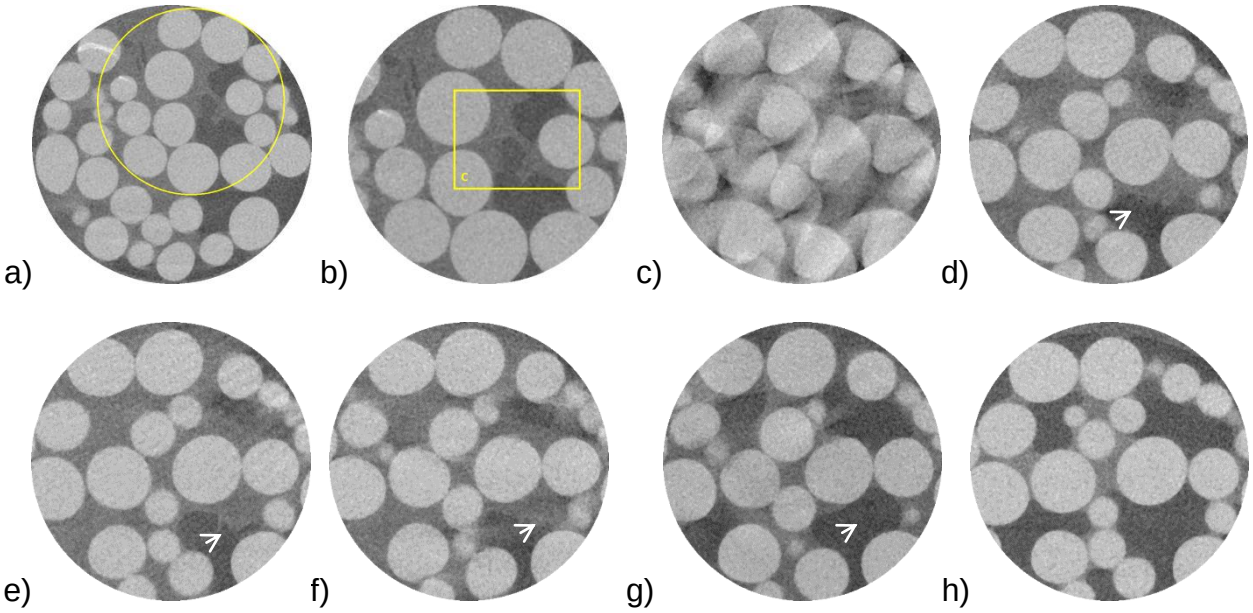

Figure 5.9: Micro X-ray CT images of CP hydrate-bearing glass-bead sample: a) Region imaged in Fig. 5.9 b-f, b) glass beads with CP hydrate, ice, and air (21 min), c) ice melts and glass-bead pack becomes unstable (42 min), d) glass-beads with CP hydrate and water (63 min), e-g) decomposition of CP hydrate (84-126 min), h) glass beads partially saturated with liquid water and patches of air (147 min). The diameter of the image a) is 60 mm (Arrows indicate the retreating dissociation front).

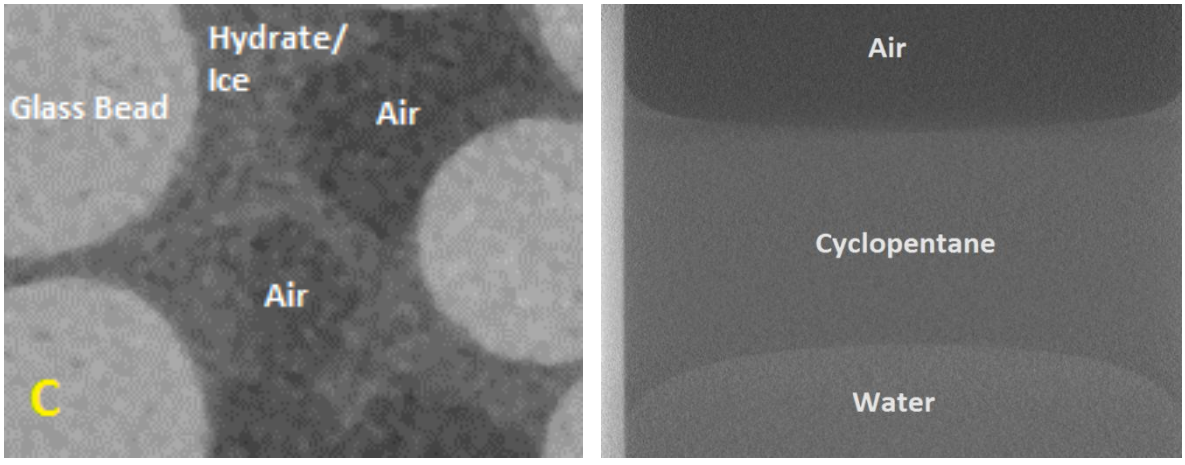

Figure 5.10: Section of a micro X-ray CT image (see Fig. 5.9b) of CP hydrate-bearing glass-bead sample in comparison with an image acquired of water, cyclopentane, and air in a glass container (the container was can be seen as a vertical bar at the left-hand side of the image).

with varying water content and without hydrate (Figure 5.11). The gas (air)-water interface is marked in red in these images. At low saturations (a), the water resided at the glass-bead contacts or bridged adjoining particles, whereas at high saturations (c), the water occurred as a continuous phase with air/gas present in form of bubbles or patches. At intermediate water saturations (b), a patchy mixture of bubbles and bridging occurred.

In a two-phase system of water and hydrate-former, hydrate typically crystallizes at the interface between the two phases [Moon et al., 2003; Taylor, 2007]. Taylor [2007] visually observed hydrate growth in a ~300 μm-diameter water droplet submersed in CP. A thin hydrate shell formed at the water-CP interface after nucleation was initiated. As the water in the droplet further converted into hydrate, depressions developed on the hydrate outer shell giving it an uneven appearance. Sloan & Koh [2008] stated that growth behavior of hydrate in a water droplet was analogous to that at a planar water surface and independent of the type of hydrate former.

Tohidi et al. [2001] and Jung and Santamarina [2012] observed CH_4 formation in the presence of hydrophilic surfaces. In the system studied by Tohidi et al. [2001] CH_4 bubbles within pores and CH_4 patches extending over several pores were surrounded by water. A thin CH_4 hydrate shell initially formed around the CH_4, but then subsequently collapsed, allowing the rest of the gas to be converted. Jung and Santamarina [2012] investigated CH_4 hydrate formation in a water droplet between two hydrophilic surfaces. First, a CH_4 hydrate layer formed on the meniscus, the hydrate shell then ruptured and water leaked out of the meniscus. CH_4 hydrate continued to grow into the water in lobe-like shapes. In both studies the resulting hydrate

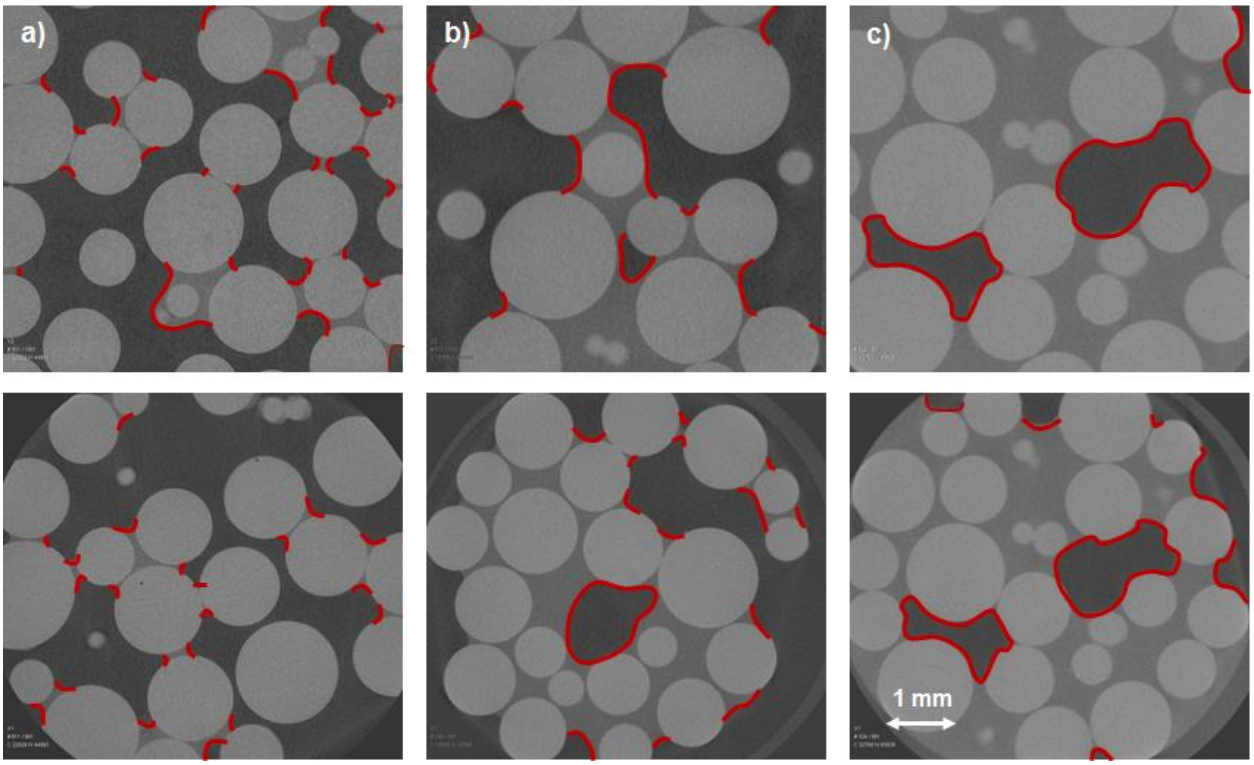

Figure 5.11: Micro X-ray CT images of partially saturated glass beads with a) low, b) intermediate, and c) high initial water saturation. The red lines mark the air-water interface between the dark-grey gas phase and the lighter-grey water phase. Light circles are glass beads. The red lines indicate the nucleation front locations during hydrate formation in a free-gas phase methane and water system

demonstrated a fragmented appearance that was also visible in micro X-ray CT images of CH_4 hydrate-bearing sediment presented by Jin et al. [2006] but was not visible in our images.

5.4 Summary of Key Observations

We presented micro X-ray CT images of THF and CP hydrate-bearing packs of glass-beads. Micro X-ray CT is a useful tool to analyze the pore-scale structure of hydrate-bearing porous media. However, additives are required to enhance the image contrast between hydrate and the liquid pore fills, and atmospheric pressure hydrate formation is required to avoid a thick-walled pressure chamber and allow the MXCT scanner to be located close to the specimen surface for maximum resolution. Using THF and CP allows for atmospheric-pressure formation of gas hydrate from the dissolved phase (THF + water) or separate phases with hydrate formation at the interface (CP is not miscible in water).

- At low saturations, water occurred at grain contacts or as bridges connecting adjacent glass beads. At high saturations, water was continuous and air/gas occurred as bubbles within individual pores or as multi-pore air/gas patches. At intermediate saturations, a mixture of both fluid distributions was observed.
- The distribution of ice and CP hydrate in the glass-bead pack appeared to mimic the location of the pore water and CP prior to freezing and initiating hydrate formation in the sample. The solid interface between the ice/CP hydrate and the air bubbles that formed in place of liquid CP that had evaporated away appeared less smooth than the air/gas-water interface in partially water saturated samples.

- In the fully-saturated THF + water system, which included $BaCl_2$ in the water for imaging purposes, we observed that the $BaCl_2$-H_2O solution was generally located at the grain contacts. THF hydrate, on the other hand, appeared to be located away from the grains contacts and surface. Often a thin layer of $BaCl_2$-H_2O was observed surrounding the glass beads.

The MXCT images support the results obtained from the comparison of measured and modeled velocity data presented in the previous chapter. They underline the importance of the initial water saturation on the distribution of hydrate in the pore space of sediment. As the water saturation increases, the water-gas distributions transitions from a spatially continuous gas phase, to patchy gas and water, to a spatially continuous water phase. As the gas-water interface, which represents the location of initial hydrate formation, moves away from the grain contacts, the hydrate becomes less effective as a cementing agent and transitions from cementing, to load-bearing, to pore-filling. In the following chapter, the results presented in Chapters 3-5 will be brought together and synthesized into a conceptual model of how the initial water saturation determines the pore-scale distribution of the hydrate which, in turn, determines the ultrasonic velocities of the unconsolidated sediment.

CHAPTER 6

CONCEPTUAL MODEL OF HYDRATE FORMATION IN SAND

The objective of this PhD thesis was to investigate the effect of hydrate formation on the pore-scale hydrate distribution and the subsequent effect on the wave velocities of unconsolidated sediment. Previous studies on hydrate-bearing sediments primarily focused on one of two hydrate formation mechanisms: a) hydrate formation from a free gas phase in partially water-saturated sediment [e.g. Waite et al., 2004; Jin et al., 2006; Ebinuma et al., 2008; Priest et al., 2005; 2009] and b) gas hydrates formed out of solution [e.g. Tohidi et al., 2001; Yun et al., 2005; Spangenberg et al., 2008; Lee et al., 2010]. Based on pore-scale models by Ecker et al. [1998] and Helgerud et al. [2001], the resulting gas hydrate-bearing sediments were generally classified with respect to their elastic properties either as cementing, in the case of formation in the presence of excess gas, or as pore-filling/load-bearing in the case of hydrate formation in systems with excess water or dissolved-phase hydrate formers.

This pore-scale classification of hydrate morphologies is linked to quite significant differences between morphologies in terms of elastic properties. For example, cementing hydrate increases p- and s-wave velocities dramatically even when very little hydrate forms, while pore-filling/load-bearing hydrate has very little impact on wave velocity through the sediment until the hydrate saturation exceeds ~50% of the pore space. Until now, these two gas hydrate distributions have generally been treated as being completely distinct and unrelated with respect to their pore-scale distribution and

elastic properties. The results of this thesis showed how cementing- and pore-filling/load-bearing hydrate distributions represent end members of a continuous spectrum of hydrate morphologies, all of which are linked by the initial water saturation present in the sediment prior to hydrate formation.

This chapter presents a conceptual model that relates the initial water saturation and hydrate formation mechanism to the resulting pore-scale hydrate distribution and the net effect on the wave velocities thorugh hydrate-bearing sediment (Figure 6.1). The model has been developed based on the research presented in the previous chapters in this thesis, bringing together results from our ultrasonic velocity measurements (Chapter 3), model comparison studies (Chapter 4) and micro X-ray computed tomography images (Chapter 5).

When hydrate forms from a free gas phase, growth initiates at the gas water interface [Moon et al., 2003; Taylor et al., 2007]. The locations of those interfaces depend on the pore-water distribution, which, in turn, depends on the initial water saturation in the sample. As the water content increases from low saturations to full saturation, water transitions from being evenly distributed and located at the grain contacts, to occurring in patches in areas of smaller pores, to being the continuous phase surrounding gas accumulations, to saturating the entire pore volume. The mechanics by which this water-distribution spectrum impacts hydrate growth and the resulting wave velocities, is summarized in Figure 6.1 and described below.

At low initial water saturations, water collects at the grain contacts or forms bridges linking adjacent grains (left column in Figure 6.1). Capillary and adhesive forces prevent coalescence of water into larger accumulations, ensuring an essentially

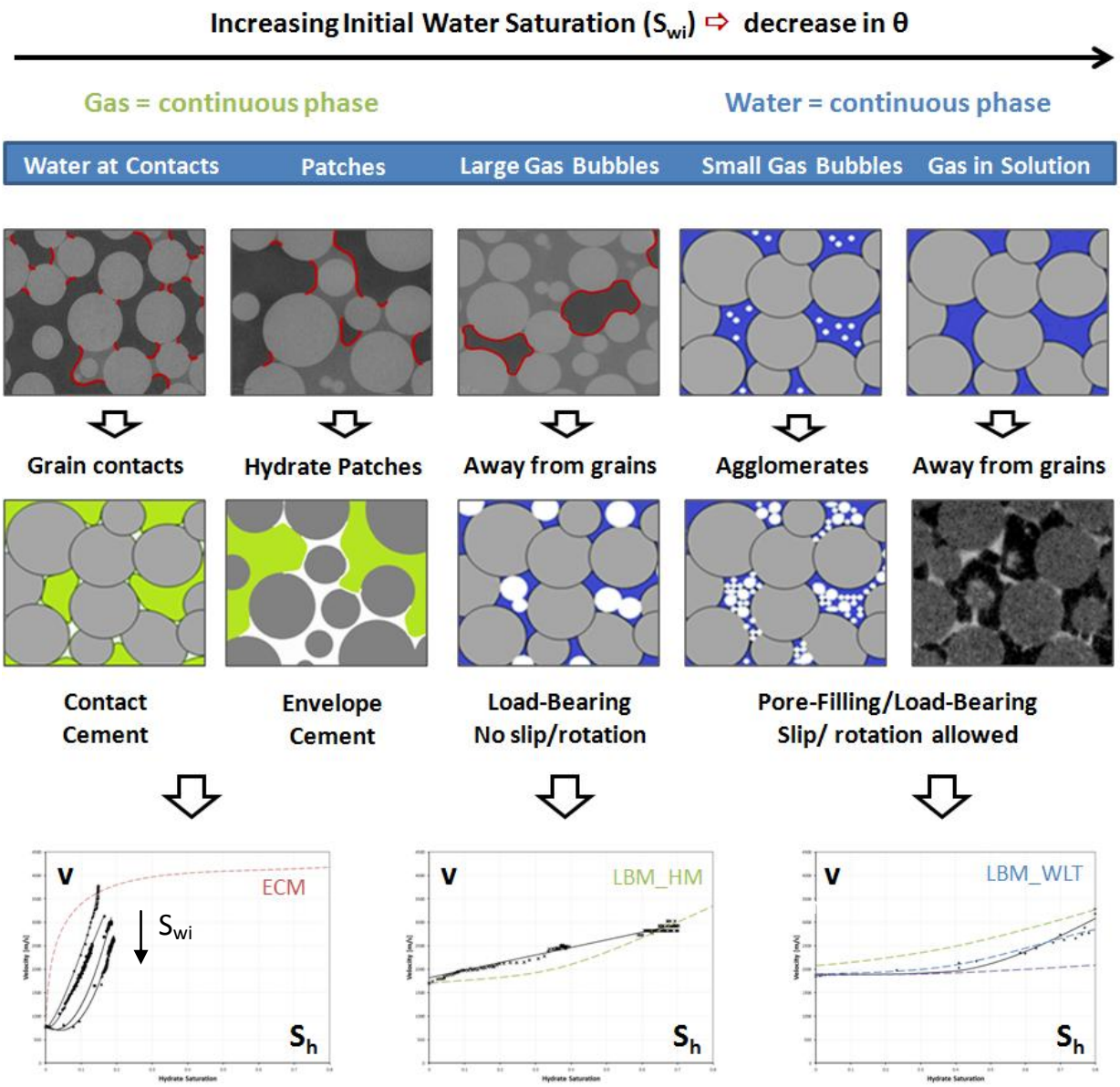

Figure 6.1: Conceptual model of hydrate formation in coarse, unconsolidated sediment. In the drawings, grey, white, blue, and green areas represent the sediment grains, hydrate, water, and gas, respectively. In the MXCT images in the top row, light, medium, and dark grey areas represent glass bead, water, and air, respectively. Red lines indicate the gas-water interfaces and areas of initial hydrate formation. In the MXCT image in the bottom row, white and black areas represent water and hydrate, respectively. The dotted lines are representative of the models of the effective medium theory: envelope-cementing model (ECM, red line), load-bearing model using the Hertz-Mindlin contact theory (LBM_HM, green line), the load-bearing model using Walton's contact theory (LBM_WLT, blue line), pore-filling model (purple line). Black lines serve only to guide the eye and connect data from individual datasets.

homogeneous water distribution throughout the sample. When subjected to suitable hydrate formation conditions, hydrate starts forming at the gas-water interface and then grows into the water phase [Taylor et al., 2007]. The resulting hydrate cements grains at the contacts in which it forms, causing a dramatic increase in bulk and shear stiffness of the sediment. The more water is converted to hydrate, the closer the hydrate front moves towards the grain contact's center and the more effectively hydrate can act as cement (Figure 6.2).

While hydrate is forming, v_p and v_s increase exponentially with increasing hydrate saturation. When all of the water in the sample is converted to hydrate, wave velocities through the gas hydrate-bearing sediment can best be described by the cementation models of the effective medium theory [Ecker et al., 1998]. The cementation models were developed for three-phase systems of sediment, hydrate and gas, i.e. samples where the water phase has been completely converted into hydrate. In the envelope-cementing model, the hydrate surrounds grains and cements between grains, whereas in the contact-cementing model, the hydrate only exists at the grain contacts. In either cementation model, even sediments with small amounts of hydrate exhibit dramatically elevated velocities compared to samples without hydrate. For a given hydrate saturation, however, the contact-cement model has all of the hydrate acting as an intergranular cement and therefore predicts a higher wave velocity than the envelope-cementing model where hydrate also forms on parts of each grain that do not connect to other grains.

Our experimental results for fully converted samples and those by other authors [Waite et al., 2004; Priest et al., 2005; 2009] agree more with the envelope-cementing

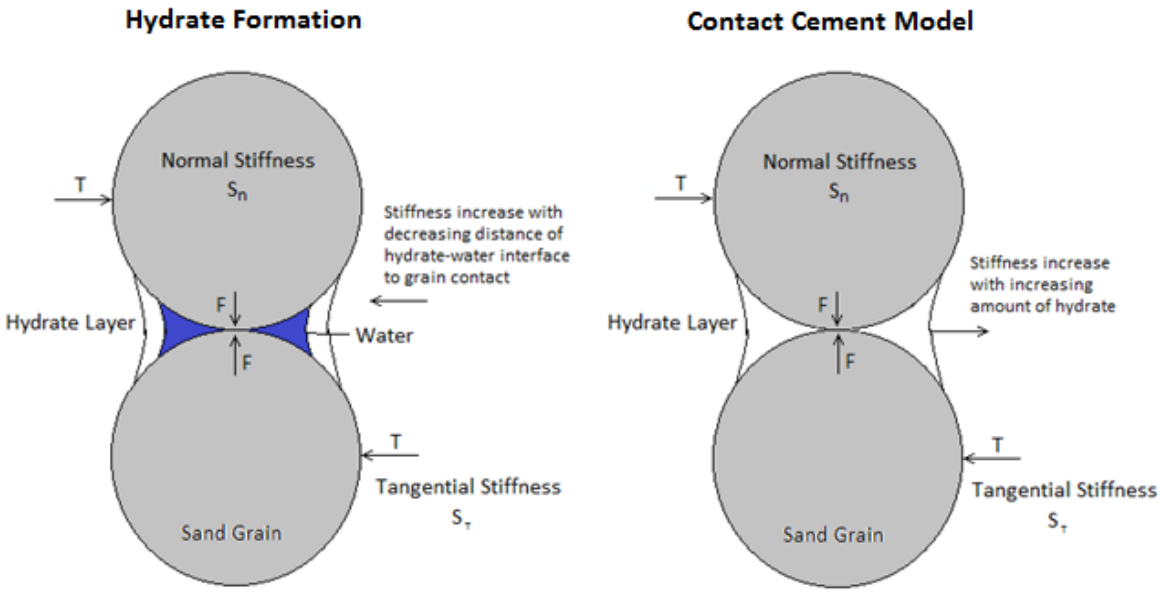

Figure 6.2: a) Effect of hydrate formation in sediment with low initial water content. The higher the initial water saturation the farther away is the stiffening cementing layer and the less effective it is in adding to the tangential stiffness of the two spheres. As hydrate formation continues, the hydrate saturation increases as the hydrate-water interface moves toward the grain contacts where it can act more effectively as a stiffening agent. b) Contact-cementing model of the effective medium theory [Ecker et al., 1998] I which the initial water has completely converted to hydrate.

rather than grain-contact cementing effective medium model. As discussed by Waite et al. [2004], this is understandable considering this type of specimen is generally formed from damp sand, so water is expected to initially coat sediment grains, and will be converted in place into hydrate. However, none of the MXCT showed any evidence of actual coating of grains unless water occurred in patches. Similar to ice, water expands as it converts into hydrate [Lee et al., 2010] and may press apart the grains at the contacts thereby lowering the normal sediment stiffness. This would also explain the collapse and compaction observed in sediment after hydrate dissociation (Chapter 5).

As the initial water saturation increases, the gas-water interface moves farther away from the grain contacts (Figure 6.2a) and the intergranular cementation due to hydrate formation becomes gradually less effective. At higher water saturations, more water has to be converted to achieve the same degree of stiffening as was observed for lower water saturations. Consequently, the rate at which velocity increases with increasing S_h during hydrate formation slows with increasing initial water saturation. As the initial water saturation increases to the point where water becomes mobile, water will coalesce and accumulate as bigger patches (second column from the left in Figure 6.1) in areas with smaller pore sizes (Figure 6.3a). After hydrate formation is completed, fully hydrate-saturated zones will alternate with zone of no hydrate (Figure 6.3b). The impact of patchy hydrate of this type is not as significant as cementing hydrate, but velocities in the hydrate-bearing sand will be higher than in the load-bearing case [Dai et al., 2011]. Averaging the velocities for sediment with this type of hydrate (Figure 6.3c) may provide a first good approximation for the overall velocity.

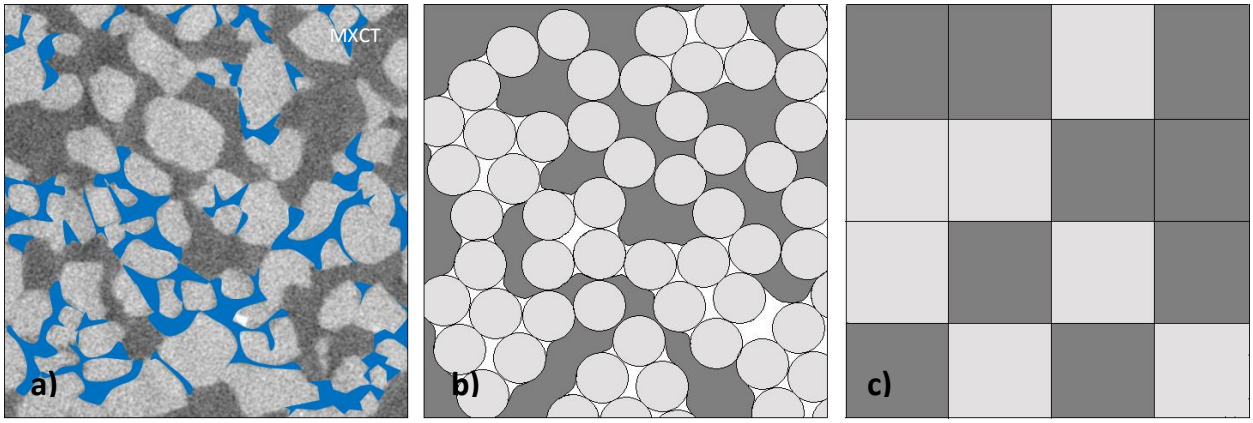

Figure 6.3: Hydrate formation in sediments with a patchy water saturation. Blue, light grey, dark grey, and white areas in a) and b) represent water, sand grains, gas/air, and hydrate, respectively. Water initially forms in clusters of smaller pores (a), such that when water has converted into hydrate, fully hydrate-saturated zones will alternate with zone of no hydrate (b). Averaging the velocities for sediment with (light grey) and without hydrate (dark grey) may provide a first good approximation for the overall velocity (c).

As water becomes the continuous phase, gas will occur in large bubbles (center column in Figure 6.1) further limiting the extent to which hydrate forms intergranular cement or even bridges sediment grains. Again, hydrate begins to form at gas water interface and forms a hydrate shell surrounding the gas bubble or patch. Unlike the low water-saturation cases, however, hydrate formation advances primarily into the gas phase rather than into the water phase. As gas is consumed, the pressure inside the bubble drops. If the pressure difference across the bubble interface becomes too large for the hydrate layer to withstand the shell ruptures and water leaks inside the gas-filled area. There it can be converted into more hydrate [Tohidi et al., 2001; Jung and Santamarina, 2010]. Images of CH_4 hydrate-bearing porous media published by Jin et al. [2006] and Tohidi et al. [2001] showed an accumulation of fragmented hydrate crystals inside the pore space, which resulted from collapsing hydrate crusts.

As opposed to hydrate formed in the presence of a continuous gas phase, hydrate formed from a continuous water phase grows away from the grain contacts and into the pore space. This behavior was also suggested by the comparison of measured velocities with velocities calculated with the Three-Phase Biot Theory [Lee and Waite, 2008] and Lee's Weighted Equation [Lee et al., 1996]. In both models, the behavior of the fitting parameters suggested the wave velocity contribution from cementation decreased relative to other factors during hydrate formation, which implies growth into the pore center and away from grain contacts. Rather than cementing grain contacts, the resulting hydrate bridges between grains across the pore space and acts as a load-bearing component of the sediment matrix that does not allow rotation or slip of grains (lower-center graph in Figure 6.1).

As the initial water saturation is increased further, bubbles shrink and eventually have no more contact with the grain surfaces (second column from the right in Figure 6.1). The gas is again evenly distributed throughout the sample and occurs in the form of smaller-than-pore-sized bubbles, which float freely in the pore water. As hydrate forms, the overall stiffness of the sediment remains largely unaffected until the hydrate saturation exceeds 30-40%. Below that critical value of hydrate formation, the hydrate particles are pore-filling and do not interact with the sediment. P-wave velocities increase only slightly as the hydrate causes a slight increase in the bulk modulus of pore fluids. S-wave velocities do not change at all [Priest et al. 2009]. The same is the case for hydrates formed out of solution (right column in Figure 6.1). Above the critical hydrate saturation of 30-40%, hydrate does interact with the sediment grains and an increase in P- and S-wave velocities can be observed as the hydrate transitions from being pore filling to becoming a load-bearing component of the sediment's unconsolidated mineral matrix (lower-right graph in Figure 6.1). Comparison of measured and modeled velocities indicated that, as opposed to the load-bearing hydrate formed from larger amounts of free gas, load-bearing gas hydrate formed out of solution allows slip and rotation of particles (lower-right graph of Figure 6.1) until the pore space is almost completely filled with hydrate (S_h>80%).

This new-found knowledge may help to better predict the elastic properties of gas hydrate-bearing sediments found in nature based on their formation history. For example, most marine gas hydrates formed through advecting gas bubbles or gas-saturated water in locations like the Nankai Trough, Shenhu Area or Alaminos Canyon in the Gulf of Mexico will be pore-filling or load-bearing, depending on the prevalent

hydrate content [Hutchinson et al., 2008; Collett et al., 2009; Fuji et al., 2009; Wang et al., 2011]. On the other hand, deposits developed in Arctic locations such as Prudhoe Bay will likely contain cementing hydrate as conventional gas reservoirs were converted into hydrate-bearing ones through changes in pressure and temperature [Collett et al., 2009; Dai et al., 2011]. The exact hydrate formation history of hydrate in a reservoir may not necessarily be of the utmost importance for exploration geophysicist intending to find highly-hydrate-saturated reservoirs suitable for gas extraction from hydrates. Exploration of gas hydrates for the purpose of production testing generally targets higher gas hydrate saturations. As we have seen above, velocity models converge at high saturations.

Nevertheless, the formation of hydrates as a function of initial water saturation should be of importance to researchers studying hydrate formation from free, recycled gas [Paull et al., 1994]. If a hydrate deposit is buried due to continued sedimentation, hydrates located at the base of the gas hydrate stability will dissociate and freed gas will move upward into the hydrate-bearing zone, where it is consumed by hydrate formation. As this process continues, more hydrate will decompose at every time step and more gas will be provided for hydrate formation. Consequently, the hydrate formation will transition from water-continuous mechanisms conceptualized on the far right side of Figure 6.1 to the mechanisms shown on the far-left. That means that hydrate at the base of stability zone is slowly transitioning from being pore-filling to becoming cementing. Our conceptual model of hydrate formation could thus help to model the elastic properties of the hydrate-bearing sediments as they change over time.

Furthermore, our conceptual model of hydrate formation in unconsolidated sediment will provide guidance those who studying the physical properties of laboratory-formed gas hydrates. Researchers are now able to predict what hydrate distribution to expect as a function of initial water saturation. This will allow researchers to interpret their laboratory-derived data set and relate measured parameters, for example electrical or flow properties, to the expected distribution of pore fluids and solids in the system.

CHAPTER 7

THE WAY FORWARD

The results presented in the previous chapters were obtained for hydrate-bearing systems that were idealized in many ways. P- and s-wave velocities were measured at ultrasonic frequencies in hydrate-bearing clean sand or glass beads without fine-grained or organic material. In addition, free-phase methane (CH_4) and "CH_4 substitutes", such as tetrahydrofuran (THF) or cyclopentane (CP), were used. Also, the pore fluid was either fresh water or contained large concentrations of barium chloride ($BaCl_2$). Even though we gained valuable insight into fundamental principles of hydrate formation in porous media and uncovered relationships between the hydrate formation method and elastic properties of hydrated sediment, additional research is required to translate these results to natural systems. Future studies should thus be focused on bringing the experimental systems and procedures closer to natural formations in terms of sample selection and measurement techniques. For example, velocity measurements could be extended to seismic and logging frequencies. Ultimately, the goal would be to move away from artificial hydrate-bearing sediments and investigate natural samples. As natural gas hydrate-cores are rare, costly, heterogeneous, and almost always show some degree of damage, sediments containing laboratory-formed gas hydrates will have to continue to be used as an alternative. Instead, the sample complexity could be increased by changing the pore fluid composition (e.g. salinity) or adding varying amounts of clay to the sandpack [Pohl et al., 2013]. The manner of hydrate formation

should also reflect CH_4 hydrate-formation processes in nature, which include not only hydrate formation from free CH_4 but also from dissolved CH_4. Investigation of more complex systems, however, may require modification of current experimental designs and could involve the inclusion of additional measurement techniques, e.g. spectral induced polarization (SIP) and nuclear magnetic resonance (NMR). Imaging techniques such as micro X-ray computed tomography (MXCT) or magnetic resonance imaging (MRI) remain indispensable and complementaryfor characterizing hydrate saturation and distribution In the following, an overview of some key recommendations that result from the outcome of this thesis is given.

- Low-frequency velocities and attenuation: Ultrasonic velocity measurements performed in the laboratory operate on frequencies (e.g. 500 kHz) that are different from field velocity measurements, such as seismic (about 10^0-10^2 Hz) and well-logging (about ~10^4 Hz) and it has been shown that elastic velocities can be frequency-dependent (i.e. dispersive) [Hornby et al., 1994; Hofmann, 2006]. Attenuation and dispersion are closely linked. It is thus vital to investigate dispersion in our hydrate-bearing sediment samples as a function of hydrate formation method before the velocity data obtained in the laboratory can be applied to calibrate field measurements. Colorado School of Mines has recently received a research grant from the Department of Energy (DOE) to study low-frequency velocities and attenuation in gas hydrate-bearing sediments [Batzle, 2012].
- MXCT with temperature-pressure control: The current sample holder only provides short-term cooling. Without pressure control or longer-term cooling,

the range of hydrate types that can be scanned is limited to those that remain stable for the duration of the scan, such as THF or CP hydrates. Installation of a temperature-controlled pressure vessel would enable acquisition of high-resolution images of hydrates of natural gases with which to observe hydrate formation and dissociation in a range of porous media. Effective temperature control may be achieved by bringing the pressure vessel in contact with Peltier elements [e.g. Takeya et al., 2007]. Setups used in previous imaging studies of hydrates circulated a cooled (confining) fluid [Kerkar et al., 2009; Ersland et al., 2010] or blew a cold stream of gaseous nitrogen through a nozzle directed at the center of the pressure vessel [Jin et al., 2004; 2006].

- Effect of grain size of THF hydrate formation: Gas hydrates preferentially form in very permeable deposits such as coarse grained or fractured sediments, where they can be disseminated in the pores or form as fracture fill. Most massive occurrences, on the other hand, are associated with fine-grained sediments and occur much more abundantly in nature. Work should be continued on MXCT scanning of THF hydrate-bearing porous media using the current experimental setup. Hydrate formation should be investigated in glass-beads samples with varying pore sizes and pore-size distributions. Grains sizes could range from 1-mm glass beads to silicate powders. The distributions could be layered, mixed, or uniform. In addition, host sediments with varying surface properties could be used. The results could help to improve our understanding of the preferential growth patterns of hydrates in sediment and may lead to the development of a methodology that allows the

synthesis of nodular, veined, or layered hydrate deposits. Note that the formation of grain-displacing hydrate will depend on the direction of the effective stress [Dai et al., 2010]. Consequently, the current hydrate formation apparatus should be modified to allow application of directional stress [Santamarina et al., 2012].

- Cyclopentane hydrate in porous media: When CP hydrate was formed from melting ice and CP, recorded velocities were higher compared than when they were formed from two liquid phases (Figure 7.1). Whether this was due to a higher water-to-hydrate conversion when using ice seeding or because of differences in the hydrate pore-scale distribution could not be resolved based the MCXT images acquired. CP hydrate-bearing specimens formed using ice-seeding should be imaged with MXCT and compared to the images obtained for CP hydrate-bearing samples formed from two liquid phases. As the density differences between CP hydrate (about 965 kg/m^3), liquid CP (751 kg/m3), water (1000 kg/m^3) and ice (920 kg/m^3) is relatively small, it may be advisable to add tracers to the liquid phases for an enhanced image contrast. Being able to distinguish between hydrate, hydrate former, and water or ice, will help to determine not only the distribution of each phase but also the amount of water converted into hydrate.

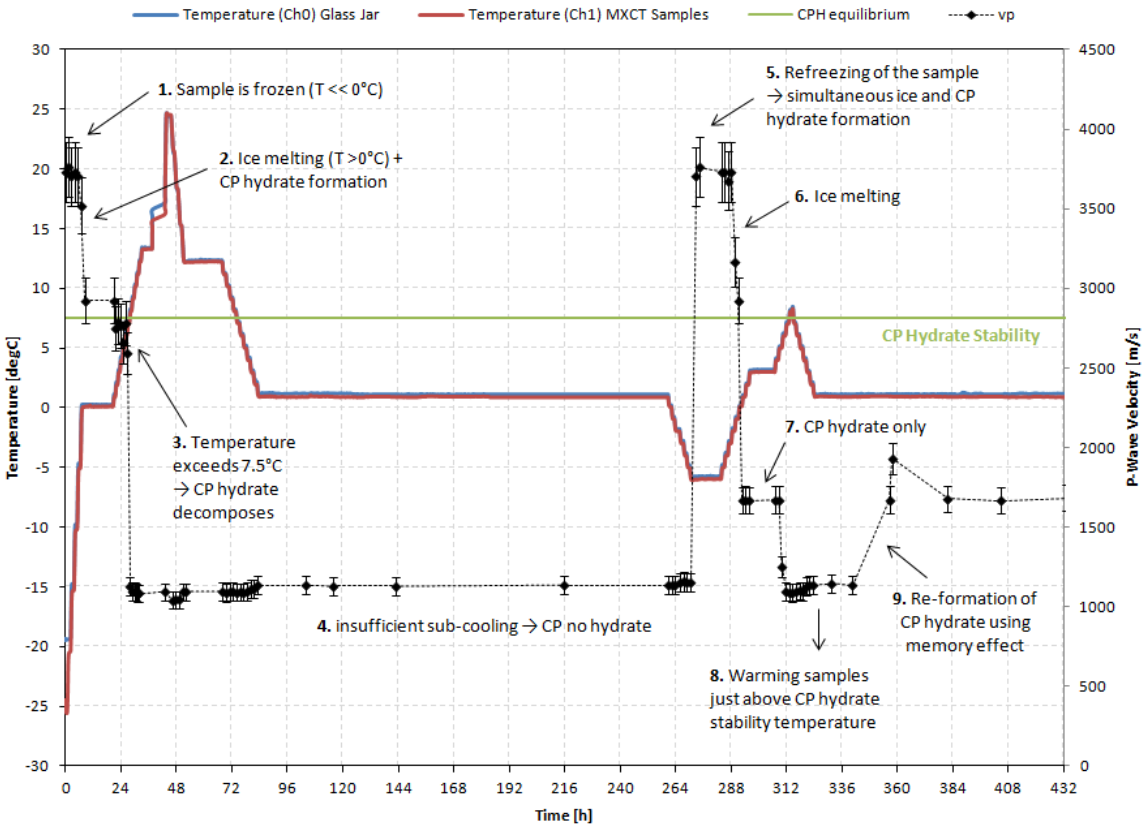

Figure 7.1: Temperature profile and ultrasonic velocities recorded during formation, dissociation, reformation of CP hydrate in glass beads. First hydrate is formed through ice seeding, then simultaneously with ice at sub-zero temperatures, and finally from two separate liquid phases utilizing the memory effect.

REFERENCES

Aman, Z., S. Joshi, E.D. Sloan, A.K. Sum, C.A. Koh, 2012, Micromechanical cohesion force measurements to determine cyclopentane hydrate interfacial properties, Journal of Colloid and Interface Science 376, 283-282

Aracne-Ruddle, C.M., B.P. Bonner, C.N. Trombino, E.D. Hardy, P.A. Berge,, C.O. Boro, D. Wildenschild, C.D. Rowe, and D.J. Hart, 1999, Ultrasonic Velocities in Unconsolidated Sand/Clay Mixtures at Low Pressures, Report, Laurence Livermore National Laboratory, Livermore, CA

Baldwin, B.A., A. Moradi-Araghi, J.C. Stevens, 2003, Monitoring hydrate formation and dissociation in sandstone and bulk with magnetic resonance imaging, Magnetic Resonance Imaging 21, 1061–1069

Baldwin B.A., J. Stevens, J.J. Howard, A. Graue, B. Kvamme, E. Aspenes, G. Ersland, J. Husebø, and D.R. Zornes, 2009, Using magnetic resonance imaging to monitor CH4 hydrate formation and spontaneous conversion of CH4 hydrate to CO2 hydrate in porous media, Magnetic Resonance Imaging 27, 720–726

Batzle, M., 2013, Measurements and Interpretation of Seismic Velocities and Attenuation in Hydrate-Bearing Sediment, a proposal submitted the U.S. Department of Energy under the solicitation DE-FOA-0000668, Colorado School of Mines, Golden, CO 80401

Berge, L.I., K.A. Jacobsen, and A. Solstad (1999), Measured acoustic wave velocities of Rll (CCI3F) hydrate samples with and without sand as a function of hydrate concentration, Journal of Geophysical Research 104 (B7), 15415-15424

Berndt, C., J. Mienert, M. Vanneste, and S. Bünz, 2005, Gas hydrate dissociation and sea floor collapsein the wake of the Storegga Slide, Norway, in Onshore-offshore relationships on the North Atlantic Margin, B.T.G. Wandås et al. (Eds.), Proceedings of a conference held in Trondheim in 2002, Norwegian Petroleum Society (NPF) Special Publication 12, Elsevier, 285-292

Bily, C., and J. W. L. Dick, 1974, Natural occurring gas hydrates in the Mackenzie delta, Northwest Territories: Bulletin of Canadian Petroleum Geology 22, 340–352.

Biot, M.A., 1941, General Theory of three-dimensional consolidation, Journal of Applied Physics, 12, 155-164

Bondarev, E.A., A.G. Groisman, and A.Z. Savvin, 1996, Porous medium effect on phase equilibrium of tetrahydrofuran hydrate, Proceedings of the 2nd International Conference on Natural Gas Hydrates, June2-6, Toulouse, France

Bowen, G.J., T.J. Bralower, G.R. Dickens, M. Delaney, D.C. Kelly, P.I. Koch, L. Kump, J. Meng, L.C. Sloan, E. Thomas, S.L. Wing, J.C. Zachos, 2006, Disciplinary and cross-disciplinary study of the Paleocene-Eocene Thermal Maximum gives new insight into greenhouse gas-induced environmental and biotic changes, EOS Transactions, American Geophysical Union 87(17), 165-169

Carcione J.M., and U. Tinivella, 2000, Bottom simulating reflectors: Seismic velocities and AVO effects, Geophysics, 65, no. 1, 54-67

Carcione, J.M., and D. Gei, 2004, Gas-hydrate concentration estimated from P- and S-wave velocities at the 2L-38 research well, Mackenzie Delta, Canada, Journal of Applied Geophysics 56, 73-78

Chand, S., T.A. Minshull, D. Gei, and J.M. Carcione, 2004, Elastic velocity models for gas hydrate-bearing sediments – a comparison, Geophysical Journal International 159, 573-590

Chaouch, A., and J.L. Briaud, 1997, Post-Melting Behavior of Gas Hydrates in Soft Ocean Sediments, Paper OTC 8298, Paper OTC 8297 presented at the 1997 Offshore Technology Conference, Houston, May 8-5

Christ, M., and J.B. Park, 2009, Ultrasonic technique as too for determining physical and mechanical properties of frozen soils, Cold Regions Science and Technology 58, 136-142

Collett, T. S., 2001, A Review of Well-Log Analysis Techniques Used to Assess Gas-Hydrate-Bearing Reservoirs, in Natural Gas Hydrates, C. K. Paull, and W. P. Dillon (Eds.), American Geophysical Union, Washington, D. C.

Collett, T. S., 2002, Energy resource potential of natural gas hydrates: AAPG Bulletin 86 (11), 1,971–1,992

Collett, T. S., A. H. Johnson, C. C. Knapp, and R. Boswell, 2009, Natural gas hydrates—Energy resource potential and associated geologic hazards, in Natural Gas Hydrates: A Review, , T. Collett, A. Johnson, C. Knapp, and R. Boswell (Eds.), AAPG Memoir 89, 146– 219

Collett, T. S., and S. R. Dallimore, 2002, Detailed analysis of gas hydrate induced drilling and production hazards, Proceedings of the 4th International Conference on Gas Hydrates, Yokohama, Japan, May 19-23

Collett, T.S., 2000, Quantitative well-log analysis of in situ gas hydrates, PhD Thesis, Colorado School of Mines, Golden, Colorado

Corak, D., T. Barth, T. Skodvin, R. Larsen, and T. Skjetne, 2011, Effect of subcooling and amount of hydrate former on formation of cyclopentane hydrate in brine, Desalination 278, 268-274

Dai, S., C. Lee, and J.C. Santamarina, 2011, Formation history and physical properties of sediments from the Mount Elbert Gas Hydrate Stratigraphic Test Well, Alaska North Slope, Marine and Petroleum Geology 28, 427-438

Dai, S., J. C. Santamarina, W. F. Waite, and T. J. Kneafsey, 2012, Hydrate morphology: Physical properties of sands with patchy hydrate saturation, J. Geophys. Res., 117, B11205, doi:10.1029/2012JB009667.

Diaconescou, C.C., R.M. Kieckhefer, and J.H. Knapp, 2001, Geophysical evidence for gas hydrates in deep water of the South Caspian Basin, Azerbaijan, Marine and Petroleum. Geology, 18, 209-221

Dickens, G.R., J.R. O'Neil, D.C. Rea, and R.M. Owen, 1995, Dissociation of oceanic methane hydrate as a cause of the carbon isotope excursion at the end of the Paleocene. Paleoceanography 10, 965–971

Domenico, S.N., 1976, Effect of Brine-Gas Mixture on Velocity in an Unconsolidated Sand Reservoir, Geophysics 41(5), 882-894

Domenico, S.N., 1977, Elastic Properties of Unconsolidated Porous Sand Reservoirs, Geophysics 42(7), 1,339-1,368

Dvorkin, J., and A. Nur, 1998, Acoustic signatures of patchy saturation, International Journal of Solids and Structures 35, 4803-4810

Dvorkin, J., and A. Nur, 1996, Elasticity of high-porosity sandstones: Theory for two North Sea data sets, Geophysics, 61, 1363-1370

Dyadin, Yu. A.; Kuznetsov, P. N.; Yakovlev, I. I.; Pyrinova, A. V., 1973, The system water-tetrahydrofuran in the crystallization region at pressures up to 9 kbar, Dokl. Chem. 208, 9-12

Ebinuma, T., K. Suzuki, H. Oyama, and H. Narita, 2008, Ultrasonic Wave Velocities Associated with Formation and Dissociation of Methane Hydrate in Artificial Sandy Sediment, presented at the 2008 Offshore Technology Conference, Paper OTC 19260, Houston, TX, May, 5-8

Ecker, C., J. Dvorkin, and A. Nur, 1998, Sediments with gas hydrates: internal structures from seismic AVO, Geophysics 63, 1659-1669

Ecker, C., J. Dvorkin, and A. Nur, 2000, Estimating the amount of gas hydrate and free gas marine seismic data, Geophysics 65 (2), 565-573

Elliot, S.E. and B.F. Wiley, 1975, Compressional Velocities of Partially Water Saturated Unconsolidated Sands, Geophysics 40 (6), 949-954

Ersland, G., J. Husebø, A. Graue, B.A. Baldwin, J. Howard, and J. Stevens, 2010, Measuring gas hydrate formation and exchange with CO2 in Bentheim sandstone using MRI tomography, Chemical Engineering Journal 158, 25–31

Espinoza, D.N. and J.C. Santamarina, 2011, P-wave monitoring of hydrate-bearing sand during CH4–CO2 replacement, Journal of Geophysical Research 115 (B10), 2156-2202

Franks, F., 1973, Water: A Comprehensive Treatise, Vol. 2, Plenum Press, New York

Fujii, T., T. Namikawa, T. Okui, M. Kawasaki, K. Ochiai, M. Nakamizu,M. Nishimura, O. Takano, andY. Tsuji, 2009, Methane hydrate occurrence and saturation confirmed from core samples, eastern Nankai Trough, Japan, in Natural Gas Hydrates: A Review, T. Collett, A. Johnson, C. Knapp, and R. Boswell (Eds.), AAPG Memoir 89, 385–400

Gao, S., W. House, and W.G. Chapman, 2005, NMR/MRI study of Clathrate Hydrate Mechanisms, Journal of Physical Chemistry B, 109, 19090-19093

Gassmann, F., 1951, Über die Elastizität poroser Medium, Vierteljarhschrift der Naturforschenden Gesellschaft in Zürich, 96, 1-23

Gei, D., and J.M. Carcione, 2003, Acoustic properties of sediments saturated with gas hydrate, free gas, and water, Geophysical Prospecting, 51, 141-157

Gough, S.R., and D.W. Davidson, 1971, Composition of tetrahydrofuran hydrate and the effect of pressure on the decomposition, Canadian Journal of Chemistry 49 (16), 2691-2699

Graue, A., B. Kvamme, B. A. Baldwin, J. Stevens, J. Howard, G. Ersland, J. Husebø, and D. R. Zornes, 2006, Magnetic resonance imaging of methane-carbon dioxide hydrate reactions in sandstone pores, Proceedings of the Society of Petroleum Engineers Annual Technical Conference and Exhibition, SPE Paper 102915

Hadley, C., D. Peters, A. Vaughan, and D. Bean, 2008, Gumusut-Kapak Project: Geohazard Characterization and Impact on Field Development Plans, International Petroleum Technology Petroleum Conference, IPTC 12554, Kuala Lumpur, Malaysia, December 3-5

Handa, Y. P., 1990, Effect of hydrostatic-pressure and salinity on the stability of gas hydrates, Journal of Physical Chemistry 94, 2652–2657

Hardage, B.A., P. Murray, D. Sava, M. Backus, R. Remington, and R. Graebner, 2006, Evaluation of deepwater gas-hydrate systems, The Leading Edge, 25, no. 5, 572-577

Hashin, Z., and S. Shtrikman, 1963, A variational approach to the elastic behavior of multiphase materials, Journal of Mechanics and Physics of Solids 11, 127-140

Helgerud, M., 2001, Wave speeds in gas hydrates and sediments containing gas hydrate: A laboratory and modeling study, PhD thesis, Stanford University

Helgerud, M.B. J. Dvorkin, A. Nur, A. Sakai, and T. Collett, 1999, Elastic wave-velocity in marine sediments with gas hydrates: Effective medium modeling, Geophysical Research Letters 26(13), 2,021-2,024

Helgerud, M.B., J. Dvorkin, and A. Nur, 2000, Rock physics characterization for gas hydrate reservoirs, elastic properties, in Gas Hydrates, Challenges for the Future, G.D. Holder, and P.R. Bishnoi, (Eds.), Annals of the New York Academy of Sciences 912, 116-125

Helgerud, M.B., W.F. Waite, S.H. Kirby, and A. Nur, 2003, Measured temperature and pressure dependence of compressional (V_p) and shear (V_s) wave speeds in compacted, polycrystalline ice Ih, Canadian. Journal of Physics 81, 81 – 87

Helgerud, M.B., W.F. Waite, S.H. Kirby, and A. Nur, 2009, Elastic wave speeds and moduli in polycrystalline ice Ih, sI methane hydrate and sII methane-ethane hydrate, Journal of Geophysical Research 114, B02212

Hesslebo, S.P., D.R. Grocke, H.C. Jenkyns, C.J. Bjerrum, P. Farrimond, H.S.M. Bell, and O.R. Green, 2000, Massive dissociation of gas hydrate during a Jurassic oceanic anoxic event, Nature 406, 392–395

Hill, R., 1952, The elastic behavior of a crystalline aggregate, Proceeding of the Physical Society, A65, 349-354

Hofmann, R., 2006, Frequency dependent elastic and anelastic properties of clastic rocks, PhD Thesis, Colorado School of Mines, Golden, CO

Holder, G.D., V.A. Kamath, and S.P. Godbole, 1984, The Potential of National Gas Hydrates as an Energy Resource, Annual Review of Energy 9, 427-445

Hornbach, M., Lavier, L., and Ruppel, C., 2007, Triggering mechanism and tsunamogenic potential of the Cape Fear Slide complex, U.S. Atlantic margin, Geochemistry Geophysics Geosystems (G3) 8, 12008, doi: 10.1029/2007GC001722.

Hornby, B. E., Schwartz, L. M., & Hudson, J. A., 1994, Anisotropic effective-medium modeling of the elastic properties of shales, Geophysics 59 (10), 1570–1583

Hu, G.W., Y.G. Ye, J. Zhang, C.L. Liu, S.B. Diao, and J.S. Wang, 2010, Acoustic properties of gas hydrate-bearing consolidated sediments and experimental testing of elastic velocity models, Journal of Geophysical Research 115, B02102

Hutchinson et al., 2008, Site selection for DOE/JIP gas hydrate drilling in the Northern Gulf of Mexico, 6th International Conference on Gas Hydrates, , Vancouver, British Columbia, Canada, July 6-10, 2008

Hyndman, R.D. and E.E. Davis, 1992, A Mechanism for the Formation of Methane Hydrate and Seafloor Bottom Simulating Reflectors by Vertical Fluid Expulsion, Journal of Geophysical Research 95 (B5), 7025-7041

Jacoby, M., J. Dvorkin, and X. Liu, 1996, Elasticity of partially saturated, frozen sand, Geophysics 61(1), 288-293

Jin, S., J. Nagao, S. Takeya, Y. Jin, J. Hayashi, Y. Kamata, T. Ebinuma, and H. Narita, 2006, Structural investigation of Methane Hydrate Sediments by Microfocus X-ray Computed Tomography, Japanese Journal of Applied Physics 54 (23), 714

Jin, S., S. Takeya, J. Hayashi, J. Nagao, Y. Kamata, T. Ebinuma, and H. Narita, 2004, Structural Analysis of Artificial Methane Hydrate Sediments by Microfocus X-ray Computed Tomography, Japanese Journal of Applied Physics 43 (8A), 5673

Jung, J.W., and J.C. Santamarina, 2012, Hydrate formation and growth in pores, Journal of Crystal Growth 245, 61-68

Kerkar, P., K.W. Jones, R. Kleinberg, W.B. Lindquist, S. Tomov, H. Feng, and D. Mahajan, 2009, Direct observations of three dimensional growth of hydrates hosted in porous media, Applied Physics Letters 95, 024102

Kiefte, H., M.J. Clouter, and R.E. Gagnon, 1985, Determination of Acoustic Velocities of Clathrate Hydrates by Brillouin Spectroscopy, Journal of Physical Chemistry 89, 3103-3108

Kingston, E., C. Clayton, and J. Priest, 2008, Gas hydrate growth morphologies and their effect of stiffness and damping of hydrate-bearing sand, Proceeding of the 6th International Conference on Gas Hydrates, Vancouver, British Columbia, Canada, July 6-10, 2008

Kneafsey, T. J., L. Tomutsa, G. J. Moridis, Y. Seol, B. M. Freifeld, C. E. Taylor, and A. Gupta, 2007, Methane hydrate formation and dissociation in a partially saturated core-scale sand sample, Journal of Petroleum Science & Engineering 56, 108-126

Krief, M., J. Garat, J. Stellingwerff, and J. Ventre, 1990, A petrophysical interpretation using the velocities of P- and S-waves, Log Analyst, 31, 355-369

Kuhs, W.F., G. Genov, D.K. Staykova, and T. Hansen, 2004, Ice perfection and onset of anomalous preservation of gas hydrates, Physical Chemistry Chemical Physics 6, 4917-4920

Kunerth, D.C., D.M. Weinberg, J.W. Rector III, C.L. Scott, and J.T. Johnson, 2001, Journal of Seismic Exploration 9, 337

Kurfürst, P.J., 1976, Ultrasonic wave measurements on frozen soils at permafrost temperatures, Canadian Journal of Earth Science 13, 1,571-1,576

Kuster, G.T., and M.N. Toksöz, 1974, Velocity and attenuation of seismic waves in two-phase media: Part 1, Theoretical formulations, Geophysics, 39, 587-606

Kvenvolden, K.A., 1993, Gas Hydrates – geological perspective and global change, Review of Geophysics 31 (2), 173-187

Kvenvolden, K.A., and M.A. McMenamin, 1980, Hydrates of natural gas: A review of their geologic occurrences, US Geological Survey Circulation 825

Kvenvolden, K.A., and T.D. Lorenson, 2001, The Global Occurrence of Natural Gas Hydrate, in Natural Gas Hydrates: Occurrence, Distribution, and Detection, Geophysical Monograph 124, edited by C.K. Paull and W.P. Dillon, pp. 3-18, AGU, Washington, D.C.

Kwon, T.H. and G.C. Cho, 2009, Evolution of Compressional Wave Velocity during CO2 Hydrate Formation in Sediments, Energy and Fuels 23, 5,731-5,736

Lapham, L. L., J. P. Chanton, R. Chapman, and C. S. Martens, 2010, Methane under-saturated fluids in deep-sea sediments, Implications for gas hydrate stability and rates of dissolution, Earth and Planetary Science Letters 298 (3-4), 275-285

Larsen, R., C. Knight, and E.D. Sloan, 1996, Clathrate hydrate growth and inhibition, Fluid Phase Equilibria 150-151. 353-360

Leclaire P., F. Cohen-Tenoudji, and Aguirre-Puente (1994), Observation of two longitudinal and two transverse waves in a frozen porous medium, Journal of the Acoustic Society of America, 97, 2052-2055

Lee, J.Y., F.M. Francisca, J.C. Santamarina, and C. Ruppel, 2010, Parametric study of the physical properties of hydrate-bearing sand, silt, and clay sediments: 2. Small-strain mechanical properties, Journal of Geophysical Research 115, B11105

Lee, J.Y., J.C. Santamarina, and C. Ruppel, 2010, Volume change associated with the formation and dissociation of hydrate in sediment, Geochemistry Geophysics Geosystems (G3) 11 (3), 13

Lee, J.Y., J.C. Santamarina, C. Ruppel, 2008, Mechanical and electromagnetic properties of northern Gulf of Mexico sediments with and without THF hydrates, Marine and Petroleum Geology 25, 884–895

Lee, J.Y., T.S. Yun, and J.C. Santamarina, 2007, Observations related to tetrahydrofuran and methane hydrates for laboratory studies of hydrate-bearing sediments, Geochemistry Geophysics Geosystems (G3) 8 (6)

Lee, M.W., 2004, Elastic velocities of partially gas-saturated unconsolidated sediments, Marine and Petroleum Geology 2, 641–650

Lee, M.W., 2005, Proposed moduli of dry rock and their application to predicting elastic velocities of sandstones, Scientific Investigation Report, 2005-5119, United States Geological Survey

Lee, M.W., and W.F. Waite, 2008, Estimating pore-space gas hydrate saturations from well-log acoustic data, Geochemistry Geophysics Geosystems 9 (7), Q07008

Lee, M.W., D.R. Hutchinson, T.S. Collett, and W.P. Dillon, 1996, Seismic Velocities for hydrate-bearing sediments using weighted equation, Journal of Geophysical Research 101(B9), 20,347-20,358

López, C., G. Spence, R. Hyndman, and D. Kelley, 2010, Frontal ridge slope failure at the northern Cascadia margin: Margin-normal fault and gas hydrate control, Geology 38 (11), 967-970

Lu, N., and W.J. Likos, 2004, Unsaturated Soil Mechanics, John Wiley and Sons, Inc., Hoboken, New Jersey

Makogon, Y. F., F. A. Trebin, A. A. Trofimuk, V. P. Tsarev, and N. V. Cherskiy, 1972, Detection of a pool of natural gas in a solid (hydrate gas) state: Doklady Academy of Sciences U.S.S.R., Earth Science Section 196, 197–200

Mavko, G., T. Mukerji, and J. Dvorkin, 1998, The Rock Physics Handbook: Tools for Seismic Analysis in Porous Media, Cambridge University Press, Cambridge

McConnell, D.R., Z. Zhang, and R. Boswell, 2012, Review of progress in evaluating gas hydrate drilling hazards, Marine and Petroleum Geology 34, 209-223

Mindlin, R.D., 1949, Compliance of elastic bodies in contact, Journal of Applied Mechanics, 16, 259-268

Moon, C., P.C. Taylor, and, P.M. Rodger, 2003, Molecular Dynamics Study of Gas Hydrate Formation, Journal of the American Chemical Society 125 (16), 4706-4707

Mosher, D., 2009, International year of planet Earth 7, Oceans, Submarine landslides and consequent tsunamis in Canada, Geoscience Canada 36, 179–190

Moudrakovski, I.L., C.I. Radcliff, and J.A. Ripmeester, 2002, Application of magnetic resonance microimaging (MRM) to monitor the formation of gas hydrate, Proceedings of the 4th International Conference on Gas Hydrates, Yokohama, Japan, May 19-23

Nakano, Y., and R. Arnold, 1973, Acoustic Properties of Frozen Sand, Water Resources Research 9(1), 178-184

Nakano, Y., R.J. Martin III, and M. Smith, 1972, Ultrasonic velocities of the Dilatational and Shear Waves in Frozen Soils, Water Resources Research 8(4), 1,024-1,030

Nimblett, J.N., R.C. Shipp, and F. Strijbos, 2005, Gas Hydrate as a Drilling Hazard: Examples from Global Deepwater Settings, OTC 17476, Proceedings of the Offshore Technology Conference, Houston, TX, May 2-5

Ohmura, R., M. Ogawa, K. Yasuoka, and Y. H. Mori, 2003, Statistical Study of Clathrate-Hydrate Nucleation in a Water/Hydrochlorofluorocarbon System: Search for the Nature of the "Memory Effect", The Journal of Physical Chemistry B 107 (22), 5289-5293

Paull, C. K., Ussler, W., III, and Borowski, W., 1994, Sources of biogenic methane to form marine gas-hydrates: In situ production or upward migration?, New York Academy of Science Annals 715, 392–409

Paull, C.K., Matsumoto, R., Wallace, P.J., et al., 1996, Proc. ODP, Initial Report 164, College Station, TX (Ocean Drilling Program)

Paull, C.K., W. Ussler III, T. Lorenson, W. Winters, and J. Dougherty, 2005, Geochemical constraints on the distribution of gas hydrates in the Gulf of Mexico, Geo-Marine Letters 25 (5), 273-280

Pearson, C.F., P.M. Halleck, P.L. McGuire, R. Hermes, and M. Matthews, 1983, Natural Gas Hydrates: A Review of In Situ Properties, Journal of Physical Chemistry 87, 4180

Pecher, I., S. Henrys, S. Ellis, S. Chiswell, and N. Kukowski, 2005, Erosion of the seafloor at the top of the gas hydrate stability zone on the Hikurangi Margin, New Zealand, Geophysical Research Letters 32, L24603, doi:10.1029/2005GL024687

Pohl, M., 2012, Ultrasonic and Low-Frequency Velocity Measurements of THF Hydrate-Bearing Sediments: M.S. Thesis, Bergakademie Freiberg

Pohl, M., M.B. Rydzy, and M.L. Batzle, 2013, Investigating the influence of clay content on ultrasonic velocities of THF hydrate-bearing sediment, presented at the 2nd International Workshop on Rock Physics, Southampton, UK, August 4-9

Posewang, J., and J. Mienert, 1999, High-resolution seismic studies of gas hydrates west of Svalbard, Geo-Marine Letters, 19, 150-156

Prasad, M., and J.Dvorkin, 2004, Velocity and Attenuation of Compressional Waves in Brines, SEG International Exposition and 74th Annual Meeting, Denver, Colorado, October 10-15

Prasad, M., and R. Meissner, 1992, Attenuation mechanisms in sands: Laboratory versus theoretical Biot-data, Geophysics 57, 710–719

Pride, S.R., J.G. Berryman, and J.M. Harris, 2004, Seismic attenuation due to wave-induced flow, Journal of Geophysical Research, 109, B01201

Priest, J. A., A.I. Best, and C.R.I. Clayton, 2005, A laboratory investigation into seismic velocities of methane gas hydrate-bearing sand, Journal of Geophysical Research 110, B04102

Priest, J., A.I. Best, and C.R.I. Clayton, 2006, Attenuation of seismic waves in methane gas hydrate-bearing sand, Geophysical Journal International 164, 149-159

Priest, J.A., E.V.L. Rees, and C.R.I. Clayton, 2009, Influence of gas hydrate morphology on the seismic velocities of sands, Journal of Geophysical Research, 114, B11205

Ren, S.R., Yo. Liu, Yi. Liu, W. Zhang, 2010, Acoustic velocity and electrical resistance of hydrate-bearing sediments, Journal of Petroleum Science and Engineering 70, 52-56

Robertson, P. K., S. Sasitharan, J. C. Cunning, and D. C. Sego, 1995, Shear wave velocity to evaluate in-situ state of Ottawa sand: Journal of Geotechnical Engineering, 121, 262–273

Ruppel, C., R. Boswell, and E. Jones, 2008, Scientific results from Gulf of Mexico Gas Hydrates Joint Industry Project Leg 1 drilling: Introduction and overview, Marine and Petroleum Geology, 25(9), 819-829.

Saito, H., E. Nakayama, and T. Yokoyama, 2010, Seismic Wave Velocities & Electrical Resistivity of Core Samples containing Methane Hydrate, OTC Paper 20707, Offshore Technology Conference, Houston, Texas., May 5-8

Santamarina, J. C., S. Dai, J. Jang, and M. Terzariol, 2012, Pressure core characterization tools for hydrate-bearing sediments, Scientific Drilling, 14, 44-48

Santamarina, J.C. and C. Ruppel, 2010, The impact of hydrate saturation on the mechanical, electrical, and thermal properties of hydrate-bearing sand, silts, and clay (Chapter 26), In: Riedel, Willoughby, Chopra (eds), Geophysical Characterization of Gas Hydrates, Society of Exploration Geophysicists Geophysical Developments, vol. 14, 373-384

Santamarina, J.C., and C. Ruppel, 2008, The impact of hydrate saturation on the mechanical, electrical, and thermal properties of hydrate-bearing sand, silts, and clay, Proceedings of the 6th International Conference on Gas Hydrates, Vancouver, British Columbia, Canada, July 6-1

Santamarina, J.C., K.A. Klein, and M.A. Fam, 2001, Soils and Waves: Particulate materials behavior, characterization and process monitoring. John Wiley & Sons, Ltd. 488, New York

Satoh T., S.R. Dallimore, T.S. Collett, T. Inoue, S.H. Hancock, and G.J. Moridis, 2005, Production test planning for the JAPEX/JNOC/GSC et al. Mallik 5L-38 gas hydrate production research well, in Scientific Results from the Mallik 2002 Gas Hydrate Program, Mackenzie Delta, Northwest Territories, Canada, S.R. Dallimore & T.S. Collett (Eds.), Bulletin 585, Geological Survey of Canada, Ottawa

Sava, D. and B. Hardage, 2006, Rock physics characterization of hydrate-bearing deepwater sediments, The Leading Edge, 25 (5), 616–619

Sava, D., and B. Hardage, 2009, Rock-physics models for gas-hydrate systems associated with unconsolidated marine sediments, in T. Collett, A. Johnson, C. Knapp, and R. Boswell, eds., Natural gas hydrates - Energy resource potential and associated geologic hazards: AAPG Memoir 89, 505– 524.

Schön, J.H., 1996, Physical Properties of Rocks, Handbook of Geophysical Exploration, Section I Seismic Exploration 18, Pergamon, Oxford, U.K.

Sefidroodi, H., E. Abrahamsen, and M.A. Kelland, 2013, Investigation into the strength and source of the memory effect for cyclopentane hydrate, Chemical Engineering Science 87, 133-140

Seol, Y., and T. J. Kneafsey, 2011, Methane hydrate induced permeability modification for multiphase flow in unsaturated porous media, Journal of Geophysical Research, 116, B08102

Shelander, A., J. Dai, G. Bunge, S. Singh, M. Eissa, and Kevin Fisher, 2012, Estimating saturation of gas hydrates using conventional 3D seismic data, Gulf of Mexico Joint Industry Project Leg II, Marine and Petroleum Geology 34, 96-110

Sloan, E.D., and C.A. Koh, 2008, Clathrate Hydrates of Natural Gases, 3rd Edition, CRC Press, Boca Raton

Spangenberg E., and J. Kulenkampff, 2005, Physical properties of gas hydrate-bearing sediments, Proceedings of the 5th International of Conference on Gas Hydrates, Trondheim, Norway, 12-16 June

Spangenberg, E., B. Beeskow-Strauch, M. Luzi, R. Naumann, J.M. Schicks, and M. Rydzy, 2008, The process of hydrate formation in clastic sediments and its impact on their physical properties, 6th International Conference on Gas Hydrates, Vancouver, British Columbia, Canada, July 6-10, 2008

Spangenberg, E., J. Kuhlenkampff, R. Naumann, and J. Erzinger, 2005, Pore space hydrate formation in a glass bead sample from methane dissolved in water, Journal of Geophysical Research 32, L24301

Stevens, J.C., J.J. Howard, and B.A. Baldwin, 2008, Experimental Hydrate Formation & Gas Production Scenarios Based on CO_2 Sequestration, Proceeding of the 6th International Conference on Gas Hydrates, Vancouver, British Columbia, Canada, July 6-10, 2008

Stoll, R. D., J. I. Ewing, and G. M. Bryan, 1971, Anomalous wave velocities in sediments containing gas hydrates, Journal Geophysical Research 76 (8), 2090–2094

Stoll, R., and G.M. Bryan, 1979, Physical Properties of Sediments Containing Gas Hydrates, Journal of Geophysical Research 84 (B4), 1629-1634

Takeya, S., A. Hori, T. Hondoh, and T. Uchida, 2000, Freezing-Memory Effect of Water on Nucleation of CO_2 Hydrate Crystals, The Journal of Physical Chemistry B 104 (17), 4164-4168

Takeya, S., K. Honda, Y. Yamamato, A. Yoneyama, Y. Hirai, K. Hyodo, and T. Takeda, 2007, Imaging and density mapping of tetrahydrofuran clathrate hydrates by phase-contrast x-ray computed tomography, Applied Physics Letters 90, 081920, 1-3

Tan, C.P., M.B. Clennell, R. Freij-Ayoub, B. Tohidi, and J. Yang, 2005, Mechanical and Petrophysical Characterisation and Wellbore Stability Management in Gas Hydrate-Bearing Sediments, presented at the Alaska Rocks 2005, The 40th U.S. Symposium on Rock Mechanics (USRMS): Rock Mechanics for Energy, Mineral and Infrastructure Development in the Northern Regions, Anchorage, Alaska, June 25-29

Taylor, C.J., K.T. Miller, C.A. Koh, and E.D. Sloan, 2007, Macroscopic investigation of hydrate film growth at the hydrocarbon/water interface, Chemical Engineering Science 62, 6524-6533

Timur, A., 1968, Velocity of compressional waves in porous media at permafrost temperatures, Geophysics 33 (4), 854-595

Tohidi, B., R. Anderson, M.B. Clennell, R.W. Burgass, A.B. Bidercap, 2001, Visual observations of gas hydrate formation and dissociation in synthetic porous media by means of glass micromodels, Geology 29 (9), 867-870

Tréhu, A.M., Bohrmann, G., Torres, M.E., and Colwell, F.S., 2006a, Proc. ODP, Sci. Results, 204, College Station, TX (Ocean Drilling Program)

Tréhu, A. M., C. Ruppel, M. Holland, D. R. Dickens, M. E. Torres, T. S. Collett, D. Goldberg, M. Riedel, and P. Schultheiss, 2006b, Gas hydrates in marine sediments, lessons from scientific ocean drilling: Oceanography 19 (4), 124–142

Trofimuk, A. A., N. V. Cherskiy, and V. P. Tsarev, 1977, The role of continental glaciation and hydrate formation on petroleum occurrences, in R. F. Meyer, ed., Future supply of nature-made petroleum and gas: New York, Pergamon Press, 919–926

Uchida, T., S. Dallimore, and J. Mikami, 2000, Occurrences of Natural Gas Hydrates beneath the Permafrost Zone in Mackenzie Delta: Visual and X-ray CT Imagery, Annals of the New York Academy of Sciences 912, 1749-6632

Uchida, T., S.R. Dallimore, J. Mikami, and F.M. Nixon, 1999, Occurrences and X-Ray computerized tomography (CT) observations of natural gas hydrate, in Scientific Results from JAPEX/JNOC/GSC Mallik 2L-38 Gas Hydrate Research Well, Mackenzie Delta, Northwest Territories, S.R. Dallimore, T. Uchida, and T.S. Collett (Eds.), Canada. Bull. Geol. Surv. Can., 544, 197-204

Waite, W., M. Helgerud, A. Nur, J. Pinkston, L. Stern, and S. Kirby, 2000, Laboratory measurements of compressional and shear wave speeds through methane hydrate, in Gas Hydrates: Challenges for the Future, edited by G. D. Holder and P. R. Bishnoi, Annals of the New York Academy of Sciences 912, 1003 – 1010

Waite, W.F., J.C. Santamarina, M. Rydzy, S.H. Chong, J.L.H. Grozic, K. Hester, J. Howard, T.J. Kneafsey, J.Y. Lee, S. Nakagawa, J. Priest, E. Rees, E.D. Sloan, 2011, Inter-Laboratory Comparison of wave velocity measurements in a sand under hydrate-bearing and other set conditions, 7th International Conference on Gas Hydrates, Ediburgh, Scotland, United Kingdom, July 17-21, 2011

Waite, W.F., J.C. Santamarina, M. Rydzy, S.H. Chong, J.L.H. Grozic, K. Hester, J. Howard, T.J. Kneafsey, J.Y. Lee, S. Nakagawa, J. Priest, E. Rees, E.D. Sloan, 2012, Overview of the Inter-Laboratory Comparison of Wave Velocity measurements in Sand with Gas Hydrates and other Pore-Filling Materials, Fire in the Ice 12 (1), 16-21

Waite, W.F., L.Y. Gilbert, W.J. Winters, D.H. Mason, 2005, Thermal property measurements in tetrahydrofuran (THF) hydrate and hydrate-bearings sediment between -25 and +4°C, and their application to methane hydrate, 5th International Conference on Gas Hydrates, Trondheim, Norway, June 12-16, 2005

Waite, W.F., W.J. Winters, and D.H. Mason, 2004, Methane hydrate in partially water-saturated sand, American Mineralogist 89, 1202-1207

Walsh, M.R., S.H. Hacock, S.J. Wilson, S.L. Patil, G. Moridis, R. Boswell, T.S. Collett, C.A. Koh, and E.D. Sloan, 2009, Prelimenary report on the commercial viability of gas production from natural gas hydrates, Energy Economics 31 (5), 815-823

Walton, K., 1987, The effective elastic moduli of a random packing of spheres, Journal of the Mechanics and Physics of Solids 35, 213–226

Wang, D., L.D. Li, H.L. Zhang, S.S. Fan, and H.B. Zhao, 2008, Laboratory measurement of longitudinal wave velocity of artificial gas hydrate under different temperatures and pressures, Science in China Series G: Physics, Mechanics, and Astronomy 51(12), 1,905-1,913

Wang, D.Y., Y.L. Zhu, W. Ma, and Y.H. Niu, 2006, Application of ultrasonic technology for physical-mechanical properties of frozen soils, Cold Regions Science and Technology 44, 12-19

Wang, X., D.R. Hutchinson, S. Wu, S. Yang, and Y. Guo, 2011, Elevated gas hydrate saturation within silty and silty clay sediments in the Shenhu area, South China Sea, Journal of Geophysical Research 116, B05102

Whitman, C.A., R. Mysyk, and M.A. White, 2008, Investigation of factors affecting crystallization of cyclopentane clathrate hydrate, The Journal of Chemical Physics 129, 174502

Wildenschild, D., J.W. Hopmans, C.M.P. Vaz, M.L. Rivers, D. Rikard, and B.S.B. Christensen, 2002, Using X-ray computed tomography in hydrology: systems, resolutions, and limitations, Journal of Hydrology 267, 285-297

Wood, A.B., 1941, A Textbook of Sound, Macmillan, New York

Wood, W.T., P.I Stoffa, and T.H. Shipley, 1994, Quantitative detection of methane hydrate through high-resolution seismic velocity analysis, Journal of Geophysical Research, 99, 9681-9695

Wu, S., G. Zhang, Y. Huang, J. Liang, and H.K. Wong, 2005, Gas hydrate occurrence on the continental slope of the northern South China Sea, Marine and Petroleum Geology, 22, 403-412

Xu, W., and C. Ruppel, 1999, Predicting the occurrence, distribution, and evolution of methane gas hydrate in porous marine sediments, Journal of Geophysical Research 104, 5,081–5,095

Xue, K., J. Zhao, Y. Song, W. Liu, W. Lam, Y. Zhu, Y. Liu, C. Cheng, and D. Liu, 2012, Direct Observations of THF Hydrate Formation in Porous Microstructure Using Magnetic Resonance Imaging, Energies 5, 898-910

Yakushev, V., and T.S. Collett, 1992, Gas Hydrates in Arctic Regions – risks to drilling & production, International Offshore and Polar Engineering Conference, Volume 1, ISOPE, Golden, CO, 669-673

Yin, H., 1992, Acoustic Velocity and Attenuation of Rocks, Isotropy, Intrinsic Isotropy, and Stress Induced Anisotropy, PhD Thesis, Stanford University

Yuan, T., R.D. Hyndman, and G.D. Spence, 1996, Seismic velocity increase and deep-sea gas hydrate concentration above a bottom-simulating reflector on the northern Cascadia continental slope, Journal of Geophysical Research 101 (B6), 13,655-13,671

Yun, T.S., F.M. Francisca, J.C. Santamarina, and C. Ruppel, 2005, Compressional and shear wave velocity in uncemented sediment containing gas hydrate, Geophysical Research Letters 32, L10609

Zhang, Y., P.G. Debenedetti, R.K. Prud'homme, and B.A. Pethica, 2004, Differential Scanning Calorimetry Study of Clathrate Hydrate Formation, Journal of Physical Chemistry B 108, 16717-16722

Zhao, J., L. Yao, Y. Song, K. Xue, C. Cheng, Y. Liu, and Y. Zhang, 2011, In situ observations by magnetic resonance imaging for formation and dissociation of tetrahydrofuran hydrate in porous media, Magnetic Resonance Imaging 29, 281-288

Zimmer, M.A., M. Prasad, G. Mavko, and A. Nur, 2007a, Seismic velocities of unconsolidated sands: Part 1 – Pressure trends from 0.1 to 20 MPa, Geophysics 72 (1), E1-E13

Zimmer, M.A., M. Prasad, G. Mavko, and A. Nur, 2007b, Seismic velocities of unconsolidated sands: Part 2 – Influence of sorting- and compaction-induced porosity variation, Geophysics 72 (1), E15-E25

Zimmermann, R.W. and M.S. King, 1986, The effect of the extend of freezing on seismic velocities in unconsolidated permafrost, Geophysics 51 (6), 1,285-1,290